

University of Nevada, Reno

**Investigating Snowfall Enhancement through Cloud Seeding: A  
Microphysical Modeling and Remote Sensing Approach**

A dissertation submitted in partial fulfillment of the requirements for  
the degree of Doctor of Philosophy in Atmospheric Science

by

Ghazal Mehdizadeh

Dr. Farnaz Hosseinpour /Dissertation Advisor

August, 2025

© by Ghazal Mehdizadeh 2025  
All Rights Reserved



THE GRADUATE SCHOOL

We recommend that the dissertation  
prepared under our supervision by

**Ghazal Mehdizadeh**

entitled

**Investigating Snowfall Enhancement through Cloud Seeding: A  
Microphysical Modeling and Remote Sensing Approach**

be accepted in partial fulfillment of the  
requirements for the degree of

**Doctor of Philosophy**

Farnaz Hosseinpour, Ph.D.  
*Advisor*

Frank McDonough, M.Sc.  
*Co-advisor*

Ehsan Erfani, Ph.D.  
*Committee Member*

Stanislav Jabuka, Ph.D.  
*Committee Member*

Anna Panorska, Ph.D.  
*Graduate School Representative*

Markus Kemmelmeier, Ph.D., Dean  
*Graduate School*

August, 2025

## **Abstract**

Cloud seeding has been employed as a weather modification strategy to enhance precipitation, particularly in arid and semi-arid regions where water scarcity is a constant concern. Despite its widespread use, the scientific understanding of its effectiveness remains incomplete. Many operational programs rely on limited observational data or simplified assumptions, which can obscure the physical mechanisms behind seeding outcomes. This dissertation aims to bridge that gap by combining high-resolution microphysical modeling with satellite-based remote sensing to evaluate the effects of glaciogenic cloud seeding in the western United States. Through a series of case studies and broader regional analyses, this research significantly deepens our understanding of cloud seeding mechanisms and provides insights for future cloud seeding studies.

A central tool in this dissertation is the Snow Growth Model for Rimed Snowfall (SGMR), a model developed to simulate key processes involved in ice crystal development, such as nucleation by silver iodide, vapor deposition, aggregation, and riming. The model was first applied to five cloud seeding events in the Lake Tahoe area. For each event, inputs such as cloud top and base heights, temperatures, liquid water content, and ice water content from MERRA-2 and CERES datasets were used to drive the model. The SGMR provided detailed estimates of snowfall rate, particle size, and ice crystal concentration, allowing for an in-depth comparison between seeded and unseeded scenarios.

Building on this initial analysis, the study was expanded to include 13 cloud seeding events across three distinct regions: Lake Tahoe, Santa Rosa Range, and Ruby Mountains. In these cases, ground-based silver iodide generators were used, and the response of the atmosphere

was assessed using a combination of GOES-R satellite data and radar reflectivity mosaics. Key spectral channels from the Advanced Baseline Imager (ABI) were analyzed to extract information about cloud-top temperatures, optical thickness, cloud phase, and water vapor profiles. These data were used not only to track cloud evolution but also to assess whether observable changes in cloud structure and precipitation occurred following seeding.

Results from both modeling and satellite analyses point to a clear conclusion: cloud seeding effectiveness is highly dependent on pre-existing atmospheric conditions. Successful seeding events, those that showed increases in snowfall rates and ice crystal concentrations, typically occurred under conditions of abundant supercooled liquid water, colder cloud tops, and moist mid- to upper-tropospheric layers. These conditions favor ice nucleation and growth processes, allowing the seeded particles to initiate or enhance precipitation. On the other hand, events that lacked these favorable environmental characteristics showed minimal response to seeding, reinforcing the idea that not all clouds are good candidates for weather modification.

Another important outcome of this work is the demonstration of how satellite remote sensing, particularly from geostationary platforms like GOES-R, can be used to support and evaluate cloud seeding operations in near-real time. By monitoring cloud microphysical properties and vertical moisture structure, remote sensing provides a valuable supplement to conventional ground-based measurements and offers a pathway toward more data-driven, adaptive cloud seeding strategies.

In summary, this dissertation contributes to a more nuanced and physically grounded understanding of cloud seeding. By integrating advanced modeling with satellite

observation, it provides a framework for identifying optimal seeding conditions and assessing developments with greater certainty. The findings have practical implications for the design and evaluation of weather modification programs and offer a foundation for integrating cloud seeding into broader regional water management and climate adaptation efforts.

*To Amir, my beloved husband and dearest friend*

*Thank you for always being there for me, for your unwavering support, and for believing in me even when I doubted myself. This achievement would not have been possible without you. This dissertation stands as much on your shoulders as mine. With all my love, I dedicate this work to you.*

## Acknowledgments

There are countless individuals to whom I owe a deep debt of gratitude. Without their expertise, support, and encouragement, this dissertation would not have been possible. Their guidance helped me overcome numerous challenges and achieve my academic goals during my time at the University of Nevada, Reno (UNR).

First and foremost, I would like to express my heartfelt appreciation to my dissertation advisor, Dr. Farnaz Hosseinpour, for giving me the opportunity in 2022 to begin my research at the Desert Research Institute (DRI). Her mentorship has been instrumental in shaping me into an independent researcher. I am especially grateful for her encouragement and unwavering support throughout my Ph.D. journey. I extend my deepest thanks to my co-advisor, Frank McDonough, for his extensive support and mentorship. His expertise in cloud seeding and generous funding during my time at DRI were vital to the success of this research.

I am sincerely grateful to Dr. Ehsan Erfani, whose guidance was crucial in helping me understand and implement the Snow Growth Model for Rimed Snowfall (SGMR). His insights and willingness to share knowledge greatly enriched my work. I would also like to thank my dissertation committee members, Dr. Stanislav Jabuka and Dr. Anna Panorska, for their feedback, valuable comments, and academic support, which helped me strengthen the quality and rigor of my research. Special thanks to Jesse Juchtzer for providing ground-based generator data and for patiently answering my questions throughout this process. I am thankful to the Atmospheric Science graduate program and DRI for creating a supportive and collaborative academic environment. I would like to acknowledge Dr.

Xiaoliang Wang, director of the Atmospheric Sciences graduate program, for his guidance during my Ph.D. studies. I am grateful for the opportunity to get to know and work with dedicated researchers and faculty members at both DRI and UNR, which significantly improved my experience.

Lastly, and most importantly, I offer my deepest and most sincere gratitude to my incredible husband, amazing parents, and beloved sister. Their unconditional love, encouragement, and belief in me have been my greatest source of strength throughout my Ph.D. journey.

## Table of contents

Abstract.....	i
Dedication.....	iv
Acknowledgments .....	v
List of Tables .....	xi
List of Figures .....	xii
1. Introduction.....	1
1.1. Background.....	1
1.1.1. Cloud seeding .....	1
1.1.1.1. Winter orographic cloud seeding.....	6
1.1.1.2. Convective cloud seeding.....	7
1.1.2. Cloud microphysics.....	9
1.1.2.1. Microphysics of warm clouds.....	9
1.1.2.2. Microphysics of cold clouds.....	9
1.1.2.2.1. Homogeneous nucleation.....	10
1.1.2.2.2. Heterogeneous Nucleation and Additional Processes....	10
1.2. Objectives .....	12
1.3. Dissertation Structure.....	13

1.4. References .....	14
2. Quantifying the Influence of Cloud Seeding on Ice Particle Growth and Snowfall Through Idealized Microphysical Modeling.....	18
2.1. Abstract.....	19
2.2. Introduction.....	20
2.3. Data and Methodology.....	26
2.3.1. Datasets.....	26
2.3.2. Snow Growth Model for Rimed Snowfall.....	27
2.4. Results and Discussion.....	32
2.4.1. Atmospheric Condition.....	33
2.4.2. Model Results.....	35
2.5. Conclusions.....	50
2.6. References.....	52
3. Assessing Orographic Cloud Seeding Impacts Through Integration of Remote Sensing from Multispectral Satellite and Radar Data and In Situ Observations in the Western United States.....	59
3.1. Abstract.....	60
3.2. Introduction.....	61

3.2.1. Remote Sensing in Cloud Seeding.....	63
3.2.1.1. Satellite Observations and Technological Developments.....	63
3.2.1.2. Advancements in Geostationary Satellite Capabilities.....	64
3.3. Data and Methodology.....	66
3.3.1. Case study: Wintertime Cloud Seeding in Targeted Western U.S. Regions.....	66
3.3.2. Advanced Baseline Imager of GOES-R Series.....	69
3.3.3. Cloud Microphysical and Atmospheric Properties.....	74
3.3.4. Radar Reflectivity.....	77
3.4. Results and Discussion.....	78
3.4.1. Meteorological Criteria for Effective Cloud Seeding.....	78
3.4.2. Site-Specific Variability in Atmospheric Conditions During Cloud Seeding.....	81
3.4.3. Satellite–Radar Analysis of Tahoe Region Cloud Seeding Events.....	86
3.4.3.1. Seeding Event 1: 11 November 2024.....	86
3.4.3.2. Seeding Event 2: 20 February 2024.....	92
3.4.3.3. Seeding Event 3: 1 February 2024.....	97
3.4.3.4. Seeding Event 4: 4 April 2024.....	101

3.5. Summary and Conclusions .....	105
3.6. References.....	108
3.7. Appendix.....	120
4. Summary and conclusions.....	129
4.1. Recommendation for future work.....	132

## List of Tables

Table 2.1. Model inputs for five cloud seeding events in the Tahoe region.....	28
Table 3.1. GOES Advanced Baseline Imager (ABI) Channels used in this study, including their approximate central wavelength ( $\mu\text{m}$ ), respective maximum spatial resolution (km), and the cloud properties analyzed.....	70
Table 3.2. Summary of Meteorological Conditions During Cloud Seeding Operations.....	80

## List of Figures

Figure 2.1. Conceptual model illustrating the ice particle growth mechanism through clouds integrated into the SGMR. The model demonstrates how snowfall microphysics are simulated, including vapor deposition, aggregation, riming, and ice nucleation mechanisms.....	29
Figure 2.2. Cloud seeding generator locations in the Lake Tahoe region (Base map image created using Google Earth ©) .....	31
Figure 2.3. Combined atmospheric conditions on Event 1 (6 March 2021), Event 2 (16 December 2021), Event 3 (5 March 2022), Event 4 (16 April 2022), and Event 5 (9 March 2021), showing average temperature (°C), maximum temperature (°C), and minimum temperature (°C), average wind speed (km/h), peak wind speed (km/h), and relative humidity (%). Data sourced from weather stations closest to the ground-based generators, as provided by the Western Regional Climate Center.....	35
Figure 2.4. Comparison of the effects of seeding on Event 1 (6 March 2021), Event 2 (16 December 2021), Event 3 (5 March 2022), Event 4 (16 April 2022), and Event 5 (9 March 2021) across four scenarios incorporating diffusion, aggregation, and riming. The analysis includes changes in number concentration.....	37
Figure 2.5. Comparison of the effects of seeding on Event 1 (6 March 2021), Event 2 (16 December 2021), Event 3 (5 March 2022), Event 4 (16 April 2022), and Event 5 (9 March 2021) across four scenarios incorporating diffusion, aggregation, and riming. The analysis includes changes in snowfall rate.....	39
Figure 2.6. Comparison of the effects of seeding on Event 1 (6 March 2021), Event 2 (16 December 2021), Event 3 (5 March 2022), Event 4 (16 April 2022), and Event 5 (9 March 2021) across four scenarios incorporating diffusion, aggregation, and riming. The analysis includes changes in IWC.....	41
Figure 2.7. Comparison of the effects of seeding on Event 1 (6 March 2021), Event 2 (16 December 2021), Event 3 (5 March 2022), Event 4 (16 April 2022), and Event 5 (9 March 2021) across four scenarios incorporating diffusion, aggregation, and riming. The analysis includes changes in fall speed.....	43
Figure 3.1. Locations of ground-based AgI generators used in cloud seeding operations across the Lake Tahoe Area, Ruby Mountains, and Santa Rosa Range in Nevada, shown with red polygons. (Base map image created using Google Earth ©).....	68
Figure 3.2. Box-and-whisker plots depicting the distribution of air temperatures recorded at Tahoe, Santa Rosa, and Ruby locations during the cloud seeding operations.....	82

Figure 3.3. GOES ABI satellite imagery from the cloud seeding event on November 11, 2024, at 20:00 UTC, over the Tahoe region, highlighting multiple spectral bands used for cloud microphysical and thermodynamic analysis. The top row presents visible and near-infrared bands (0.64 $\mu\text{m}$ , 0.86 $\mu\text{m}$ , and 1.61 $\mu\text{m}$ ), the middle row displays infrared window bands (10.3 $\mu\text{m}$ , 11.2 $\mu\text{m}$ , and 12.3 $\mu\text{m}$ ), and the bottom row features water vapor bands (6.2 $\mu\text{m}$ , 6.9 $\mu\text{m}$ , and 7.3 $\mu\text{m}$ ). Satellite imagery from NOAA STAR GOES-West, Pacific Southwest sector.....	89
Figure 3.4. Radar reflectivity images on November 11, 2024. Sequence begins prior to seeding and illustrates the evolution of reflectivity following the initiation of cloud seeding. The images are from the National reflectivity mosaic derived from the NEXRAD (Next Generation Weather Radar) system and correspond to 19:00, 20:00, 20:20, and 20:40 UTC. The area shown is centered over the Lake Tahoe region, spanning parts of northeastern California and western Nevada. Radar images retrieved from the NOAA NCEI Radar Viewer.....	91
Figure 3.5. Same as Figure 3.3, but for February 20, 2024, at 21:51 UTC.....	94
Figure 3.6. Same as Figure 3.4, but for February 20, 2024, showing data at 21:25, 21:50, 22:10, and 22:30 UTC.....	96
Figure 3.7. Same as Figure 3.3, but for February 1, 2024, at 18:16 UTC.....	99
Figure 3.8. Same as Figure 3.4, but for February 1, 2024, showing data at 17:25, 18:15, 18:35, and 18:55 UTC.....	100
Figure 3.9. Same as Figure 3.3, but for April 4, 2024, at 23:21 UTC.....	103
Figure 3.10. Same as Figure 3.4, but for April 4, 2024, showing data at 18:00, 23:00, 23:20, and 23:40 UTC.....	104

# Chapter 1

## Introduction

### 1.1. Background

#### 1.1.1. Cloud seeding

Cloud seeding accelerates the natural process of rain/snow formation. It begins when moisture accumulates around airborne aerosol, reaching a saturation point where it can no longer retain the moisture, causing it to precipitate as rain/snow. It employs additional “nuclei” to facilitate water droplet condensation, with common materials including silver iodide, salt, potassium iodide, dry ice (solid carbon dioxide), and liquid propane due to their efficacy in forming ice crystals at higher temperatures. Cloud seeding is most effective in generating increased snowfall within cloud temperatures ranging from 19 to -4 °F (-7 to -20 °C). Other criteria for successful cloud seeding involve several factors such as the presence of supercooled liquid water, atmospheric instability (without inversions or stable layers), and favorable wind direction and speed to effectively guide seeding particles into the targeted clouds.

The first successful demonstration of cloud seeding was by Vincent Schaefer in 1946. During an experiment in a cold chamber in a laboratory, Schaefer introduced dry ice into a cloud of supercooled water droplets, resulting in snowfall. Subsequently, a successful field test seeding of a natural cloud by airplane was conducted (Schaefer, 1946). Shortly after,

Bernard Vonnegut (Vonnegut, 1947) identified silver iodide as another effective substance for cloud seeding. Silver iodide has a crystal structure like natural ice, making it an effective agent for generating snowfall from supercooled water droplets. Following their groundbreaking work, water resource managers realized the potential of using this technique to boost water supplies in dry areas by augmenting the winter snowpack.

In response to growing water scarcity and water demands, which have worsened due to climate change, many countries are involved in enhancing precipitation. With the significant population growth in the U.S. between 1950 and 2010, especially in the southern and western states authorities are conducting cloud seeding to preserve the existent supply (Kenny et al., 2009; Flossmann et al., 2019; Rauber et al., 2019).

During the winter months in the western United States, snow accumulates in higher coastal ranges and across various elevations in interior mountains, later melting in spring and summer to replenish annual water resources. Motivated by the urgent need for water due to drought in the 1950s and 1960s, pioneering researchers conducted projects to investigate the feasibility of weather modification for enhancing water availability. Initial experiments on orographic cloud seeding, which expanded into comprehensive field studies in the 1970s and 1980s, achieved some success in determining when cloud seeding might increase precipitation, though they did not definitively quantify the extent of this increase.

In 2003, a report by the National Research Council highlighted the lack of conclusive scientific evidence supporting the effectiveness of global weather modification initiatives. However, more recent studies conducted in 2011 over Australia's Snowy Mountains and in 2014 over Wyoming's Medicine Bow Mountains, along with advancements in cloud

seeding modeling, are revealing correlations between cloud seeding and increased precipitation levels.

Manton et al. (2011) conducted several observational studies to investigate the seeding effects using a network of 13 ground generators and 44 precipitation gauges across the Snowy Mountains in Australia. They compared 53 seeding periods with 31 unseeded instances and found a 14% increase in precipitation in the target area compared to natural levels, with a 3% chance of the results being due to sampling issues or natural variability (Manton et al., 2011; Manton and Warren, 2011). In a subsequent phase conducted in 2017, 10 additional ground generators and 17 more precipitation gauges were introduced to the north of the original locations detailed in phase 1, with the analysis divided into two distinct target regions: one to the north and the other to the south. Furthermore, the study methodology was refined to better account for uncertainties in estimating natural precipitation levels. The results indicated that in the southern target area, there was a total fractional increase of 12% above the natural precipitation level at a significance level of 6%, while in the northern target area, this increase was 16 percent at a significance level of 3% (Manton et al., 2017).

Xue et al. (2013) conducted a study utilizing the Weather Research and Forecasting (WRF) model to simulate the impact of ground and airborne cloud seeding across four scenarios near the Payette and Snake River basins in Idaho. Employing a cloud-seeding parameterization within the model, they simulated the effects of seeding, allowing for direct comparison with control simulations, which lacked cloud seeding. The spatial distribution of simulated precipitation variances between the seeded and control

simulations revealed considerable variability across the targeted basin, with increases of up to 2 mm observed in certain instances. However, most affected regions experienced less than 1 mm of additional precipitation. This suggests that findings derived from measurements taken at one location may not accurately reflect the conditions across the entire selected area (Xue et al., 2013).

The 2014 Wyoming Weather Modification Pilot Project (WWMPP) aimed to assess the effect of silver iodide cloud seeding on regional snowfall through several years, randomized statistical analysis, generating 118 practical seeding periods across the Medicine Bow ranges and the Sierra Madre. Although the statistical evaluation of these periods revealed a ~3% seeding effect on precipitation amount, it lacked statistical significance, with a probability of the small observed increase of 28% as indicated by the p-value. This result did not dismiss the possibility of cloud seeding's impact; however, with only 118 cases, differentiating between a modest 3% precipitation increase and inherent weather variability proves challenging. While confirming the 3% effect necessitates a larger sample size, the associated costs, time constraints, and other factors make this impractical. Instead, an alternative approach involved conducting 8946 model simulations based on the 118 cases, utilizing the Weather Research and Forecasting model with cloud-seeding parameterization. These simulations demonstrated an average precipitation enhancement of around 5% (comparable to seedable storms in winter) at designated precipitation gauge sites. Additionally, a complementary study suggested that 27%-30% of wintertime precipitation occurs under conditions favorable for seeding (Ritzman et al., 2015). Consequently, the projected enhancement of annual winter precipitation totals would amount to about 1.5% (Rasmussen et al., 2018).

Friedrich et al. (2020) conducted a study as part of the Seeded and Natural Orographic Wintertime Clouds: the Idaho Experiment (SNOWIE) project, which dispersed silver iodide from an aircraft upwind of the Payette River basin. During these experiments, flights were conducted upwind of or over areas where natural precipitation was minimal. This allowed researchers to accurately identify and monitor the patterns of radar echo and corresponding increases in ground precipitation gauges resulting from cloud seeding. The observed enhancements in snowfall rate during seeding varied from roughly 0.4 mm/hr to 1.2 mm/hr, leading to liquid comparable snowfall increases varying from 0.05 mm to 0.28 mm (Friedrich et al., 2020).

Two primary techniques exist for cloud seeding. The first, known as hygroscopic seeding, focuses on accelerating the merging process of droplets within liquid clouds to form larger, precipitation-ready droplets. This method typically employs the distribution of sizable salt particles at the cloud's base. The second technique, glaciogenic seeding, aims to induce ice formation within supercooled clouds, which then leads to precipitation (Laaksonen and Malila, 2022). This process often involves spreading effective ice-forming agents, like silver iodide or dry ice, throughout the cloud to facilitate heterogeneous nucleation of ice. Alternatively, spraying liquid carbon dioxide can cool the cloud to a point where supercooled droplets freeze spontaneously. Glaciogenic seeding is commonly used for convective clouds or winter orographic clouds. Among these methods, the use of silver iodide (AgI) has been the subject of extensive scientific research, particularly in the context of these cloud types (Laaksonen and Malila, 2022).

#### 1.1.1.1. Winter orographic cloud seeding

During the boreal winter season, the formation of clouds and precipitation over mountains is affected by the orography, as moist air ascends over the terrain near the freezing point, leading to the creation of supercooled liquid water (Flossmann et al., 2019). The fundamental concept behind seeding orographic clouds involves introducing artificial INPs, typically silver iodide (AgI), into SLW. This process encourages ice particle formation at relatively higher temperatures (about  $-5^{\circ}\text{C}$ ), which then grows through processes like deposition and collision, ultimately increasing precipitation over the mountainous areas. This approach, known as glaciogenic seeding, has been validated through both observational and theoretical studies (French et al., 2018; Flossmann et al., 2019).

Within the framework of the Wyoming Weather Modification Pilot Project, Geerts et al. (2010) examined how ground based AgI seeding affects orographic cloud microphysics. They used radar data comparisons between seeded and non-seeded conditions, employing contoured frequency by altitude displays (CFADs) to demonstrate seeding effects, which were found to intensify with higher Froude numbers, indicating less stable airflow. Further studies (e.g., French et al., 2018) have detailed the precipitation enhancement processes in orographic cloud systems, particularly in Idaho's mountainous regions. They also outlined two methods for aircraft based AgI seeding. One involved flying the seeding aircraft at an effective altitude, dispersing INPs horizontally into the cloud using acetone burners or flares. The second method used ejectable flares, deploying from above the supercooled water layer. This second method is especially suitable for mountainous areas, although

there is a risk of the flares extinguishing before reaching the optimal altitude if the aircraft flies too high. Besides, a variety of ground-based seeding techniques exist, including acetone burners, artillery, rockets, and even high-altitude fireworks, aiming to elevate INPs to the desired cloud levels. Nevertheless, the effectiveness of these methods is augmented by remote sensing technology, indicating a preference for direct seeding approaches over ground-based generators for their efficiency in enhancing precipitation.

#### 1.1.1.2. Convective cloud seeding

In clouds formed by surface heating, the complicated relations between atmospheric dynamics and cloud microphysics present various chances to increase precipitation. Two primary approaches are employed for cloud seeding: 1) hygroscopic seeding and 2) glaciogenic seeding. The first approach involves adding sizable CCN to foster the growth of large droplets at the cloud's base, thereby triggering coalescence processes. The second approach introduces INP to encourage ice and mixed-phase processes within the cloud. Hygroscopic seeding agents are typically salts ranging from 0.1 to 10  $\mu\text{m}$  in size (Drofa et al., 2013; Flossmann et al., 2019) and are dispersed in clouds via aircraft using micro powders, ejectable flares, or burn-in-place flares (Bruitjes et al., 2012). Other methods such as artillery shells and ground-based flares and rockets are also used for dispersal into convective clouds. The hygroscopic seeding approach is suitable for cloud systems with a depth of over 1 km below the freezing level, where natural aerosol particles lack large CCN, and updrafts near the cloud base exceed 1 m/s (Tessendorf et al., 2012). Particles that are larger and exhibit greater hygroscopic properties compared to the background

particles are anticipated to undergo accelerated growth via condensation, followed by further enlargement through collisions with other droplets. Moreover, CCN contributes to the tail effect, while also provoking a competition effect that hinders the formation of smaller or less soluble CCN by reducing the ultimate supersaturation levels (Segal et al., 2007). Should the depth of the cloud exceed the freezing threshold, the influence of CCN arising from the warm phase may permeate into the cloud's mixed and ice phases (Lawson et al., 2015). Several studies have demonstrated the efficacy of hygroscopic seeding in enhancing rainfall during continental storms (Tessendorf et al., 2012; Flossmann et al., 2019).

In the process of glaciogenic seeding, substances such as silver iodide (AgI) and dry ice are introduced into clouds to either enhance the concentration of INPs or raise cloud buoyancy through the latent heat released during the SLW freezing process. This introduction of ice particles, known as the "static effect", leads to an increase in latent heat release, referred to as the "buoyancy effect". The complexity of seeding convective cloud systems escalates when it involves mixed-phase processes, intertwining cloud microphysics, dynamics, and environment.

Despite the vast investigation, the link between aerosol particles and ground precipitation remains poorly understood. For instance, when clouds come together, it greatly increases rainfall, cloud cover, and features observed by radar including echo tops and enhanced reflectivity (Sinkevich and Krauss, 2014). Nonetheless, the exact effects are not fully comprehended or recorded.

### 1.1.2. Cloud microphysics

Cloud microphysics focuses on understanding how particles within clouds, like aerosols or raindrops, behave and change, rather than looking at entire cloud shapes or formations. These particles are significantly smaller than the overall cloud and vary in size from less than a micrometer to a few centimeters, placing them on the ‘microscale’ (Lamb, 2015). The study of cloud microphysics reveals that water in clouds can exist in various forms, influenced by a set of seven fundamental microphysical processes, including 1) Collection; 2) Nucleation; 3) Vapor Diffusion; 4) Ice Enhancement; 5) Melting; 6) Breakup; 7) Fallout (Houze, 2014; Lamb, 2015). These processes often occur simultaneously in clouds, creating a complex interplay of different water and ice particle forms in warm and cold clouds.

#### 1.1.2.1. Microphysics of warm clouds

The microphysics of warm clouds, where temperatures are consistently above 0°C, involves processes that occur without the presence of ice. In warm clouds, liquid-phase processes dominate the microphysical behavior, leading to the growth and precipitation of water droplets without the involvement of ice-phase processes.

#### 1.1.2.2. Microphysics of cold clouds

In cold clouds, characterized by temperatures dropping below 0°C, the microphysical processes become complex due to the simultaneous existence of supercooled liquid water droplets and ice crystals (Houze, 2014). These dynamics are closely linked to atmospheric

conditions and temperature changes, significantly affecting the emergence, sustainability, and characteristics of precipitation types like snow, sleet, and hail.

#### 1.1.2.2.1. Homogeneous nucleation

Homogeneous ice nucleation refers to the formation of ice crystals without the assistance of any external particles (Vali et al., 2015; Korhonen, 2021). Homogeneous nucleation from vapor is theoretically possible but highly unlikely in natural conditions due to the need for extreme cold (below  $-65^{\circ}\text{C}$ ) and high supersaturation, which are not typical in the atmosphere. Instead, ice usually forms in clouds through homogeneous nucleation from the liquid phase, where supercooled water droplets freeze. This process is temperature-dependent, with liquid water transitioning to ice at temperatures usually below  $-35$  to  $-40^{\circ}\text{C}$ . Factors such as droplet size and the presence of dissolved substances influence the freezing point (Houze, 2014). Pure water droplets undergo homogeneous freezing when the relative humidity over ice reaches approximately 145% and the temperature drops to about  $-38^{\circ}\text{C}$  (Pruppacher and Klett, 1997). At around  $-38^{\circ}\text{C}$ , molecular potential energy is released, initiating homogeneous freezing (Korhonen, 2021). This process starts with creating an ice embryo, which is essentially a thermodynamically unstable cluster of water molecules arranged in a way that promotes their transition into stable ice (Vali et al., 2015).

#### 1.1.2.2.2. Heterogeneous Nucleation and Additional Processes

When the freezing process involves impurities such as aerosol particles, there are four mechanisms of heterogeneous ice nucleation. Moreover, the aerosol particles acting as ice nuclei are known as ice-nucleating particles (INPs) (Korhonen, 2021).

- Deposition nucleation:

Deposition nucleation occurs when ice crystals form directly from supersaturated vapor on INP without the initial formation of liquid water (Houze, 2014; Vali et al., 2015). This is the only process that can happen even under conditions where the air is not saturated, indicating no liquid water shapes on insoluble particles. Ice can form directly from vapor without turning into liquid because ice has a lower saturation vapor pressure than liquid water (Korhonen, 2021).

When freezing happens in conditions where there is an excess of water vapor and INPs are present, it's common for the liquid to form on these particles. These particles can serve as Cloud Condensation Nuclei (CCN) as well as INPs. Consequently, under conditions of water supersaturation that lead to freezing, there are three distinct mechanisms through which heterogeneous ice nucleation can occur.

- Immersion freezing:

Among the four modes, immersion freezing is considered the most prevalent form of ice nucleation in the atmosphere. Ice formation is triggered by particles other than the initial CCN within a supercooled droplet. This process starts when an INP submerged in a supercooled liquid droplet initiates ice formation (Murray et al., 2012).

- Contact nucleation:

This occurs when an ice nucleus in the air contacts a supercooled droplet. Contact freezing is a process that begins at the droplet's surface, opposite to immersion freezing, where the INP either directly contacts the liquid or emerges at the point where air, liquid, and particle converge, known as the air-liquid-particle triple interface (Vali et al., 2015). While the distinction between contact and immersion freezing's impact is debated, specific INPs are more prone to trigger nucleation through contact freezing (Shaw et al., 2005; Korhonen, 2021).

- Condensation nucleation:

Condensation freezing occurs when water first condenses on a particle before it freezes. However, this mode can be hard to differentiate from immersion freezing (Vali et al., 2015). In this study, parameterizations for deposition and condensation were adapted from research conducted by Liu et al., 2007. Similarly, the approaches to immersion-freezing nucleation and contact-freezing nucleation were informed by the study of Xue et al., 2013.

The effectiveness of nucleation is influenced by factors such as water vapor content, the exposed surface area of the nucleus material, and particularly temperature, as higher temperatures increase surface tension and elastic strain, reducing nucleation efficiency. Ice nucleation is more likely at lower temperatures and on surfaces with a crystal lattice like ice. Natural substances such as mineral dust and biological particles are common ice nuclei, with their nucleation efficiency varying with temperature and concentration (Houze, 2014).

## 1.2. Objectives

The main goal of this dissertation is to improve our understanding of cloud seeding mechanisms over the western United States by addressing the trade-offs between efficiency, precision, and accuracy in climate modeling, particularly in the simulation of microphysical processes. The research emphasizes a microphysical perspective and integrates satellite remote sensing to provide a broader and more accurate depiction of atmospheric phenomena.

The study pursues four specific objectives: (1) to incorporate satellite remote sensing data to enhance observational support and model validation; (2) to apply the Snow Growth Model for Rimed Snowfall to simulate the vertical evolution of ice particle size distributions as a function of relative humidity and supersaturation; (3) to perform controlled model experiments under a range of meteorological conditions, comparing seeded and non-seeded scenarios to evaluate changes in snowfall production; and (4) to improve the representation of microphysical processes by incorporating ice crystal nucleation alongside vapor deposition, aggregation, and riming, allowing for a more comprehensive simulation of cloud microphysics. Through these objectives, the study seeks to contribute to the refinement of seeding strategies and the advancement of predictive atmospheric modeling tools.

### 1.3. Dissertation Structure

This dissertation is organized into four chapters. Chapter 1 introduces the topic of cloud seeding, discusses its various types, and provides foundational background on cloud microphysics. Chapter 2 presents research published in the *Atmosphere* journal in 2024,

which addresses objectives 2, 3, and 4 outlined in Section 1.2. In this study, the SGMR model was used to simulate ice particle growth under varying humidity and supersaturation conditions, evaluate changes in snowfall between seeded and non-seeded scenarios, and enhance the representation of cloud microphysical processes by incorporating nucleation, deposition, aggregation, and riming. As this chapter is based on the published work, it contains substantial portions of the same text as the 2024 article. Chapter 3 includes research submitted to *Remote Sensing* in 2025, which focuses on objective 1 of Section 1.2. This study employed a satellite–radar integration framework, along with in-situ observations, to incorporate satellite remote sensing data for improved observational support and model validation. Since this chapter is derived from the submitted manuscript, it also contains significant overlap with the original text, which is currently under review at the time of this writing. Finally, Chapter 4 concludes the dissertation by summarizing the key research findings and contributions.

#### 1.4. References

Bruintjes, R. T., V. Salazar, T. A. Semeniuk, P. Buseck, D. W. Breed, and J. Gunkelman, 2012: Evaluation of hygroscopic cloud seeding flares. *J. Wea. Modif.*, 44, 69–94, <https://journalofweathermodification.org/index.php/JWM/article/view/85>.

Drofa, A. S., V. G. Eran'kov, V. N. Ivanov, A. G. Shilin, and G. F. Iskevich, 2013: Experimental investigations of the effect of cloud-medium modification by salt powders. *Izv. Atmos. Ocean. Phys.*, 49, 298–306, <https://doi.org/10.1134/S0001433813030043>.

Flossmann, Andrea & Manton, Michael & Abshaev, Ali & Bruintjes, Roelof & Murakami, Masataka & Prabha, Thara & Yao, Zhanyu. (2019). Review of Advances in Precipitation Enhancement Research. *Bulletin of the American Meteorological Society*. 100. 10.1175/BAMS-D-18-0160.1.

French, J. R., and Coauthors, 2018: Precipitation formation from orographic cloud seeding. *Proc. Natl. Acad. Sci. USA*, 115, 1168–1173, <https://doi.org/10.1073/pnas.1716995115>.

Friedrich, K., Ikeda, K., Tessendorf, S. A., French, J. R., Rauber, R. M., Geerts, B., ... & Dawson, N. (2020). Quantifying snowfall from orographic cloud seeding. *Proceedings of the National Academy of Sciences*, 117(10), 5190-5195.

Geerts, B., Q. Miao, Y. Yang, R. Rasmussen, and D. Breed, 2010: An airborne profiling radar study of the impact of glaciogenic cloud seeding on snowfall from winter orographic clouds. *J. Atmos. Sci.*, 67, 3286–3302, <https://doi.org/10.1175/2010JAS3496.1>.

Houze Jr, R. A. (2014). *Cloud dynamics*. Academic press.

Kenny, J. F., N. L. Barber, S. S. Hutson, K. S. Linsey, J. K. Lovelace, and M. A. Maupin, 2009: Estimated use of water in the United States in 2005. U.S. Geological Survey Circular 1344, 52 pp., <https://pubs.usgs.gov/circ/1344/pdf/c1344.pdf>.

Korhonen, K. (2021). *Ice Nucleation Induced by Atmospheric Particulate Matter: Investigation Using a Portable Continuous Flow Diffusion Chamber Instrument* (Doctoral dissertation, Suomen Aerosolitutkimusseura ry).

Laaksonen, A., & Malila, J. (2022). Ice nucleation. In A. Laaksonen & J. Malila (Eds.), *Nucleation of Water* (pp. 209-248). Elsevier. <https://doi.org/10.1016/B978-0-12-814321-6.00018-X>

Lamb, D. Clouds and Fog, Cloud Microphysics. In *Encyclopedia of Atmospheric Sciences*; Elsevier: Amsterdam, The Netherlands, 2015; Volume 2, pp. 133–140. ISBN 978-0-12-382225-3.

Liu, X., Penner, J. E., Ghan, S. J., & Wang, M. (2007). Inclusion of ice microphysics in the NCAR Community Atmospheric Model version 3 (CAM3). *Journal of Climate*, 20(18), 4526-4547.

Manton, M. J., & Warren, L. (2011). A confirmatory snowfall enhancement project in the Snowy Mountains of Australia. Part II: Primary and associated analyses. *Journal of applied meteorology and climatology*, 50(7), 1448-1458.

Manton, M. J., Peace, A. D., Kemsley, K., Kenyon, S., Speirs, J. C., Warren, L., & Denholm, J. (2017). Further analysis of a snowfall enhancement project in the Snowy Mountains of Australia. *Atmospheric Research*, 193, 192-203.

Manton, M. J., Warren, L., Kenyon, S. L., Peace, A. D., Bilish, S. P., & Kemsley, K. (2011). A confirmatory snowfall enhancement project in the Snowy Mountains of Australia. Part I: Project design and response variables. *Journal of applied meteorology and climatology*, 50(7), 1432-1447.

- Murray, B. J., O'sullivan, D., Atkinson, J. D., & Webb, M. E. (2012). Ice nucleation by particles immersed in supercooled cloud droplets. *Chemical Society Reviews*, 41(19), 6519-6554.
- Pruppacher, H. R., & Klett, J. D. (1997). *Microphysics of clouds and precipitation*, Kluwer Acad. Morwell Mass.
- Rasmussen, R. M., Tessendorf, S. A., Xue, L., Weeks, C., Ikeda, K., Landolt, S., ... & Lawrence, B. (2018). Evaluation of the Wyoming Weather Modification Pilot Project (WWMPP) using two approaches: Traditional statistics and ensemble modeling. *Journal of Applied Meteorology and Climatology*, 57(11), 2639-2660.
- Ritzman, J. M., Deshler, T., Ikeda, K., & Rasmussen, R. (2015). Estimating the Fraction of Winter Orographic Precipitation Produced under Conditions Meeting the Seeding Criteria for the Wyoming Weather Modification Pilot Project. *Journal of Applied Meteorology and Climatology*, 54(6), 1202-1215. <https://doi.org/10.1175/JAMC-D-14-0163.1>
- Rauber, R. M., Geerts, B., Xue, L., French, J., Friedrich, K., Rasmussen, R. M., Tessendorf, S. A., Blestrud, D. R., Kunkel, M. L., & Parkinson, S. (2019). Wintertime Orographic Cloud Seeding—A Review. *Journal of Applied Meteorology and Climatology*, 58(10), 2117-2140. <https://doi.org/10.1175/JAMC-D-18-0341.1>
- Schaefer, V. J. (1946). The production of ice crystals in a cloud of supercooled water droplets. *Science*, 104(2707), 457-459.
- Shaw, R. A., Durant, A. J., and Mi, Y.: Heterogeneous surface crystallization observed in undercooled water, *J. Phys. Chem. B*, 109,9865–9868, doi:10.1021/jp0506336, 2005.
- Sinkevich, A. A., and T. W. Krauss, 2014: Changes in thunderstorm characteristics due to feeder cloud merging. *Atmos. Res.*, 142, 124–132, <https://doi.org/10.1016/j.atmosres.2013.06.007>.
- Tessendorf, S. A., and Coauthors, 2012: The Queensland Cloud Seeding Research Program. *Bull. Amer. Meteor. Soc.*, 93, 75–90, <https://doi.org/10.1175/BAMS-D-11-00060.1>.
- Vali, G., DeMott, P. J., Möhler, O., & Whale, T. F. (2015). A proposal for ice nucleation terminology. *Atmospheric Chemistry and Physics*, 15(18), 10263-10270.
- Vonnegut, B. (1947). The nucleation of ice formation by silver iodide. *Journal of applied physics*, 18(7), 593-595.
- Xue, L., Hashimoto, A., Murakami, M., Rasmussen, R., Tessendorf, S. A., Breed, D., ... & Blestrud, D. (2013). Implementation of a silver iodide cloud-seeding parameterization in WRF. Part I: Model description and idealized 2D sensitivity tests. *Journal of applied meteorology and climatology*, 52(6), 1433-1457.

Xue, L., Tessendorf, S. A., Nelson, E., Rasmussen, R., Breed, D., Parkinson, S., & Blestrud, D. (2013). Implementation of a silver iodide cloud-seeding parameterization in WRF. Part II: 3D simulations of actual seeding events and sensitivity tests. *Journal of Applied Meteorology and Climatology*, 52(6), 1458-1476.

## **Chapter 2**

# **Quantifying the Influence of Cloud Seeding on Ice Particle Growth and Snowfall Through Idealized Microphysical Modeling**

This chapter is an adapted version of the following publication:

Mehdizadeh, G., Erfani, E., McDonough, F., & Hosseinpour, F. (2024). Quantifying the Influence of Cloud Seeding on Ice Particle Growth and Snowfall Through Idealized Microphysical Modeling. *Atmosphere*, 15(12), 1460.  
<https://doi.org/10.3390/atmos15121460>

## 2.1. Abstract

Cloud seeding is a weather modification technique for enhancing precipitation in arid and semi-arid regions, including the Western U.S. However, designing an optimal cloud seeding operation based on comprehensive evaluation metrics, such as seeding agent dispersion and atmospheric conditions, has yet to be thoroughly explored for this region. This study investigated the impacts of cloud seeding, particularly utilizing silver iodide, on ice particle growth within clouds through numerical modeling. By leveraging the Snow Growth Model for Rimed Snowfall (SGMR), the microphysical processes involved in cloud seeding across five distinct events were simulated. The events were in the Lake Tahoe region, nestled within the Sierra Nevada Mountain ranges in the Western U.S. This model was executed based on six primary variables, including cloud top height, cloud base height, cloud top temperature, cloud base temperature, liquid water content, and ice water content. This study incorporated datasets from the Modern-Era Retrospective Analysis for Research and Applications Version 2 and the Clouds and the Earth Radiant Energy System. The findings revealed the importance of ice nucleation, aggregation, diffusion, and riming processes and highlighted the effectiveness of cloud seeding in enhancing ice particle number concentration, ice water content, and snowfall rates. However, event-specific analyses indicated diverse precipitation responses to cloud seeding based on initial atmospheric conditions. The SGMR modeling hints at the importance of improving ice microphysical processes and provides insights for future cloud seeding research using regional and global climate models.

## 2.2. Introduction

Cloud seeding, a prevalent weather modification technique, involves introducing substances such as silver iodide (AgI) into clouds to change cloud particle properties and increase precipitation [1]. This method is particularly valuable in arid and semi-arid areas worldwide, where the growing population has a boosted demand for water [2]. Therefore, weather modification could reduce the effects of drought on human communities [2]. The change in precipitation as a result of cloud seeding has been shown by a number of studies. In observational studies by Manton et al. (2011) [3], a network of 13 ground generators and 44 precipitation gauges in the Snowy Mountains, Australia, showed a 14% increase in precipitation during 53 seeding periods compared to 31 unseeded instances. That study was later expanded [4] with 10 additional ground generators and 17 more gauges, enhancing the analysis. This expansion led to a 12% increase in precipitation in the southern target area at a 6% significance level and a 16% increase in the northern area at a 3% significance level. Further evidence comes from the 2014 Wyoming Weather Modification Pilot Project (WWMPP), which assessed the effect of AgI cloud seeding on snowfall through a randomized analysis of 118 seeding periods across the Medicine Bow ranges and the Sierra Madre in southeastern Wyoming [5]. Although the results suggested a ~3% increase in precipitation, this was not statistically significant. To better understand the effects, simulations using the WRF model showed an average precipitation enhancement of 5%. Additionally, studies indicated that 27–30% of winter precipitation occurs under conditions suitable for seeding [6], projecting an annual winter precipitation increase of about 1.5% [5]. Another significant study was conducted by Friedrich et al. (2020) [7] as part of the Seeded and Natural Orographic Wintertime Clouds: the Idaho Experiment (SNOWIE)

project. In this study, AgI was dispersed from an aircraft upwind of the Payette River basin. The flights were conducted in areas with minimal natural precipitation, enabling accurate identification and monitoring of radar echo patterns and the corresponding increases in ground precipitation due to cloud seeding. The observed enhancements in snowfall rate during seeding varied from approximately 0.4 mm/h to 1.2 mm/h [7].

The idea of artificially enhancing precipitation is appealing to water resource managers, as it could contribute to balancing and sustaining water supply and demand year-round [2,8,9]. Significant amounts of freshwater are introduced into Earth's hydrological cycle as precipitation from clouds [2,10]. Between 1970 and 2020, the population of the United States increased more than sixty percent, transitioning from rural to urban regions [11]. The population grew most in the southern and western states [12]. Communities in the western states facing water shortages and increasing demands turned to weather modification techniques in order to expand their water resources [12]. Research indicates that in the coming decades, water is expected to become a scarcer resource due to the ever-increasing population and climate change, endangering snow reservoirs across the western mountains [12,13].

Two primary techniques exist for cloud seeding: hygroscopic and glaciogenic seeding. Hygroscopic seeding accelerates the coalescence of droplets within liquid clouds to form larger, precipitation-ready droplets. This method typically involves distributing salts varying in size from 0.1 to 10  $\mu\text{m}$  at the cloud base [14,15]. In contrast, glaciogenic seeding aims to induce ice formation within clouds containing supercooled liquid water (SLW) [16]. This technique often employs ice-forming agents, such as AgI or dry ice, to facilitate

the heterogeneous nucleation of ice. Glaciogenic seeding is commonly applied to convective or winter orographic clouds [12]. In convective clouds formed by surface heating, the interplay between dynamics and microphysics presents various possibilities to enhance precipitation [15]. In glaciogenic seeding, seeding agents are introduced into clouds to increase the concentration of ice-nucleating particles (INPs) as well as enhance the cloud's buoyancy through the release of latent heat from SLW freezing. Both effects are anticipated to happen simultaneously because the formation of ice particles leads to latent heat release [15,17,18].

Precipitation in wintertime orographic clouds is affected by regional orography, with SLW forming as moist air ascends over mountain ranges [15,19]. Orographic cloud seeding involves introducing INPs into the SLW to generate ice particles at temperatures of about  $-5^{\circ}\text{C}$ , which grow through collision and deposition [9,15]. The effects of ground-based seeding of AgI on the orographic cloud microphysics were examined by Geerts et al. (2010) [20] as part of the Wyoming Weather Modification Pilot Project (WWMPP) [21]. By comparing radar data from seeded and unseeded flights utilizing contoured frequency by altitude displays (CFADs), they identified an increased seeding impact with higher Froude numbers, indicating reduced flow stability. Further, a record of precipitation enhancement processes in wintertime orographic clouds over southwestern Idaho was provided by French et al. (2018) [9]. They outline two aircraft seeding methods with AgI, consisting of burn in place, where INPs are released horizontally from the aircraft at effective seeding heights, and ejectable flares, deployed at or above the supercooled water level, suitable for mountainous areas but with risks of burnout. Ground-based seeding strategies, such as acetone burners, artillery shells, and rockets [22], face challenges in assuring that INPs

arrive at the right cloud level. Remote sensing can track seeded material, and modeling and observation analyses indicate that direct seeding is more influential than ground-based methods [23,24].

Previous studies have primarily focused on employing seeding to enhance precipitation [5,9,12] or for hail damage mitigation [25,26]. Observational studies provide real-world data to validate models and offer detailed insights into cloud seeding processes, which are essential for directing future research and improving weather modification techniques. However, while numerous observational studies [3,5,27] have attempted to investigate the effects of cloud seeding on seasonal precipitation levels, their estimation through statistical analyses and observations presents notable challenges. First, there is the issue of identifying the location and timing of the seeded clouds within the natural clouds (absence of natural control); second, the complexity of identifying seeding effects and detecting an increase in surface precipitation [28]; third, the cost of long-term seeding experimentation [29]. Therefore, advancements in numerical models that simulate the physics of cloud seeding and cloud processes, validated by observational data, are proving crucial [12].

Numerical models are valuable for effectively evaluating and quantifying the effects of cloud seeding [12]. Xue et al. (2013) [24] showed different outcomes from ground-based versus aircraft seeding in the Payette and Snake River basins, Idaho. Further, they utilized the 2D Weather Research and Forecasting (WRF) model integrated with a prognostic aerosol model with cloud seeding parameters. The study revealed significant spatial variability in precipitation, with increases up to 2 mm in some areas, but most regions experienced less than 1 mm of additional precipitation. This indicates that localized

measurements may not represent conditions across the entire area [24]. Similarly, four cloud seeding cases in the same area, conducted during a snow trace chemistry field campaign from 2003 to 2005, were simulated by Xue et al. (2017) [30]. Using the WRF model in large eddy simulation mode with a 667 m grid spacing, two airborne and two ground-based events were examined. The results, compared with soundings, Snowpack Telemetry (SNOTEL) site precipitation and silver concentrations in snow samples, showed that the simulated concentrations matched the observed data's magnitude and spatial distribution [30]. Furthermore, large eddy simulation models have been utilized in numerous studies, e.g., [31,32], to explore AgI seeding in orographic clouds. Their findings suggest that a limitation of practical seeding is the vertical distribution of seeding agents and their efficiency in reaching the clouds, and, therefore, cloud dynamics is not greatly influenced by seeding. Although numerical model simulations offer insights into the influence of seeding, it is essential to validate them in the real atmosphere. Regional climate simulations with a resolution of 6 km or lower [13,33,34] have indicated that modern mesoscale models, using the latest microphysical schemes, can simulate natural precipitation in complex terrains during the cold season, and it is possible to simulate seasonal snowfall with an accuracy that approaches within 10% of observations. Before this advancement, model uncertainty hindered scientists from using cutting-edge models for orographic cloud seeding [12]. Following these achievements, models are now being used to assess orographic cloud seeding projects [5].

Three-dimensional (3D) cloud models in cloud seeding studies offer significant advantages by providing a comprehensive spatial representation of cloud dynamics, turbulence, and microphysical processes. For instance, 3D cloud models can capture the interactions

between terrain and cloud structures, making them particularly effective for evaluating cloud seeding impacts in complex environments. Moreover, they are useful in assessing the domain for which seeding is effective. Studies demonstrated the use of 3D models in simulating deep convective clouds, which helped in better understanding the dispersion and activation of AgI [35,36,37,38].

Despite these advantages, 3D models are analytically and computationally expensive and may also face limitations in ensuring complete activation of seeding agents due to stagnant flow regions within the cloud [36,39]. Using a 1D model allows us to isolate various microphysical processes and assess their relative strengths. The Snow Growth Model (SGM) [40] was designed to study snow and ice microphysical processes with great accuracy and computational efficiency. This model proves especially advantageous since satellite measurements of cloud properties are not available or reliable at the bottom of clouds, offering a dependable method for the growth of snow and ice from the cloud top to the cloud bottom using main microphysical processes. Building on prior research [41,42], this study contains substantial enhancements to the SGM, including the incorporation of the riming process and ice heterogeneous nucleation. With these updates, the model was termed the Snow Growth Model for Rimed Snowfall (SGMR).

This study suggests an innovative application of the SGMR for cloud seeding in various background conditions, enhancing our comprehension of ice nucleation and the development of ice growth throughout the cloud. Section 3 describes the methodology used in this study. Section 4 discusses the results, including atmospheric conditions and model outputs. Finally, the conclusions are presented in Section 5.

## 2.3. Data and Methodology

### 2.3.1. Datasets

The Modern-Era Retrospective Analysis for Research and Applications, Version 2 (MERRA-2) [43], is used here to investigate meteorological variables. MERRA-2 is NASA's atmospheric reanalysis from 1980 to the present, utilizing an advanced version of the Goddard Earth Observing System Model, Version 5 (GEOS-5) [44] data assimilation system. All datasets from MERRA-2 are distributed on a constant horizontal grid, featuring 576 longitudinal points and 361 latitudinal points. This design corresponds to a grid resolution of  $0.625^\circ$  longitude by  $0.5^\circ$  latitude. Additionally, the data are structured across 72 model layers [45], enabling detailed atmospheric analysis.

Moreover, the Clouds and the Earth Radiant Energy System (CERES) [46] is employed to collect cloud variables. CERES is designed for the Earth Observing System (EOS) [46,47,48] and encompasses solar and terrestrial radiation fluxes as well as various ice and liquid cloud properties at specific vertical levels. It is a global dataset, and its spatial coverage relies on the satellite orbit, varying from about 20 km at nadir for Single Scanner Footprint (SSF) products to 1 degree by 1 degree (latitude by longitude) for gridded daily and monthly averages. We used 1-degree gridded daily data in this study. CERES cloud characteristics are specified through concurrent measurements from different EOS tools, such as the Moderate-Resolution Imaging Spectroradiometer (MODIS) [49]. MODIS, on NASA's Terra and Aqua satellites, has been used to retrieve global cloud and aerosol properties and atmospheric conditions [50]. While CERES starts with radiative measurements, retrieval algorithms are essential in generating the full suite of CERES data

products, including cloud characteristics. The apparent precision in these values reflects the data retrieval and processing techniques rather than direct measurement accuracy. In this study, the model is driven using MERRA-2 and CERES datasets.

### 2.3.2. Snow Growth Model for Rimed Snowfall

The Snow Growth Model for Rimed Snowfall (SGMR) is a one-dimensional, analytically based microphysical model that is computationally efficient, making it a cost-effective option for modeling processes involved in the growth of ice and snow particles. It is particularly valuable in situations where observational data at the surface or cloud base are either unavailable or uncertain, providing a reliable means of simulating snow growth even in the absence of direct measurements.

The Snow Growth Model (SGM) [40] was initially developed as a process-based model to simulate aggregation and vapor deposition processes, disregarding the impacts of updraft and riming due to relatively weak updrafts and low supercooled liquid water content (LWC). This is specific to mid-latitude cyclones in continental areas of the United States during the winter season.

Over time, progress was made to improve microphysical processes [41] by incorporating the riming process [42,51] to upgrade the vapor diffusional mass growth rate, ice particle mass–dimension, project area–dimension, and fall speed–dimension relationships. These improvements were highlighted by integrating the riming process into the model, which led to its updated designation as the Snow Growth Model for Rimed Snowfall (SGMR).

The SGMR in this study has been further developed to include the nucleation process, crucial for accurately simulating the effects of cloud seeding. By incorporating nucleation, the SGMR can more reliably simulate how substances (e.g., silver iodide) used in cloud seeding affect precipitation. Within the SGMR, ice nucleation for four heterogeneous nucleation processes (covering condensation, deposition, contact, and immersion processes) has been implemented within the temperature range of  $-40\text{ }^{\circ}\text{C}$  to  $0\text{ }^{\circ}\text{C}$ , following the formulations from Liu et al. (2007) [52]. Within the seeding plume, an AgI mean radius of 50 nanometers is assumed [24], with an AgI number concentration of  $700\text{ cm}^{-3}$  [53], and the plume extends to the lowest 800 m of the cloud. Another assumption in the model is that, in the case that IWC exceeds  $0.05\text{ g/m}^3$  at the top of the cloud, the model will select this threshold value (Table 2.1). Based on previous studies [54,55], this approach is expected to yield a mean diameter smaller than 3000 microns within the cloud layer, keeping it within a physical range.

Table 2.1. Model inputs for five cloud seeding events in the Tahoe region.

Event	Date	Cloud Top Height (km)	Cloud Base Height (km)	Cloud Top Temperature ( $^{\circ}\text{C}$ )	Cloud Base Temperature ( $^{\circ}\text{C}$ )	LWC ( $\text{g/m}^3$ )	IWC ( $\text{g/m}^3$ )
1	6 March 2021	4.9	3.3	-19	-9	0.16	0.05
2	16 December 2021	3.9	2.0	-13	-3	0.25	0.05
3	5 March 2022	5.0	2.2	-23	-8	0.10	0.05
4	16 April 2022	4.0	2.5	-11	-4	0.16	0.05
5	9 March 2021	4.1	2.2	-21	-6	0.20	0.05

The process of ice particle growth within clouds involves several mechanisms, each playing an integral role in shaping precipitation. These processes are illustrated in the

conceptual model, as indicated in Figure 2.1. The mechanisms include vapor deposition, where water vapor condenses onto ice nuclei; aggregation, which involves the collision and merging of ice crystals; riming, where supercooled water droplets freeze upon contact with ice crystals; and heterogeneous ice nucleation, when ice crystals form on the surfaces of aerosol particles. These fundamental microphysical processes are integrated into the SGMR to enable the simulation of ice microphysics.

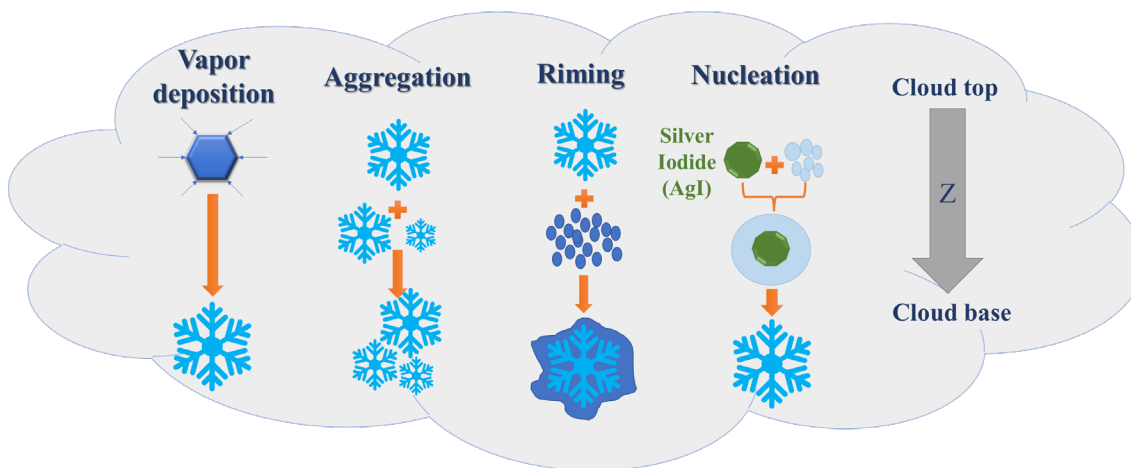


Figure 2.1. Conceptual model illustrating the ice particle growth mechanism through clouds integrated into the SGMR. The model demonstrates how snowfall microphysics are simulated, including vapor deposition, aggregation, riming, and ice nucleation mechanisms.

SGMR uses inputs from a comprehensive array of variables, including cloud top and base height, temperature, maximum LWC in the cloud layer, and ice water content (IWC) near the top cloud. Subsequently, the model simulates the growth behavior of ice particles in response to forcing data. The model runs both with and without considering cloud seeding, a critical factor in our study. This approach aims to evaluate how cloud seeding influences

various parameters: (a) number concentration, referring to the number of ice particles present per volume of air; (b) IWC, representing the mass mixing ratio of ice per volume of air; (c) mass-weighted terminal fall speed, which denotes the velocity at which ice particles descend within the cloud; and (d) snowfall rate, which is the vertical flux of IWC or IWC multiplied by fall speed, indicating the rate at which snow falls from the atmosphere.

Figure 2.2 showcases the geographical locations of cloud seeding ground-based generators in the Lake Tahoe region across five locations, ranging in elevation between 1500 and 2500 m. The specific generator sites are Cisco, Ward, Barker, Bunker, and Morattini, operated by the Desert Research Institute (DRI). These generators are strategically positioned to optimize the cloud seeding process and enhance precipitation levels in targeted areas. Cloud seeding operations are conducted during the winter season, specifically from November to May.

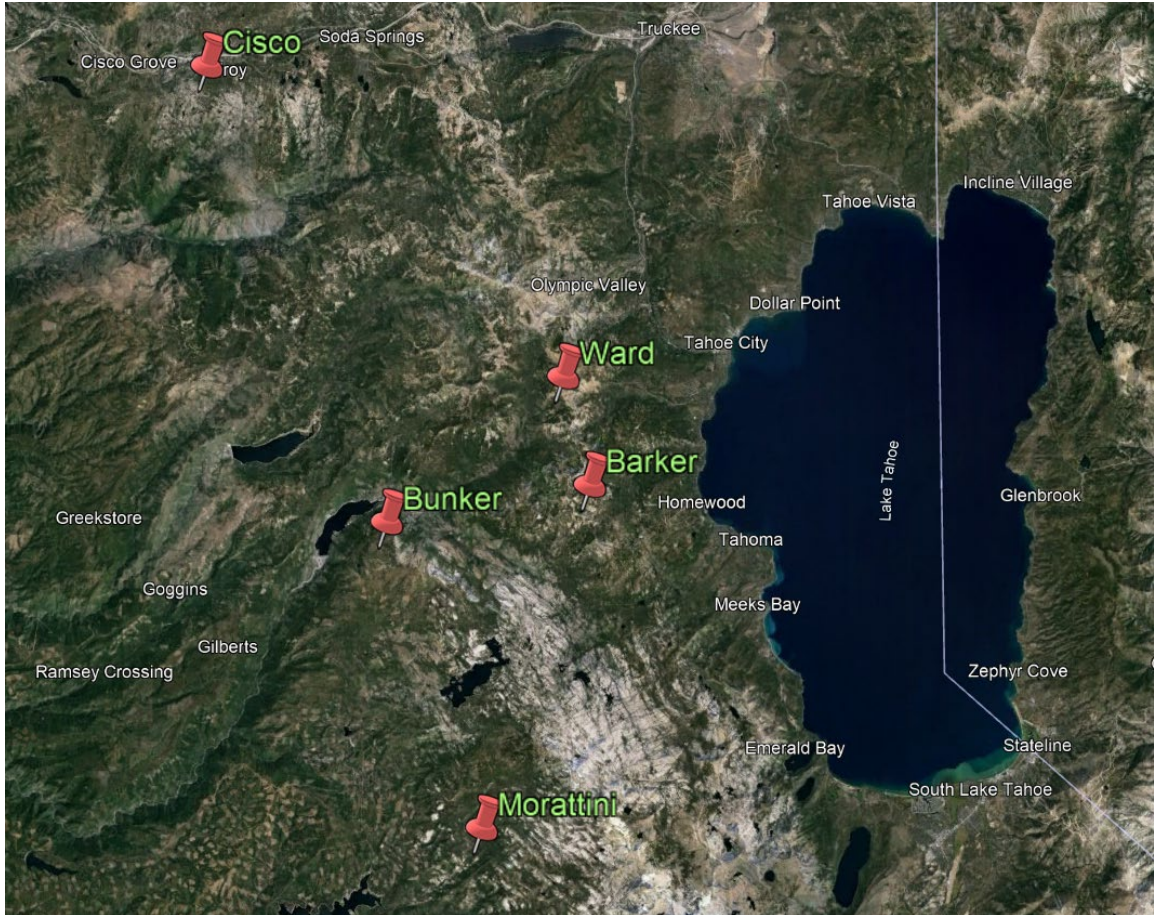


Figure 2.2. Cloud seeding generator locations in the Lake Tahoe region (Base map image created using Google Earth ©).

The SGMR model was applied to analyze five distinct cloud seeding occurrences in the Tahoe region on 6 March 2021, 16 December 2021, 5 March 2022, 16 April 2022, and 9 March 2021 (Table 2.1). The required model inputs are sourced from CERES satellite and MERRA-2 reanalysis datasets. Model inputs include cloud top and base heights (km), cloud top and cloud base temperatures ( $^{\circ}\text{C}$ ), liquid water content (LWC), and ice water content (IWC) measured ( $\text{g}/\text{m}^3$ ). Table 2.1 illustrates the specific model inputs utilized for five seeding events in the Tahoe area. Based on the analysis of cloud characteristics during

these events, different types of orographic clouds were identified. The cloud types observed on 6 March 2021, 5 March 2022, and 9 March 2021 can be classified as “AltoCumulus” due to their moderate cloud heights, mixed-phase content, and temperature profiles, which are indicative of altocumulus formation under orographic lifting conditions. The clouds present during the seeding events on 16 December 2021 and 16 April 2022 can be classified as “Stratocumulus”, characterized by lower cloud heights and higher liquid water content, consistent with the typical features of Stratocumulus clouds.

#### 2.4. Results and Discussion

This section presents the findings of our study on the cloud seeding mechanism. The main objective was to simulate the growth behavior of ice particles within clouds. The variations in cloud top and base heights, temperatures, LWC, and IWC across five events, as presented in Table 2.1, provide insights into the differing microphysical properties of the clouds. The vertical extent of the cloud layers during each event was determined by measuring the cloud’s top and base heights. On 6 March 2021, the cloud top was at 4.9 km, and the base was at 3.3 km, indicating a relatively thick cloud layer (thickness of 1.6 km). During the second event (16 December 2021), the cloud top was at 3.9 km, with a base at 2 km, suggesting a thicker yet lower cloud. The event on 5 March 2022 showed cloud top and base heights of 5 and 2.2 km, respectively.

Furthermore, on 16 April 2022, the cloud thickness was 1.5 km, nearly similar to Event 1. The cloud top at 4.1 km and the base at 2.2 km presented a relatively thick layer in the last event, on 9 March 2021. The temperatures at the cloud tops ranged from  $-23$  °C to  $-11$  °C. The coldest cloud tops were on 5 March 2022, where the cloud had the highest altitude

among all events, and the warmest was on 16 April 2022. The temperatures at the cloud bases varied from  $-9^{\circ}\text{C}$  to  $-3^{\circ}\text{C}$ . The coldest base temperature was observed on 6 March 2021 and the warmest on 16 December 2021. The values of temperature within the cloud layer are critical for determining various processes and properties, such as vapor deposition, nucleation, and viscosity.

Additionally, LWC and IWC measurements indicate the amounts of supercooled cloud droplets and ice particles in the clouds. LWC showed considerable variability, with values ranging from  $0.1\text{ g/m}^3$  to  $0.25\text{ g/m}^3$ . The highest amount was observed on 16 December 2021, while the lowest was on 5 March 2022. These differences in cloud properties are crucial for understanding cloud behavior and are significant for weather modification and atmospheric research applications. The values of IWC at the cloud top are important to determine the change in most ice microphysical variables within the cloud layer. The values of LWC affect the effectiveness of the riming process.

#### 2.4.1. Atmospheric Condition

The atmospheric conditions (depicted in Figure 2.3) of these five events were also monitored at the weather stations [56] nearest to the ground-based generators. At the first event, the average temperature was  $-3^{\circ}\text{C}$ , with a maximum of  $0^{\circ}\text{C}$  and a minimum of  $-6^{\circ}\text{C}$ , at Bunker Station, which is situated at an elevation of 2293 m. Following this, data from the NorthStar weather station, positioned at an elevation of 2625 m, on 16 December 2021, indicated that the average air temperature was  $-7^{\circ}\text{C}$ , with variations between a high of  $-6$  and a low of  $-9^{\circ}\text{C}$ . Wind speeds averaged 13 km/h, with occasional peaks reaching 58 km/h, mainly from the west-southwest (259 degrees). Subsequently, for Event 3 on 5

March 2022, wind speed averaged 15 km/h, peaking at 69 km/h, predominantly from the northeast at 67 degrees at Ward station, located at an elevation of 2597 m. In contrast, during Event 4 in the NorthStar Weather Station, the air temperature averaged  $-2^{\circ}\text{C}$ , ranging from  $-1^{\circ}\text{C}$  to  $-4^{\circ}\text{C}$ . Wind speeds were more pronounced, averaging 23 km/h and peaking at 70 km/h, mostly from the southwest (209 degrees). Lastly, on 9 March 2021, the westerly winds were notably strong, averaging 40 km/h, with gusts reaching 68 km/h at an elevation of 2597 m at Ward Station. These conditions coincided with cool temperatures averaging  $-8^{\circ}\text{C}$ , ranging between  $-7^{\circ}\text{C}$  and  $-8^{\circ}\text{C}$ . During the observed events, the conditions indicated consistently high humidity levels, with relative humidity ranging from 94% to 100%. The dew point and wet bulb temperatures fluctuated within the range of  $-11^{\circ}\text{C}$  to  $-2^{\circ}\text{C}$ , suggesting persistently cool and moist conditions conducive to seeding activities. Cloud seeding was conducted using ground-based generators, which typically target the lower portion of the cloud. The seeding duration varied depending on prevailing atmospheric conditions, with ground-based generator operations ranging from 2 to 12 h for the cases considered in this study.

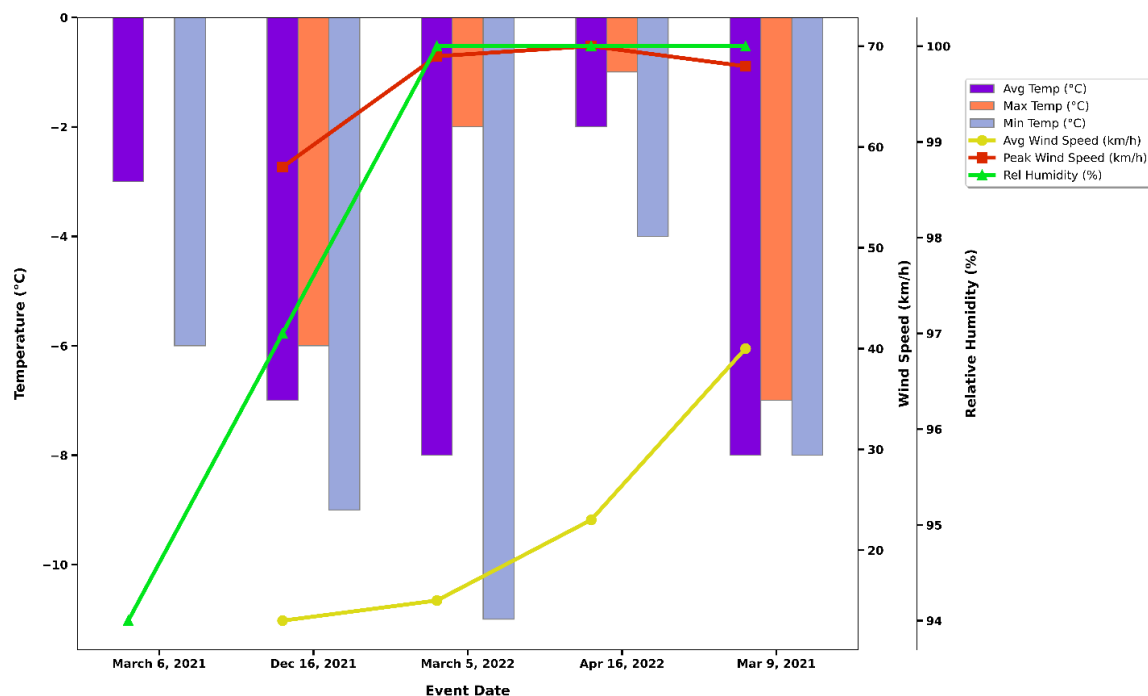


Figure 2.3. Combined atmospheric conditions on Event 1 (6 March 2021), Event 2 (16 December 2021), Event 3 (5 March 2022), Event 4 (16 April 2022), and Event 5 (9 March 2021), showing average temperature (°C), maximum temperature (°C), and minimum temperature (°C), average wind speed (km/h), peak wind speed (km/h), and relative humidity (%). Data sourced from weather stations closest to the ground-based generators, as provided by the Western Regional Climate Center.

#### 2.4.2. Model Results

By running the model under varied scenarios, the effects of cloud seeding on snow particle formation and dynamics can be effectively identified. In the absence of seeding, snow particles form naturally around atmospheric aerosols without the introduction of nucleating agents. Regarding Event 1 on 6 March 2021, Figure 2.4 (right panels) shows that the number concentration of particles decreases from 14 L<sup>-1</sup> at the cloud top to 2 L<sup>-1</sup> at the

bottom in natural conditions for the run with all three processes. This reduction is attributed to the growth of cloud particles from the top to the bottom of the cloud, where larger or heavier particles are more efficiently removed. The figure also highlights that aggregation plays a more significant role than riming in reducing the number of ice particles. Conversely, the snowfall rate, as depicted in Figure 2.5 (right panels), increases by approximately 0.2 mm/h when the three processes of riming, aggregation, and diffusion occur simultaneously. The vertical profile of IWC in Figure 2.6 (right panels) indicates an increase from the cloud top to the bottom (from 0.05 to 0.075 gr/cm<sup>3</sup>), driven by the phase transition from vapor to ice and the accumulation of cloud droplets on ice surfaces through riming. Although aggregation does not change the IWC, riming notably enhances it. Furthermore, Figure 2.7 (right panels) illustrates an increase in fall speed in scenarios that include all ice particle growth mechanisms, where the fall speed enhances from the cloud top to the base due to the increase in particle size and mass per area ratio.

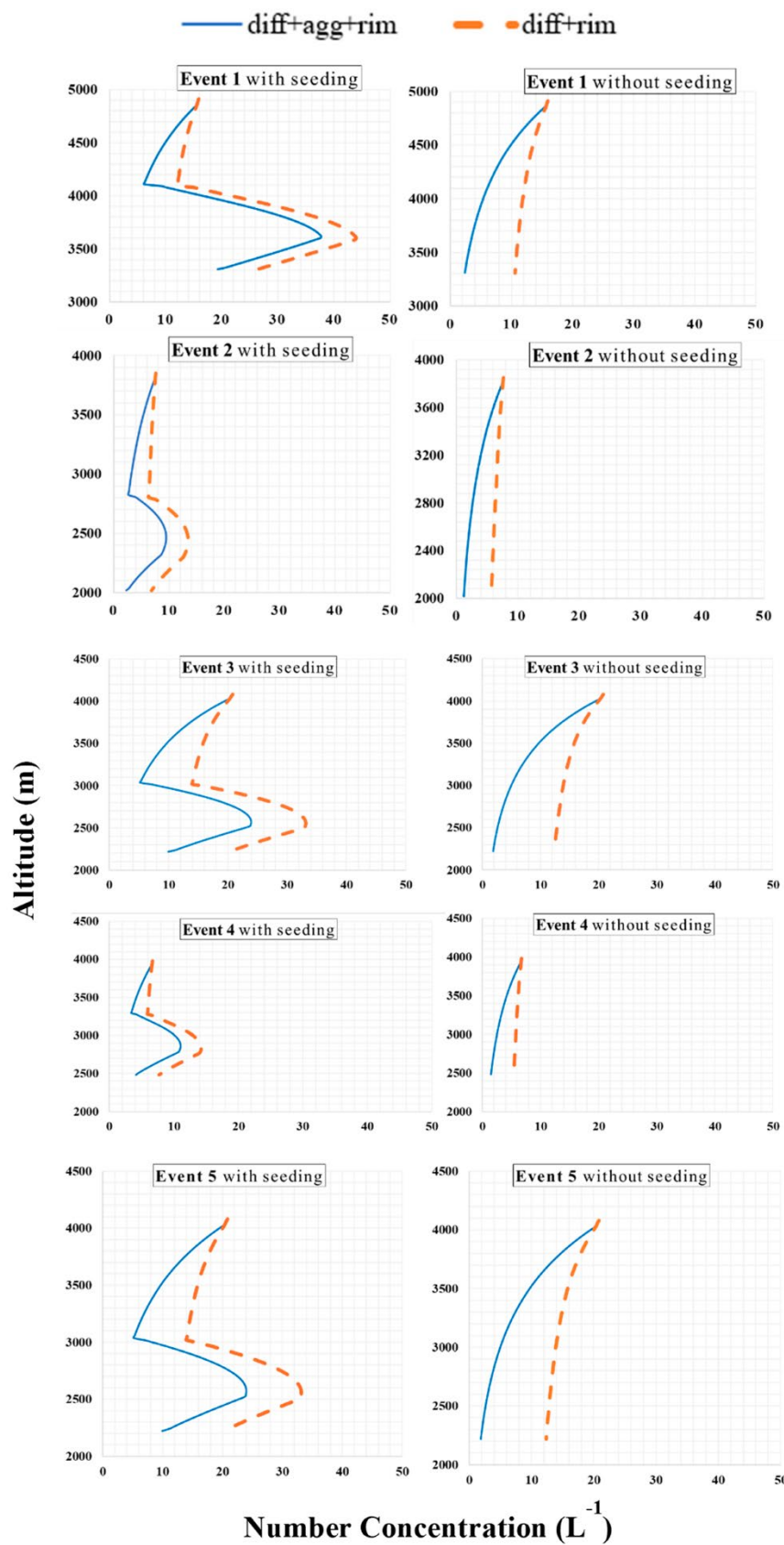


Figure 2.4. Comparison of the effects of seeding on Event 1 (6 March 2021), Event 2 (16 December 2021), Event 3 (5 March 2022), Event 4 (16 April 2022), and Event 5 (9 March 2021) across four scenarios incorporating diffusion, aggregation, and riming. The analysis includes changes in number concentration.

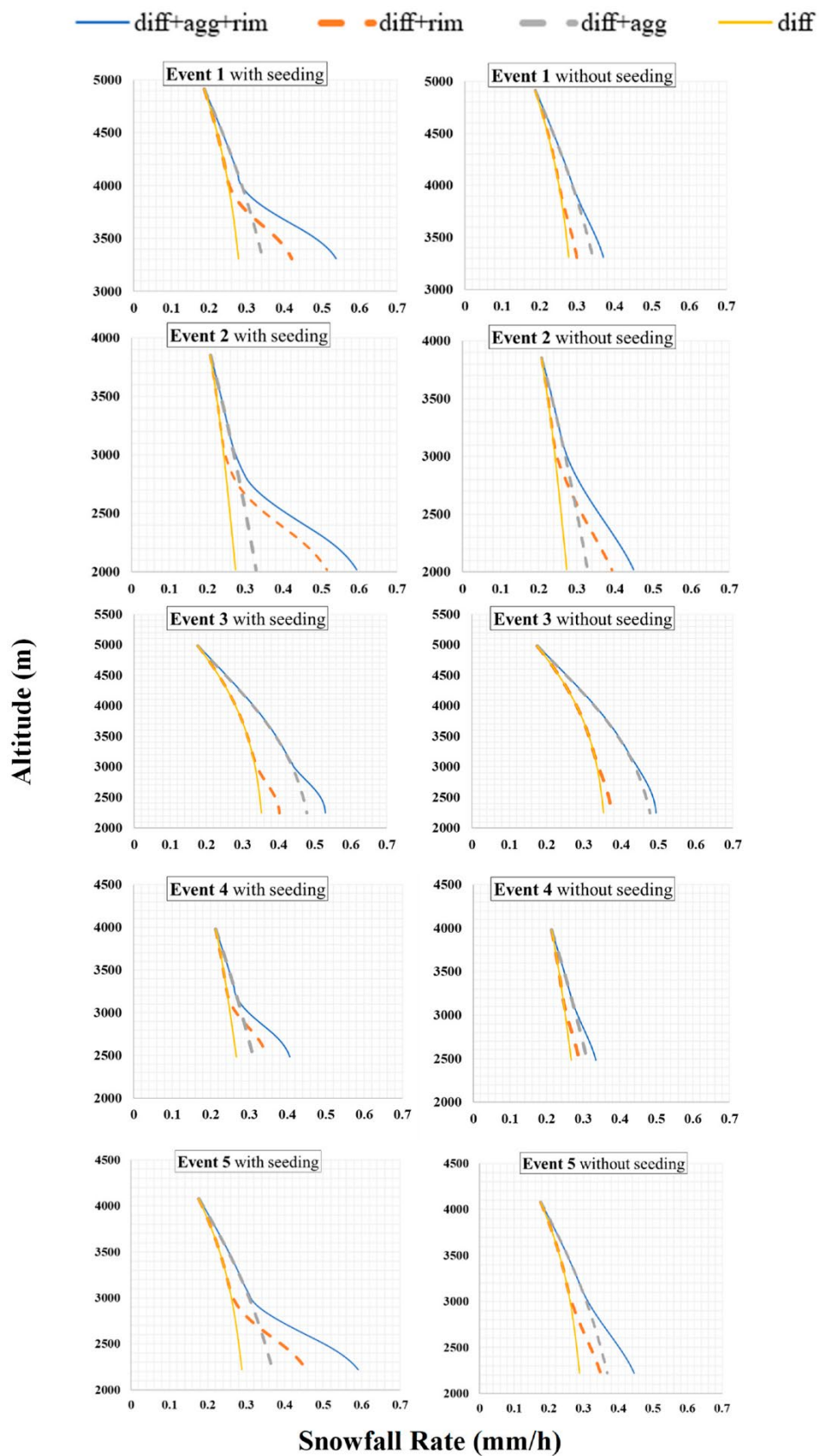


Figure 2.5. Comparison of the effects of seeding on Event 1 (6 March 2021), Event 2 (16 December 2021), Event 3 (5 March 2022), Event 4 (16 April 2022), and Event 5 (9 March 2021) across four scenarios incorporating diffusion, aggregation, and riming. The analysis includes changes in snowfall rate.

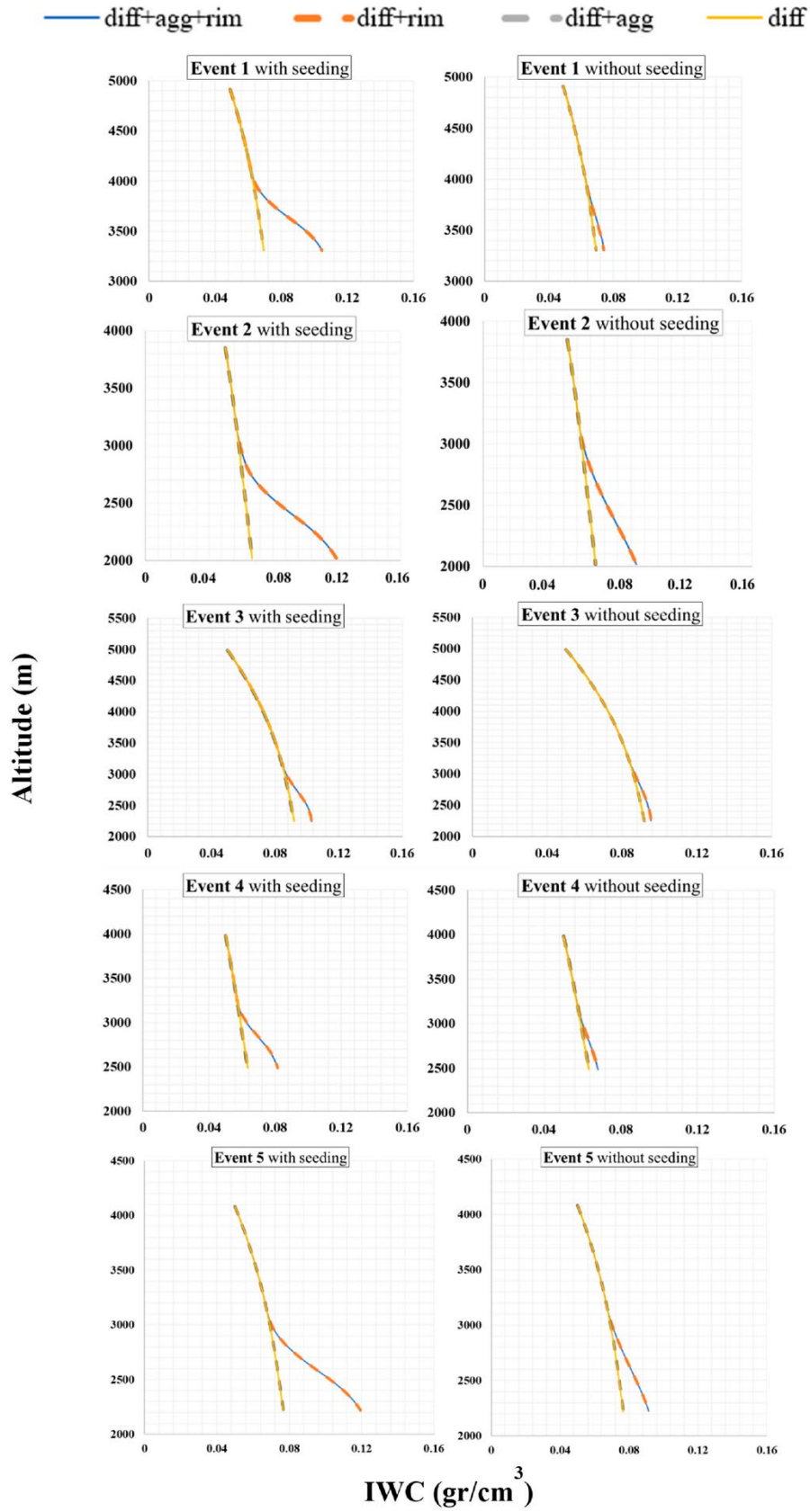


Figure 2.6. Comparison of the effects of seeding on Event 1 (6 March 2021), Event 2 (16 December 2021), Event 3 (5 March 2022), Event 4 (16 April 2022), and Event 5 (9 March 2021) across four scenarios incorporating diffusion, aggregation, and riming. The analysis includes changes in IWC.

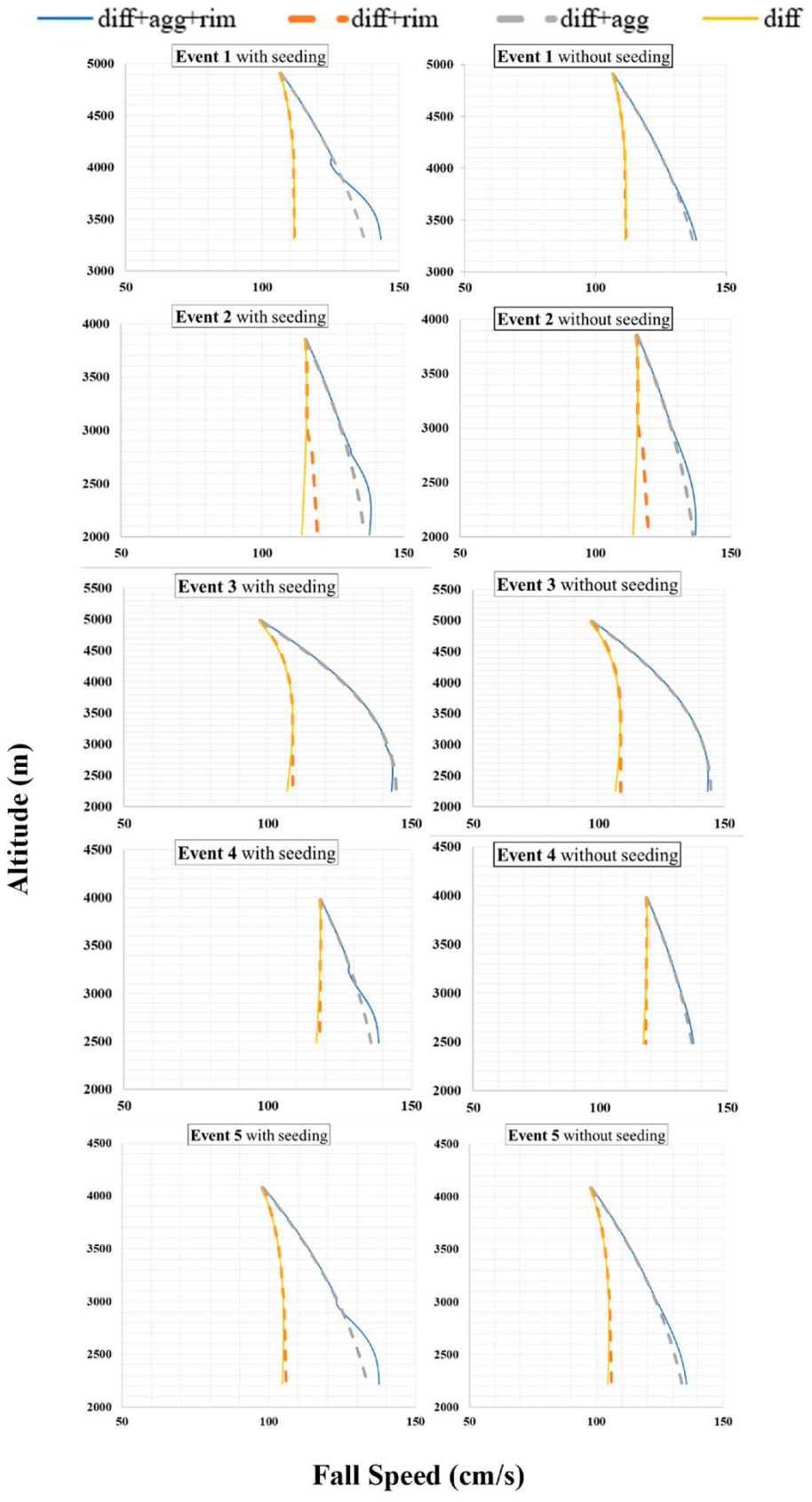


Figure 2.7. Comparison of the effects of seeding on Event 1 (6 March 2021), Event 2 (16 December 2021), Event 3 (5 March 2022), Event 4 (16 April 2022), and Event 5 (9 March 2021) across four scenarios incorporating diffusion, aggregation, and riming. The analysis includes changes in fall speed.

When seeding is active, the first significant effect observed is an increase in the number concentration of ice particles. This rise is primarily due to the AgI plume effect at the lower part of the cloud, where nucleation significantly enhances the number of ice particles (Figure 2.4; left panels). In Event 1, this concentration peaks at 38 particles per liter at an altitude of 3600 m. Seeding also notably enhances snowfall rates by forming a greater number of ice particles, especially evident in scenarios involving riming, as shown in Figure 2.5 (left panels). In this event, the snowfall rate increase was 0.17 mm/h, as the newly formed ice particles substantially boosted the IWC. This increase aligns with simulated transitions in other parameters, starting at altitudes around 4000 m. While aggregation produces larger but less dense snowflakes, riming significantly raises the ice mass through the accumulation of cloud droplets by ice particles. Additionally, cloud seeding considerably enhances the IWC, as depicted in Figure 2.6 (left panels). Comparative analysis of conditions with and without seeding shows that riming at the cloud base in Event 1 results in a 0.04 g/cm<sup>3</sup> increase in IWC. Furthermore, the introduction of nucleating agents alters the physical characteristics of snowflakes, including their size and shape, which affects their fall speed. Despite this, the overall impact on the mass-weighted fall speed is minimal because the nucleated ice particles are small.

In the natural conditions of Event 2, the cloud processes exhibit a typical, gradual transition in all measured parameters. The number concentration of ice particles for the run with the inclusion of diffusion, aggregation, and riming shows a consistent decrease with altitude, beginning to reduce from about eight particles per liter at 3800 m. The snowfall rate under unseeded conditions reaches the maximum of 0.45 mm/h at the cloud base. The IWC increases from top to bottom, reaching a maximum of 0.09 gr/cm<sup>3</sup> at the cloud base, reflective of higher ice content in comparison to Event 1, in natural cloud conditions. Similarly, the fall speed exhibits a maximum speed of about 135 cm/s at 2000 m.

Upon introducing seeding in Event 2, the cloud microphysics are significantly altered. The number concentration when diffusion, aggregation, and riming are included surges to 10 particles per liter at 2500 m, an increase that highlights the effectiveness of nucleating agents in stimulating ice particle formation. Likewise, the snowfall rate sees a considerable increase, reaching 0.6 mm/h at the cloud base, which is 0.15 mm/h higher than the unseeded condition. The IWC reaches a higher peak of 0.12 gr/cm<sup>3</sup> at 3000 m, a clear indication of a more efficient riming process facilitated by the seeding. Moreover, the fall speed of the particles increased in the scenario consisting of all mechanisms.

The model outcomes for Event 3 (on 5 March 2022) indicate that the number concentration of ice particles significantly reduces from 21 to about 12 particles per liter when riming and diffusion are present. In scenarios involving all three processes, the number concentration at the cloud base further drops to approximately two particles per liter, because aggregation causes ice particles to stick together. Moreover, the snowfall rate increases from 0.17 mm/h at an altitude of 5013 m to about 0.5 mm/h at 2249 m, reflecting

enhanced snow formation as particles descend. While the IWC shows minimal changes across all scenarios, it consistently enhances from the top to the bottom of the cloud. Also, the fall speed of particles rises from 95 cm/s at the cloud top to 110 cm/s at the cloud base in scenarios with aggregation and aggregation + diffusion, and to approximately 145 cm/s when aggregation is not present, highlighting the impact of particle growth mechanisms on fall velocity.

In contrast, the seeded condition of Event 3 results in the number concentration of ice particles reaching 24 particles per liter, when three processes are present. Although Event 3 features the lowest cloud top temperature and the highest altitude among all events, its number concentration remains lower than that simulated in Event 1. Furthermore, the snowfall rate grows at the 2500 m level, indicating enhanced precipitation efficiency due to seeding. A modest increase of about 0.01 g/cm<sup>3</sup> in IWC near the cloud base is observed, marking the lowest increase among all events. Additionally, the fall speed of particles shows a negligible change with seeding, suggesting that while nucleation enhances ice particle formation, it does not greatly affect the falling rate.

During Event 4 on 16 April 2022, the cloud's vertical depth was notably shallower compared to other observed events, with a measured depth of 1.51 km (Table 2.1). Under the unseeded condition, the number concentration decreased minimally, reaching approximately two particles per liter at the cloud bottom. The snowfall rate increased to 0.33 mm/h at the cloud base, located at an altitude of 2486 m. Additionally, there was only a minimal increase in IWC near the cloud base, indicating limited growth in ice mass under natural conditions. The overall trend in fall speed was a moderate increase with decreasing

height, from 120 cm/s at the cloud top to approximately 135 cm/s at the base. This trend suggests that as ice particles descended, their size and mass contributed to a greater fall speed.

Following the injection of cloud seeding, significant changes in cloud microphysics were observed in Event 4. The number concentration of ice particles increased to nine particles per liter at an altitude of 2800 m, 300 m above the cloud base. The snowfall rate began to rise from the middle of the cloud at approximately 2800 m and reached 0.41 mm/h at the cloud base, indicating a 0.05 mm/h increase due to seeding. The IWC also increased by about 0.01 gr/cm<sup>3</sup> after seeding, reflecting enhanced ice particle formation and growth. Furthermore, seeding led to an increase in the mass-weighted fall speed.

Regarding the last event on 9 March 2021, the number concentration of ice particles under natural atmospheric conditions decreased from 21 particles per liter at the cloud top to 2 particles per liter at the cloud base, including the three processes of diffusion, aggregation, and riming. Moreover, the snowfall rate increased, predominantly influenced by aggregation near the cloud top and by riming near the cloud bottom. The riming process is much stronger towards the cloud bottom because LWC values are higher in this part of the cloud. As a result of the collection of cloud droplets by ice particles, dense rimed particles form, and this enhances the overall IWC and, therefore, the snowfall rate in simulations with the inclusion of riming. Since riming is negligible near the cloud top, aggregation dominates, and, as a result, the snowfall rate is stronger in simulations including the aggregation process. Although aggregation did not alter the IWC, riming notably enhanced it. Specifically, the difference in IWC between scenarios including riming and those

without was approximately  $0.015 \text{ g/cm}^3$  at the cloud base. Furthermore, an increase in fall speed was shown in scenarios encompassing all ice particle growth mechanisms.

When seeding was active, the number concentration began to increase and reached a value of  $24 \text{ L}^{-1}$  at an altitude of around 3000 m due to the plume effect at the lower part of the cloud. Here, nucleation significantly enhanced the number of ice particles. Additionally, seeding led to a notable enhancement in snowfall rates by forming a greater number of snowflakes in scenarios involving riming. This enhancement amounted to approximately  $0.14 \text{ mm/h}$ . Moreover, in scenarios that included riming, the IWC increased by  $0.025 \text{ g/cm}^3$ .

In summary, SGMR findings indicate that riming has a significant impact due to the collection of cloud droplets by ice particles that leads to enhancing their mass and area while making a negligible change in their size. Notably, seeding increased the snowfall rate, with scenarios involving cloud seeding resulting in a snowfall rate on average 24% higher than those with no cloud seeding. The lowest enhancement in the snowfall rate was simulated in Event 3 (e.g., 6%), whereas the highest was in Event 1 (e.g., 37%). In general, the results provided a comprehensive understanding of how different microphysical processes and environmental conditions influence snowfall characteristics during cloud seeding.

The sensitivity of cloud seeding variables, such as temperature, liquid water content, and seeding agent concentration, is key to understanding and predicting the effectiveness of seeding [24]. Colder temperatures enhance nucleation, higher LWC supports riming and ice growth, and appropriate seeding agent concentrations promote efficient ice crystal

formation [57]. These variables interact in complex ways, and their combined effects determine the feasibility and success of cloud seeding operations. Moreover, atmospheric variable criteria, such as the presence of supercooled liquid water, cloud thickness, and appropriate wind conditions, play a crucial role in optimizing seeding outcomes and ensuring that cloud seeding is both feasible and effective [28].

To further understand the impact of different conditions on snow formation, this study involved running the model under four different scenarios, each representing a combination of processes, such as diffusion, aggregation, nucleation, and riming. The model was run for Event 1 with various number concentrations ranging from 100 to 1000  $\text{cm}^{-3}$  [53] to analyze the sensitivity of cloud microphysics to seeding agent concentration. The left panel in Figure 2.8 illustrates the evolution of the cloud particle number concentration from cloud top to bottom, while the right panel depicts the evolution of the snowfall rate for various AgI concentrations of 100  $\text{cm}^{-3}$ , 400  $\text{cm}^{-3}$ , 700  $\text{cm}^{-3}$ , and 1000  $\text{cm}^{-3}$  in the seeding plume (lowest 800 m within the cloud layer). The results indicate that higher agent concentrations lead to increased number concentrations and higher snowfall rates because more seeding agents enhance ice crystal formation, which accelerates snowflake growth and increases snowfall. As mentioned in Section 2.2, the AgI number concentration is assumed to be 700  $\text{cm}^{-3}$  throughout this study for the main simulations [53]. This concentration was chosen because it effectively promotes ice nucleation and enhances snowfall without excessive use of the seeding agent. The model was then executed with and without accounting for cloud seeding, an important part of our research. This method

was intended to assess the impact of cloud seeding on different parameters, including number concentration, IWC, mass-weighted terminal fall speed, and snowfall rate.

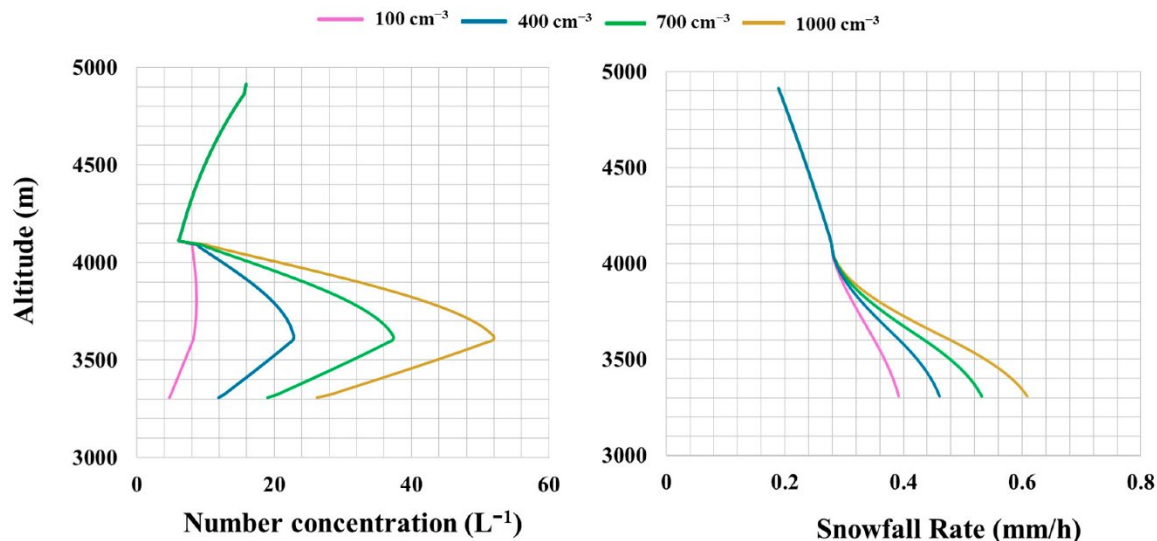


Figure 2.8. Sensitivity of cloud parameters (cloud particle number concentration and snowfall rate) to AgI number concentration (100, 400, 700, 1000  $\text{cm}^{-3}$ ) with active diffusion, aggregation, riming, and nucleation processes for Event 1.

## 2.5. Conclusions

This study presented significant advancements in understanding and modeling cloud seeding as the most common weather modification technique. Deeper insights into the microphysical processes of ice particle growth within seeded clouds were gained through the development and application of the SGMR model. The incorporation of riming and ice nucleation processes into the SGMR allowed for a more accurate simulation of the snowfall rate, particularly in the context of cloud seeding events in the Tahoe region. Previous studies often lacked a realistic integration of key microphysical processes and did not fully

explore their combined effects on precipitation. Additionally, there has been limited research on cloud seeding in the Tahoe area, making this study particularly valuable. This study addresses these gaps by enhancing the SGMR model to incorporate these processes, providing a more comprehensive understanding of cloud seeding's impact on snowfall. Analyzing five varied events in the region, this study found that cloud seeding significantly enhances snowfall rates, increasing them by an average of 24%, with the highest increase being 37%. Seeding also increases the number of ice particles, particularly at lower cloud levels, and enhances IWC through riming. While seeding slightly raises the fall speed of snow particles, the overall impact is minimal due to the small size of nucleated particles. The effectiveness of seeding varies across different events, with the most substantial effects observed in colder, thicker clouds. These enhancements highlighted the potential of cloud seeding to augment precipitation, which was crucial for water resource management, particularly in regions facing water scarcity.

Moreover, this study highlighted the complexities and challenges associated with cloud seeding. Variability in atmospheric conditions and the number concentration of seeding agents were critical factors influencing the outcomes of numerical simulations. These factors significantly affect cloud seeding effectiveness, as insufficient agent concentrations may not enhance precipitation. In addition, high-resolution observational datasets are required to initialize the models and reduce the uncertainty of simulations. While numerical models like the SGMR provide valuable insights, their findings can be validated with in situ measurements to ensure accuracy. The advancements in modeling and observational capabilities presented were essential for optimizing seeding strategies and maximizing

their effectiveness. However, there remains a critical need for more sophisticated mesoscale models that incorporate advanced aerosol schemes and accurately represent cloud and aerosol processes. Such models would allow for a more precise simulation of cloud seeding, accounting for the complex interactions between aerosols, cloud microphysics, and atmospheric dynamics. Incorporating these elements is particularly important in simulating the dispersion and activation of seeding agents like silver iodide, as well as in predicting the resulting changes in cloud properties and precipitation patterns. As climate change and population growth exacerbate water resource challenges, the role of cloud seeding in sustainable water management has become increasingly important. Continued research in weather modification technologies is crucial for harnessing their full potential to address global water needs.

## 2.6. References

1. Essien, M. Evaluation of Cloud Seeding Techniques for Precipitation Enhancement. *Glob. J. Clim. Stud.* 2023, 1, 53–64. [[Google Scholar](#)]
2. Li, D.; Zhao, C.; Yue, Z.; Liu, C.; Sun, Y.; Cohen, J.B. Response of cloud and precipitation properties to seeding at a supercooled cloud-top layer. *Earth Space Sci.* 2022, 9, e2021EA001791. [[Google Scholar](#)] [[CrossRef](#)]
3. Manton, M.J.; Warren, L.; Kenyon, S.L.; Peace, A.D.; Bilish, S.P.; Kemsley, K. A confirmatory snowfall enhancement project in the Snowy Mountains of Australia. Part I: Project design and response variables. *J. Appl. Meteor. Climatol.* 2011, 50, 1432–1447. [[Google Scholar](#)] [[CrossRef](#)]
4. Manton, M.J.; Peace, A.D.; Kemsley, K.; Kenyon, S.; Speirs, J.C.; Warren, L.; Denholm, J. Further analysis of a snowfall enhancement project in the Snowy Mountains of Australia. *Atmos. Res.* 2017, 193, 192–203. [[Google Scholar](#)] [[CrossRef](#)]
5. Rasmussen, R.M.; Tessendorf, S.A.; Xue, L.; Weeks, C.; Ikeda, K.; Landolt, S.; Breed, D.; Deshler, T.; Lawrence, B. Evaluation of the Wyoming Weather Modification Pilot Project (WWMPP) Using Two Approaches: Traditional

- Statistics and Ensemble Modeling. *J. Appl. Meteorol. Climatol.* 2018, 57, 2639–2660. [[Google Scholar](#)] [[CrossRef](#)]
6. Ritzman, J.M.; Deshler, T.; Ikeda, K.; Rasmussen, R. Estimating the Fraction of Winter Orographic Precipitation Produced under Conditions Meeting the Seeding Criteria for the Wyoming Weather Modification Pilot Project. *J. Appl. Meteorol. Climatol.* 2015, 54, 1202–1215. [[Google Scholar](#)] [[CrossRef](#)]
  7. Friedrich, K.; Ikeda, K.; Tessendorf, S.A.; French, J.R.; Rauber, R.M.; Geerts, B.; Xue, L.; Rasmussen, R.M.; Blestrud, D.R.; Kunkel, M.L.; et al. Quantifying snowfall from orographic cloud seeding. *Proc. Natl. Acad. Sci. USA* 2020, 117, 5190–5195. [[Google Scholar](#)] [[CrossRef](#)]
  8. Xue, L.L.; Chu, X.; Rasmussen, R.; Breed, D.; Boe, B.; Geerts, B. The dispersion of silver iodide particles from ground-based generators over complex terrain. Part II: WRF large-eddy simulations versus observations. *J. Appl. Meteorol. Climatol.* 2014, 53, 1342–1361. [[Google Scholar](#)] [[CrossRef](#)]
  9. French, J.R.; Friedrich, K.; Tessendorf, S.A.; Rauber, R.M.; Geerts, B.; Rasmussen, R.M.; Xue, L.; Kunkel, M.L.; Blestrud, D.R. Precipitation formation from orographic cloud seeding. *Proc. Natl. Acad. Sci. USA* 2018, 115, 1168–1173. [[Google Scholar](#)] [[CrossRef](#)]
  10. Zhao, C.; Yang, Y.; Fan, H.; Huang, J.; Fu, Y.; Zhang, X.; Kang, S.; Cong, Z.; Letu, H.; Menenti, M. Aerosol characteristics and impacts on weather and climate over Tibetan Plateau. *Natl. Sci. Rev.* 2020, 7, 492–495. [[Google Scholar](#)] [[CrossRef](#)]
  11. U.S. Census Bureau. 2010 Census: Apportionment Data. U.S. Census Bureau. 2010. Available online: <https://www.census.gov/data/tables/2010/dec/apportionment-data-text.html> (accessed on 26 April 2021).
  12. Rauber, R.M.; Geerts, B.; Xue, L.; French, J.; Friedrich, K.; Rasmussen, R.M.; Tessendorf, S.A.; Blestrud, D.R.; Kunkel, M.L.; Parkinson, S. Wintertime orographic cloud seeding—A review. *J. Appl. Meteorol. Climatol.* 2019, 58, 2117–2140. [[Google Scholar](#)] [[CrossRef](#)]
  13. Rasmussen, R.; Liu, C.; Ikeda, K.; Gochis, D.; Yates, D.; Chen, F.; Tewari, M.; Barlage, M.; Dudhia, J.; Yu, W.; et al. High-Resolution Coupled Climate Runoff Simulations of Seasonal Snowfall over Colorado: A Process Study of Current and Warmer Climate. *J. Clim.* 2011, 24, 3015–3048. [[Google Scholar](#)] [[CrossRef](#)]
  14. Segal, Y.; Khain, A.; Pinsky, M.; Rosenfeld, D. Effects of hygroscopic seeding on raindrop formation as seen from simulations using a 2000-bin spectral cloud parcel model. *Atmos. Res.* 2004, 71, 3–34. [[Google Scholar](#)] [[CrossRef](#)]

15. Flossmann, A.I.; Manton, M.; Abshaev, A.; Brientjes, R.; Murakami, M.; Prabhakaran, T.; Yao, Z. Review of advances in precipitation enhancement research. *Bull. Am. Meteorol. Soc.* 2019, 100, 1465–1480. [[Google Scholar](#)] [[CrossRef](#)]
16. Laaksonen, A.; Malila, J. *Nucleation of Water: From Fundamental Science to Atmospheric and Additional Applications*; Elsevier: Amsterdam, The Netherlands, 2021. [[Google Scholar](#)]
17. Woodley, W.L.; Rosenfeld, D.; Silverman, B.A. Results of on-top glaciogenic cloud seeding in Thailand. Part I: The demonstration experiment. *J. Appl. Meteorol. Climatol.* 2003, 42, 920–938. [[Google Scholar](#)] [[CrossRef](#)]
18. Maryadi, A.; Tomine, K.; Nishiyama, K. Some aspects of a numerical glaciogenic artificial cloud seeding experiment using liquid carbon dioxide over Kupang, Indonesia. *J. Agric. Meteorol.* 2015, 71, 1–14. [[Google Scholar](#)] [[CrossRef](#)]
19. Tessendorf, S.A.; French, J.R.; Friedrich, K.; Geerts, B.; Rauber, R.M.; Rasmussen, R.M.; Xue, L.; Ikeda, K.; Blestrud, D.R.; Kunkel, M.L.; et al. A transformational approach to winter orographic weather modification research: The SNOWIE Project. *Bull. Am. Meteorol. Soc.* 2019, 100, 71–92. [[Google Scholar](#)] [[CrossRef](#)]
20. Geerts, B.; Miao, Q.; Yang, Y.; Rasmussen, R.; Breed, D. An airborne profiling radar study of the impact of glaciogenic cloud seeding on snowfall from winter orographic clouds. *J. Atmos. Sci.* 2010, 67, 3286–3302. [[Google Scholar](#)] [[CrossRef](#)]
21. Breed, D.; Rasmussen, R.; Weeks, C.; Boe, B.; Deshler, T. Evaluating winter orographic cloud seeding: Design of the Wyoming Weather Modification Pilot Project (WWMPP). *J. Appl. Meteorol. Climatol.* 2014, 53, 282–299. [[Google Scholar](#)] [[CrossRef](#)]
22. Abshaev, M.T.; Abshaev, A.M.; Sulakvelidze, G.K.; Burtsev, I.I.; Malkarova, A.M.; Nesmeyanov, P.A. Development of rocket and artillery technology for hail suppression. *Achiev. Weather. Modif.* 2006, 109–127. [[Google Scholar](#)]
23. Brientjes, R.T.; Clark, T.L.; Hall, W.D. The dispersion of tracer plumes in mountainous regions in central Arizona: Comparisons between observations and modeling results. *J. Appl. Meteorol. Climatol.* 1995, 34, 971–988. [[Google Scholar](#)] [[CrossRef](#)]
24. Xue, L.; Hashimoto, A.; Murakami, M.; Rasmussen, R.; Tessendorf, S.A.; Breed, D.; Parkinson, S.; Holbrook, P.; Blestrud, D. Implementation of a silver iodide cloud-seeding parameterization in WRF. Part I: Model description and idealized 2D sensitivity tests. *J. Appl. Meteorol. Climatol.* 2013, 52, 1433–1457. [[Google Scholar](#)] [[CrossRef](#)]

25. Dessens, J.; Sánchez, J.L.; Berthet, C.; Hermida, L.; Merino, A. Hail prevention by ground-based silver iodide generators: Results of historical and modern field projects. *Atmos. Res.* 2016, 170, 98–111. [[Google Scholar](#)] [[CrossRef](#)]
26. Haupt, S.E.; Rauber, R.M.; Carmichael, B.; Knievel, J.C.; Cogan, J.L. 100 years of progress in applied meteorology. Part I: Basic applications. *Meteorol. Monogr.* 2018, 59, 22.1–22.33. [[Google Scholar](#)] [[CrossRef](#)]
27. Gabriel, K.R. Ratio statistics for randomized experiments in precipitation stimulation. *J. Appl. Meteor.* 1999, 38, 290–301. [[Google Scholar](#)] [[CrossRef](#)]
28. Flossmann, A.I.; Manton, M.; Abshaev, A.; Brientjes, R.; Murakami, M.; Prabhakaran, T.; Yao, Z. Peer Review Report on Global Precipitation Enhancement Activities (Research Report); World Meteorological Organization: Geneva, Switzerland, 2018; Available online: <https://hal.uca.fr/hal-01917801> (accessed on 20 March 2023).
29. Wang, J.; Yue, Z.; Rosenfeld, D.; Zhang, L.; Zhu, Y.; Dai, J.; Yu, X.; Li, J. The Evolution of an AgI Cloud-Seeding Track in Central China as Seen by a Combination of Radar, Satellite, and Disdrometer Observations. *J. Geophys. Res. Atmos.* 2021, 126, e2020JD033914. [[Google Scholar](#)] [[CrossRef](#)]
30. Xue, L.; Edwards, R.; Huggins, A.; Lou, X.; Rasmussen, R.; Tessendorf, S.; Holbrook, P.; Blestrud, D.; Kunkel, M.; Glenn, B.; et al. WRF Large-eddy Simulations of chemical tracer deposition and seeding effect over complex terrain from ground-and aircraft-based AgI generators. *Atmos. Res.* 2017, 190, 89–103. [[Google Scholar](#)] [[CrossRef](#)]
31. Xue, L.; Chu, X.; Rasmussen, R.; Breed, D.; Geerts, B. A Case Study of Radar Observations and WRF LES Simulations of the Impact of Ground-Based Glaciogenic Seeding on Orographic Clouds and Precipitation. Part II: AgI Dispersion and Seeding Signals Simulated by WRF. *J. Appl. Meteorol. Climatol.* 2016, 55, 445–464. [[Google Scholar](#)] [[CrossRef](#)]
32. Chu, X.; Geerts, B.; Xue, L.; Pokharel, B. A Case Study of Cloud Radar Observations and Large-Eddy Simulations of a Shallow Stratiform Orographic Cloud, and the Impact of Glaciogenic Seeding. *J. Appl. Meteorol. Climatol.* 2017, 56, 1285–1304. [[Google Scholar](#)] [[CrossRef](#)]
33. Jing, X.; Geerts, B.; Wang, Y.; Liu, C. Evaluating Seasonal Orographic Precipitation in the Interior Western United States Using Gauge Data, Gridded Precipitation Estimates, and a Regional Climate Simulation. *J. Hydrometeorol.* 2017, 18, 2541–2558. [[Google Scholar](#)] [[CrossRef](#)]
34. Liu, C.; Ikeda, K.; Rasmussen, R.; Barlage, M.; Newman, A.J.; Prein, A.F.; Chen, F.; Chen, L.; Clark, M.; Dai, A.; et al. Continental-scale convection-permitting

- modeling of the current and future climate of North America. *Clim. Dyn.* 2017, 49, 71–95. [[Google Scholar](#)] [[CrossRef](#)]
35. Levy, G.; Cotton, W.R. A numerical investigation of mechanisms linking glaciation of the ice-phase to the boundary layer. *J. Clim. Appl. Meteorol.* 1984, 23, 1505–1519. [[Google Scholar](#)] [[CrossRef](#)]
  36. Farley, R.D.; Nguyen, P.; Orville, H.D. Numerical simulation of cloud seeding using a three-dimensional cloud model. *J. Weather Modif.* 1994, 26, 113–124. [[Google Scholar](#)]
  37. Guo, X.; Zheng, G.; Jin, D. A numerical comparison study of cloud seeding by silver iodide and liquid carbon dioxide. *Atmos. Res.* 2006, 79, 183–226. [[Google Scholar](#)] [[CrossRef](#)]
  38. Guo, X.; Fu, D.; Zheng, G. Modeling study on optimal convective cloud seeding in rain augmentation. *Asia-Pac. J. Atmos. Sci.* 2007, 43, 273–284. [[Google Scholar](#)]
  39. Javanmard, S.; Pirhayati, M.K. A Numerical Study of the Role of Cold Convective Cloud Parameterization in Precipitation Pattern at Ground Surface. *J. Geogr. Geol.* 2012, 4, 269. [[Google Scholar](#)] [[CrossRef](#)]
  40. Passarelli, R.E., Jr. Approximate analytical model of the vapor deposition and aggregation growth of snowflakes. *J. Atmos. Sci.* 1978, 35, 118–124. [[Google Scholar](#)] [[CrossRef](#)]
  41. Mitchell, D.L.; Huggins, A.; Grubisic, V. A new snow growth model with application to radar precipitation estimates. *Atmos. Res.* 2006, 82, 2–18. [[Google Scholar](#)] [[CrossRef](#)]
  42. Erfani, E. A Mechanistic Understanding of North American Monsoon and Microphysical Properties of Ice Particles; University of Nevada, Reno: Reno, NV, USA, 2016. [[Google Scholar](#)]
  43. Rienecker, M.M.; Suarez, M.J.; Gelaro, R.; Todling, R.; Bacmeister, J.; Liu, E.; Bosilovich, M.G.; Schubert, S.D.; Takacs, L.; Kim, G.-K.; et al. MERRA: NASA's modern-era retrospective analysis for research and applications. *J. Clim.* 2011, 24, 3624–3648. [[Google Scholar](#)] [[CrossRef](#)]
  44. Greenwald, T.J.; Pierce, R.B.; Schaack, T.K.; Otkin, J.A.; Rogal, M.; Bah, K.; Lenzen, A.J.; Nelson, J.P.; Li, J.; Huang, H.L. Real-time simulation of the GOES-R ABI for user readiness and product evaluation. *Bull. Am. Meteorol. Soc.* 2016, 97, 245–261. [[Google Scholar](#)] [[CrossRef](#)]
  45. Gelaro, R.; McCarty, W.; Suárez, M.J.; Todling, R.; Molod, A.; Takacs, L.; Randles, C.A.; Darmenov, A.; Bosilovich, M.G.; Reichle, R.; et al. The modern-era

- retrospective analysis for research and applications, version 2 (MERRA-2). *J. Clim.* 2017, 30, 5419–5454. [[Google Scholar](#)] [[CrossRef](#)] [[PubMed](#)]
46. Doelling, D.R.; Sun, M.; Nordeen, M.L.; Haney, C.O.; Keyes, D.F.; Mlynchak, P.E. Advances in geostationary-derived longwave fluxes for the CERES synoptic (SYN1deg) product. *J. Atmos. Ocean. Technol.* 2016, 33, 503–521. [[Google Scholar](#)] [[CrossRef](#)]
  47. Wielicki, B.A.; Barkstrom, B.R.; Harrison, E.F.; Lee III, R.B.; Smith, G.L.; Cooper, J.E. Clouds and the Earth's Radiant Energy System (CERES): An earth observing system experiment. *Bull. Am. Meteorol. Soc.* 1996, 77, 853–868. [[Google Scholar](#)] [[CrossRef](#)]
  48. Loeb, N.G.; Su, W.; Doelling, D.R.; Wong, T.; Minnis, P.; Thomas, S.; Miller, W.F. Earth's top-of-atmosphere radiation budget. Reference Module in Earth Systems and Environmental Sciences. *Compr. Remote Sens.* 2018, 5, 67–84. [[Google Scholar](#)] [[CrossRef](#)]
  49. Payra, S.; Sharma, A.; Verma, S. Application of remote sensing to study forest fires. In *Atmospheric Remote Sensing*; Elsevier: Amsterdam, The Netherlands, 2023; pp. 239–260. [[Google Scholar](#)]
  50. Justice, C.; Townshend, J.; Vermote, E.; Masuoka, E.; Wolfe, R.; Saleous, N.; Roy, D.; Morisette, J. An overview of MODIS Land data processing and product status. *Remote Sens. Environ.* 2002, 83, 3–15. [[Google Scholar](#)] [[CrossRef](#)]
  51. Erfani, E.; Mitchell, D.L. Growth of ice particle mass and projected area during riming. *Atmos. Chem. Phys.* 2017, 17, 1241–1257. [[Google Scholar](#)] [[CrossRef](#)]
  52. Liu, X.; Penner, J.E.; Ghan, S.J.; Wang, M. Inclusion of ice microphysics in the NCAR Community Atmospheric Model version 3 (CAM3). *J. Clim.* 2007, 20, 4526–4547. [[Google Scholar](#)] [[CrossRef](#)]
  53. Marcolli, C.; Nagare, B.; Welti, A.; Lohmann, U. Ice nucleation efficiency of AgI: Review and new insights. *Atmos. Chem. Phys.* 2016, 16, 8915–8937. [[Google Scholar](#)] [[CrossRef](#)]
  54. Achtert, P.; O'Connor, E.J.; Brooks, I.M.; Sotiropoulou, G.; Shupe, M.D.; Pospichal, B.; Brooks, B.J.; Tjernström, M. Properties of Arctic liquid and mixed-phase clouds from shipborne Cloudnet observations during ACSE 2014. *Atmos. Chem. Phys.* 2020, 20, 14983–15002. [[Google Scholar](#)] [[CrossRef](#)]
  55. Järvinen, E.; Nehlert, F.; Xu, G.; Waitz, F.; Mioche, G.; Dupuy, R.; Jourdan, O.; Schnaiter, M. Vertical distribution of ice optical and microphysical properties in Arctic low-level mixed-phase clouds during ACLOUD. *Atmos. Chem. Phys. Discuss.* 2023, 2023, 1–30. [[Google Scholar](#)]

56. Western Regional Climate Center. Available online: <https://wrcc.dri.edu/> (accessed on 2 April 2023).
57. Morrison, B.J. A Characterization of Dry Ice as a Glaciogenic Seeding Agent. Atmospheric Science Paper No. 441; Department of Atmospheric Science, Colorado State University: Fort Collins, CO, USA, 1989. [[Google Scholar](#)]

## **Chapter 3**

# **Assessing Orographic Cloud Seeding Impacts Through Integration of Remote Sensing from Multispectral Satellite and Radar Data and In Situ Observations in the Western United States**

This chapter is an adapted version of the following publication:

Mehdizadeh, G., Hosseinpour, F., & McDonough, F. (2025). Assessing Orographic Cloud Seeding Impacts Through Integration of Remote Sensing from Multispectral Satellite and Radar Data and In Situ Observations in the Western United States.

### 3.1. Abstract

Cloud seeding is a targeted weather modification strategy aimed at enhancing precipitation, particularly in regions facing water scarcity. This study evaluates the impacts of wintertime cloud seeding events in the western United States, focusing on three key regions: the Lake Tahoe Area, the Santa Rosa Range, and the Ruby Mountains using an in-targeted remote sensing approach. Ground-based AgI generators were deployed to initiate seeding, and the atmospheric responses were assessed using multispectral observations from the Advanced Baseline Imager (ABI) aboard the GOES-R series satellites and regional radar reflectivity mosaics derived from NEXRAD data. Satellite-derived cloud microphysical properties, including cloud-top brightness temperatures, optical thickness, and phase indicators, were analyzed in conjunction with radar reflectivity to evaluate microphysical changes associated with seeding. The analysis revealed significant regional variability: Tahoe events consistently exhibited strong seeding signatures, such as droplet-to-ice phase transitions, cloud-top cooling, and thickened cloud structures, often followed by increased radar reflectivity. These outcomes were linked to favorable atmospheric conditions including colder temperatures, elevated mid-to-upper tropospheric moisture, and sufficient supercooled liquid water. In contrast, events in Santa Rosa Range generally showed weaker responses due to warmer, drier conditions and limited cloud development, while the Ruby Mountains presented mixed outcomes. A key contribution of this study is the development of a reproducible satellite–radar integration framework that improves the detection and interpretation of cloud seeding impacts. This combined approach allows for a more comprehensive assessment of seeding outcomes, capturing the progression from initial cloud-phase transitions to potential hydrometeor development. The results highlight the

importance of aligning seeding strategies with local atmospheric conditions and demonstrate the practical value of satellite-based tools for evaluating seeding effectiveness, particularly in data-sparse regions. Overall, this work contributes to advancing both the scientific insight and operational practices of weather modification through remote sensing.

### 3.2. Introduction

Cloud seeding is a weather modification technique designed to enhance precipitation by introducing aerosols such as silver iodide (AgI) into clouds [1,2,3,4]. These aerosols serve as nuclei around which water droplets can form, or initiate ice nucleation, facilitating the coalescence process and increasing the likelihood of precipitation. AgI is widely used due to its crystal structure, which closely resembles that of ice, promoting ice formation in supercooled clouds. Cloud seeding is often applied in regions experiencing drought conditions or to enhance snowfall in mountainous areas [3,5]. While its effectiveness depends on various factors, including cloud type and environmental conditions, cloud seeding has been utilized as a tool to manage water resources and mitigate the impacts of drought [6,7]. Despite ongoing debates about its efficacy in natural variability, operational programs continue to expand with support from both governmental and regional stakeholders.

Cloud-seeding methodologies are commonly classified as glaciogenic or hygroscopic [8]. Glaciogenic seeding introduces efficient ice-nucleating particles, most often AgI or, in some programs, calcium chloride, into mixed-phase clouds to stimulate the Bergeron–Findeisen process, enlarge ice crystals and hasten their descent as snow or rain [9,10].

Hygroscopic seeding, by contrast, releases micron-scale salt aerosols into warm convective clouds, broadening the droplet spectrum, intensifying collision–coalescence, and ultimately increasing rainfall at the surface [11]. Current operations integrate high-resolution numerical weather prediction, radar nowcasting, and in-situ cloud-physics measurements to optimize launch timing from aircraft, ground generators, rockets, or autonomous uncrewed aerial platforms [12,13]. This systems-based approach underscores the interdisciplinary character of modern weather-modification research and provides the physical baseline against which remote sensing-based evaluations of post-seeding cloud responses can be interpreted.

At present, more than forty sustained programs employ cloud seeding for diverse objectives that include winter orographic snow-pack enhancement in the western United States, warm-cloud rainfall augmentation across the Arabian Peninsula and Southeast Asia, hail-suppression initiatives in parts of Europe and Canada, and fog-dispersion at major transportation hubs (14,15,16]. Cost–benefit assessments suggest favorable economic returns when precipitation increases are integrated over reservoir inflows or reduced hail damage to agriculture and infrastructure [17]. Long-term environmental monitoring further shows that background concentrations of AgI or other seeding agents remain several orders of magnitude below established ecotoxicological thresholds, though continued surveillance is recommended as operational scales expand [18]. These cumulative operational findings furnish critical context for evaluating seeding outcomes through satellite observations and help frame the practical value of refining detection algorithms for seeding-induced cloud and precipitation modifications. As global water demands in-

crease and climate variability intensifies, scalable and verifiable enhancement strategies are gaining renewed attention.

Understanding the atmospheric processes that influence cloud formation and precipitation is critical for improving weather modification techniques such as cloud seeding [3]. As global climate patterns shift and water scarcity issues intensify, the need for reliable and efficient cloud seeding methods has become more pressing [19]. Ensuring access to clean and dependable water resources also demands integrated environmental monitoring and modeling strategies [20,21,22]. There have been many studies focusing on the environmental impacts of human interventions and climate-related changes [23,24,25]. Satellite remote sensing provides a powerful approach for monitoring cloud seeding activities and assessing their impacts on cloud microphysics, precipitation, and aero-sol-cloud interactions, enhancing our understanding through advanced retrieval methodologies [13,26,27,28,29]. Moreover, the integration of geostationary satellite data with ground-based and airborne observations is helping to identify microphysical signatures of seeded clouds in near real time, contributing to improved targeting and post-event validation.

### 3.2.1. Remote Sensing in Cloud Seeding

#### 3.2.1.1. Satellite Observations and Technological Developments

The first satellite-based observation of glaciogenic cloud-seeding signatures was recorded in 2005, when the Advanced Very High-Resolution Radiometer (AVHRR)[30] satellite imagery captured a distinct cloud track resulting from the seeding of a thick super-cooled cloud layer over central China, with cloud microphysical property retrievals revealing

glaciation and cloud-top sinking, which were further validated by simulations of seeding material dispersion [31]. Yu et al. (2005) utilized NOAA-14 satellite imagery alongside numerical modeling to validate the effects of cloud seeding over Shaanxi, China, where a distinct cloud formation appeared shortly after seeding and corresponded with the dispersion of silver iodide; their simulations closely aligned with the satellite observations, confirming the seeding's impact on cloud development and duration [32]. Wang et al. (2021) [33] used the Moderate Resolution Imaging Spectroradiometer (MODIS) [34] and FengYun-3C [35] polar-orbiting meteorological satellite, CINRAD/CB radar (C-band component of the China New Generation Doppler Weather Radar) [36], and PARSIVEL disdrometer (Particle Size Velocity) [37,38] data to track AgI cloud seeding in central China. Satellite imagery captured a glaciated seeding track shortly after treatment, confirming ice formation and cloud-top collapse, and subsequent radar and disdrometer measurements validated the track's expansion and increased precipitation, thereby supporting the effectiveness of cloud seeding. Utilizing MODIS-derived cloud characteristics, Morrison et al. (2013) identified areas with supercooled liquid water, which are considered optimal targets for glaciogenic cloud seeding [39]. Observations from the Himawari-8 satellite [40], a geostationary satellite operated by Japan, confirmed these effects by detecting a rise in cloud brightness temperature after seeding, attributed to ice particle fallout and the subsequent collapse of the cloud top within the seeding track. These studies high-light the role of satellite remote sensing in monitoring and evaluating cloud seeding im-pacts, providing valuable insights for weather modification research.

#### 3.2.1.2. Advancements in Geostationary Satellite Capabilities

The Geostationary Operational Environmental Satellites (GOES) [41] have played a key role in advancing meteorological observations and forecasts since their deployment. These satellites provide continuous, high-temporal-resolution monitoring of atmospheric conditions, including cloud development, convection, cloud-top properties essential for weather analysis, and cloud seeding assessments. The GOES-R series introduced significant technological advancements, enhancing data quality and expanding application capabilities for atmospheric monitoring [42]. These improvements in spatial, temporal, and spectral resolution, along with enhanced radiometric accuracy, have particularly benefited cloud microphysics studies and atmospheric analyses relevant to cloud seeding. The ABI serves as the primary imaging device on NOAA's GOES-R Series satellites, capturing data on various surface and atmospheric features such as clouds, moisture levels, and smoke [43,44,45]. The ABI enhances the monitoring of these features with improved spectral bands, enabling more precise observations of atmospheric conditions and surface changes. This capability is particularly valuable for tracking weather events, wildfire activity, and cloud characteristics relevant to cloud seeding applications [46]. ABI operates with 16 spectral bands, comprising two visible, four near-infrared (NIR), and ten infrared (IR) channels [44,47,48,49,50]. Furthermore, ABI's data assimilation into numerical weather prediction models has led to improved forecast accuracy. The comprehensive observations of atmospheric parameters enhance model initialization, resulting in better predictions of weather patterns and climate phenomena [51].

This paper aims to investigate the application of satellite remote sensing to gain deeper insight into the impacts of cloud seeding. Real-time monitoring of cloud properties offers valuable insights into the dynamics of cloud seeding, allowing for more accurate

assessments and improved weather modification strategies. We hypothesize that spectral analysis from satellite remote sensing can detect seeding-induced changes, thereby refining current methodologies and enhancing effective cloud seeding operations. In this study, we compare different GOES satellite bands across various cloud seeding events to identify key post-seeding atmospheric and cloud features. By analyzing spectral signatures and cloud microphysical properties, we aim to develop methodologies for detecting seeding-induced modifications using satellite observations. Section 2 outlines the methodology, including satellite bands and their characteristics. Section 3 presents case studies of cloud seeding events. Section 4 discusses the implications of these findings for improving cloud seeding assessments, followed by conclusions and future research directions in Section 5.

### 3.3. Data and Methodology

#### 3.3.1. Case study: Wintertime Cloud Seeding in Targeted Western U.S. Regions

Wintertime cloud seeding programs in the western United States have been ongoing since the early 1960s, with initial studies focused on the Lake Tahoe region [52,53]. These operations typically utilize ground-based generators that burn an AgI solution, a method in use since the 1980s. Estimates of seasonal seeding effectiveness indicate snowfall increases ranging from 4% to 10% have been achieved [52]. Through science-based techniques, these programs aim to enhance snowpack and increase runoff in mountainous areas. These efforts are aimed to enhance precipitation formation efficiency during winter storms, while maintaining environmentally responsible practices that support sustainable water resources for both ecosystems and communities.

The weather sensors installed at ground-based cloud seeding generators include instruments capable of measuring meteorological conditions at high temporal resolution for operational monitoring. Wind speed and direction are measured using anemometers, which provide a wind speed resolution of approximately 0.098 m/s per Hz of pulse output and a directional resolution of 0.5°, with accuracies of  $\pm 0.3$  m/s and  $\pm 3^\circ$ , respectively. Temperature and relative humidity sensors offer resolutions of 0.1 °C and 0.1 % RH, with accuracies of  $\pm 0.6$  °C and  $\pm 3$  % RH. Precipitation is recorded using all-weather weighing gauges, which detect incremental changes as small as 0.05–0.1 mm depending on capacity and sensor configuration. Meteorological parameters are typically logged at 15-minute intervals, although the system supports sub-minute sampling depending on deployment settings.

Cloud seeding operations examined in this study focus on key areas, such as the Lake Tahoe Basin, the Ruby Mountains, and the Santa Rosa Range in Nevada (Figure 3.1). Seeding operations in the Ruby Mountains were conducted on January 2, 3, and 13, 2024. In the Santa Rosa Range, key seeding dates included January 2, 3, and 13, 2024, as well as March 1, 2024. The Lake Tahoe Basin experienced observed seeding events on February 1 and 20, 2024, November 11, 2024, and February 16, 2025. Ground-based generators are strategically installed at elevations ranging from 1,500 to 2,900 meters in Tahoe, 1,829 to 2,010 meters in the Rubies, and 1,460 to 1,493 meters in Santa Rosa. These placements facilitate the effective dispersal of seeding materials into cloud systems to stimulate snowfall over key watersheds. Operations are primarily carried out during winter months, from November through May, and are implemented in collaboration with local, and federal partners.

To evaluate the effects of cloud seeding operations, satellite remote sensing data were analyzed to monitor cloud properties and atmospheric changes. While remote sensing analyses were conducted across all three regions, Tahoe, the Ruby Mountains, and the Santa Rosa Range, only the Tahoe-area cases are presented in the main text to illustrate representative outcomes. The satellite imagery for each region covered the following spatial domains: Tahoe ( $38.27^{\circ}$ – $39.37^{\circ}$  N,  $119.15^{\circ}$ – $120.59^{\circ}$  W), Santa Rosa Range ( $41.19^{\circ}$ – $41.59^{\circ}$  N,  $117.03^{\circ}$ – $118.04^{\circ}$  W), and Ruby Mountains ( $40.05^{\circ}$ – $41.09^{\circ}$  N,  $114.37^{\circ}$ – $115.49^{\circ}$  W). The corresponding satellite imagery and analysis for the Ruby and Santa Rosa regions are provided in the Appendix for completeness. The following section describes the satellite instruments and imagery used for this analysis.

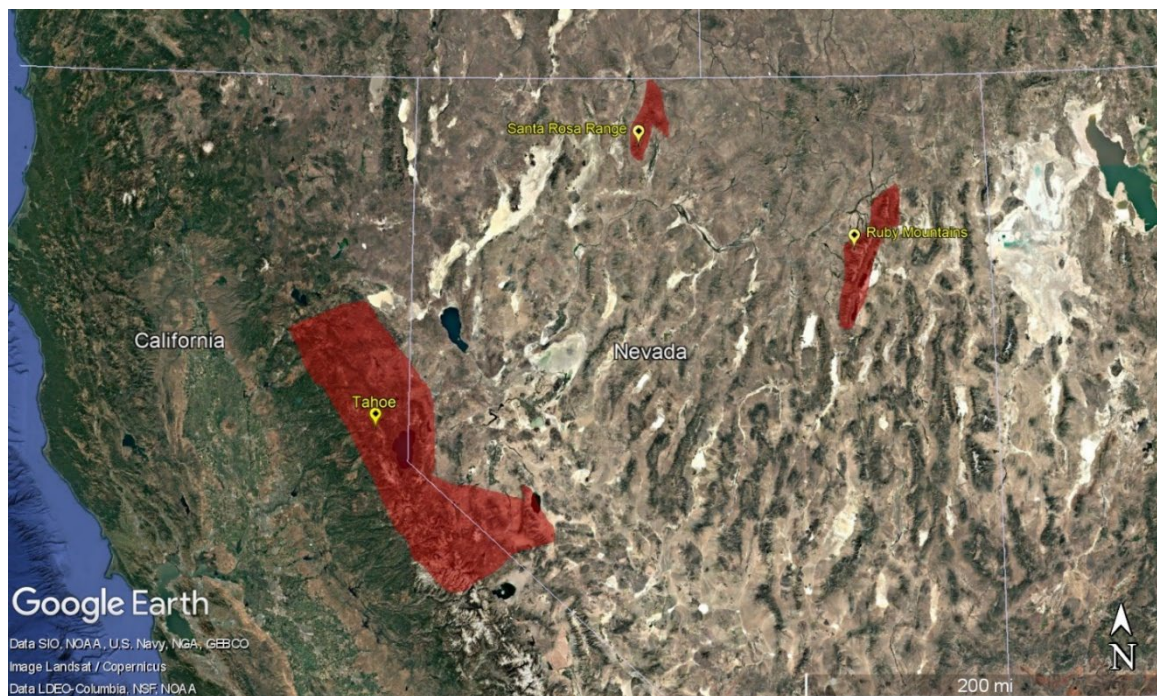


Figure 3.1. Locations of ground-based AgI generators used in cloud seeding operations across the Lake Tahoe Area, Ruby Mountains, and Santa Rosa Range in Nevada, shown with red polygons. (Base map image created using Google Earth ©).

### 3.3.2. Advanced Baseline Imager of GOES-R Series

To investigate cloud seeding case studies, the ABI GOES-R series observations were utilized due to several key advantages [54]. GOES-R offers high temporal resolution, enabling frequent imaging and continuous tracking of cloud dynamics [55]; its geostationary orbit allows continuous observation of a fixed region, facilitating the observation of localized cloud modifications resulting from seeding activities [56]; and its broad multispectral capability is essential for distinguishing cloud phases and detecting snow and ice [44]. The geostationary positioning ensures the availability of near real-time data, which are critical for assessing the temporal evolution of cloud systems and cloud seeding impacts [31].

The ABI sensor on GOES-R series satellites, including GOES-16, GOES-17, and GOES-19, provides 16 multispectral bands with advanced imaging capabilities for weather, ocean, and environmental monitoring [47,51]. It covers the Western Hemisphere with temporal resolutions from 30 seconds to 15 minutes and spatial resolutions of 0.5 km for visible band, 1 km for the NIR, and 2 km for the IR bands [45,51]. ABI operates in two scan modes: Full-Disk Mode, capturing a full-disk image every 5 minutes, and Flex Mode, which scans the full disk every 10 minutes, Continental U.S. (CONUS) every 5 minutes, and two mesoscale sectors every minute [57]. Prior to April 2019, Flex Mode produced a full-disk image every 15 minutes. Prior to April 2019, the Full-Disk scan interval was 15 minutes.

Among these, the visible bands, particularly Band 2 (0.64  $\mu\text{m}$ ), provide high spatial resolution (0.5 km), enabling detailed observation of cloud and surface boundaries. NIR

bands are crucial for snow/ice detection, and cloud phase discrimination, as they distinguish reflectance differences between ice, snow, and liquid water clouds [44,58]. IR bands are essential for assessing cloud-top temperature, identifying convective development, and retrieving atmospheric temperature and humidity profiles, supporting applications in weather forecasting, climate monitoring, and cloud-seeding assessments [59,60]. Table 3.1 provides a summary of the ABI's 16 spectral bands used in this research, including their central wavelengths and highest spatial resolutions.

With its broad spectral coverage and fine spatiotemporal resolution, ABI is a powerful tool for monitoring cloud microphysical and thermodynamic properties. In this study, we utilized ABI imagery to analyze cloud seeding events, leveraging the specific spectral bands optimized for cloud analysis. This approach supports improved understanding of seeding-induced changes to cloud dynamics and precipitation processes. To facilitate targeted analysis, the following section provides an overview of key ABI channels, highlighting their distinct observational capabilities and importance in atmospheric monitoring.

Table 3.1. GOES Advanced Baseline Imager (ABI) Channels used in this study, including their approximate central wavelength ( $\mu\text{m}$ ), respective maximum spatial resolution (km), and the cloud properties analyzed.

---

<b>Channel Number</b>	<b>Central Wavelength (<math>\mu\text{m}</math>)</b>	<b>Type</b>	<b>Highest Spatial Resolution (km)</b>	<b>Cloud Property to Detect</b>
-----------------------	------------------------------------------------------	-------------	----------------------------------------	---------------------------------

---

2	0.64	Visible (Red Band)	0.5	Cloud optical depth and thickness, Ice and liquid water path
3	0.86	Near-Infrared	1	Cloud particle size, Cloud optical depth and thickness
5	1.6	Near-Infrared	1	Cloud phase, Cloud particle size
8	6.2	Infrared (Water Vapor)	2	Water vapor content
9	6.9	Infrared (Water Vapor)	2	Water vapor content
10	7.3	Infrared (Water Vapor)	2	Water vapor content
13	10.3	Infrared (Window)	2	Cloud phase, Cloud top temperature, Ice and liquid water path
14	11.2	Infrared (Window)	2	Cloud top temperature, Precipitation potential
15	12.3	Infrared (Window)	2	Ice and liquid water path, Precipitation potential

a) Band 2 (0.64  $\mu\text{m}$ ) – Red Visible Band

The ABI Band 2, known as the "Red Visible Band," operates at 0.64  $\mu\text{m}$  with the highest spatial resolution (0.5 km) [61,62]. This fine resolution is particularly effective for identifying localized meteorological and surface features, such as fog boundaries and cumulus clouds [51]. This band plays an essential role in daytime cloud analysis, capturing reflected visible solar radiation and distinguishing clouds from land surface [44,62]. It

remains essential for monitoring atmospheric conditions and characterizing daytime clouds relevant to cloud seeding applications.

b) Band 3 (0.86  $\mu\text{m}$ ) – Vegetation Band

The 0.86  $\mu\text{m}$  is a NIR channel used during daytime that help to identify cloud boundaries and surface moisture conditions important for cloud formation and seeding. It enhances land-water contrast but requires adjustments for true-color imagery due to higher vegetation reflectance compared to the green band (0.51  $\mu\text{m}$ ) [44,51].

c) Band 5 (1.61  $\mu\text{m}$ ) – Snow/Ice Band

ABI Band 5 (1.61  $\mu\text{m}$ ) with 1 km resolution, is essential for distinguishing cloud phase by differentiating water-based (bright) from ice-based (dark) clouds due to ice absorption [44]. It effectively identifies snow and ice, which appear dark in this band compared to the 0.86  $\mu\text{m}$  band, aiding in monitoring surface and cloud conditions important for cloud seeding. Although cloud cover and motion can affect observations, Band 5 remains essential for daytime and nighttime environmental monitoring [48,51].

d) Band 8 (6.2  $\mu\text{m}$ ) – Upper-Level Water Vapor Band

The 6.2  $\mu\text{m}$  band detects moisture in the upper troposphere (250–500 hPa, ~5.5–10.3 km) [51,63], helping identify atmospheric features such as jet streams, troughs, and ridges that influence storm development. It tracks air movement in cloud-free areas, detects dry air intrusions, and provides information on upper-level moisture and vertical air motion. These capabilities support evaluating cloud seeding effectiveness. However, its ability to observe lower atmospheric moisture is limited in areas with dense cloud cover [51].

e) Band 9 (6.9  $\mu\text{m}$ ) – Mid-Level Water Vapor Band

The 6.9  $\mu\text{m}$  band monitors moisture and atmospheric motion in the mid-troposphere, important for understanding cloud formation stability [64]. It helps evaluate conditions relevant to cloud seeding by monitoring mid-level moisture and atmospheric dynamics. Its effectiveness is reduced in areas with dense cloud cover, limiting detection of lower-level moisture [51,65,66].

f) Band 10 (7.3  $\mu\text{m}$ ) – Lower-Level Water Vapor Band

The 7.3  $\mu\text{m}$  band monitors moisture and wind patterns in the lower troposphere (500–750 hPa), providing key information on low-level humidity and wind dynamics essential for cloud seeding. It offers clearer insights into lower atmospheric moisture compared to mid- and upper-level water vapor bands. However, thick clouds can limit their observations [51,64,65].

g) Band 13 (10.3  $\mu\text{m}$ ) – Clean Infrared Window Band

ABI Band 13 is less affected by water vapor absorption, making it effective for detecting atmospheric features and cloud properties. It measures cloud-top brightness temperatures (BTs), which aids in cloud phase identification, as colder clouds at high altitudes typically contain ice. Its applications include continuous cloud classification, including nighttime observations, and help estimate of cloud-top temperature and particle size [64]. However, BTs may not always correspond precisely to surface or near-surface air temperatures due to atmospheric absorption effects.

h) Band 14 (11.2  $\mu\text{m}$ ) – Infrared Longwave Window Band

The 11.2  $\mu\text{m}$  Infrared Longwave Window Band is useful for atmospheric and surface observations. Although classified as a window channel, it experiences some water vapor absorption, leading to slightly cooler BTs compared to the clean window channel (10.3  $\mu\text{m}$ ) [51]. This band contributes to cloud detection and precipitable water estimation, which are relevant for assessing atmospheric conditions in cloud seeding [64].

i) Band 15 (12.3  $\mu\text{m}$ ) – Dirty Window Band

The 12.3  $\mu\text{m}$  Dirty Window Band is an IR channel sensitive to atmospheric moisture and aerosols with more water vapor absorption than the Clean Window Band, resulting in slightly lower observed BTs, particularly in humid regions. Due to its sensitivity to both moisture and airborne particles, 12.3  $\mu\text{m}$  band is effective in identifying dust plumes and other atmospheric aerosols. When combined with 10.3  $\mu\text{m}$  channel, this band helps differentiate silicate-based particles, such as desert dust and volcanic ash, from cloud water and ice [64]. However, due to its interaction with atmospheric moisture, it is less effective for direct surface observations compared to other longwave infrared window channels.

### 3.3.3. Cloud Microphysical and Atmospheric Properties

a) Cloud particle size

The 0.86  $\mu\text{m}$  and 1.6  $\mu\text{m}$  bands are commonly used to analyze cloud properties relevant to cloud seeding [42,43,67,68]. The 0.86  $\mu\text{m}$  band, sensitive to surface reflectance and cloud cover but provides limited microphysical detail. In contrast, the 1.6  $\mu\text{m}$  band detects differences in cloud particle size and phase, which is valuable for identifying ice formation

triggered by seeding agents, as ice particles absorb strongly at this wavelength [69,70]. This enables evaluation of microphysical processes and potential snowfall enhancement [67,70].

b) Cloud phase

Cloud phase can be inferred using BT and reflectivity differences between the 1.61  $\mu\text{m}$  and 10.3  $\mu\text{m}$  bands [42,68,71]. The 1.61  $\mu\text{m}$  band highlights reflectance variations: brighter areas indicate liquid water clouds, while darker areas suggest ice clouds [72]. The 10.3  $\mu\text{m}$  band provides cloud-top temperature, where colder temperatures correspond to higher-altitude ice clouds [71,73]. Post-seeding analysis using these bands helps identify ice formation, indicating successful nucleation [71]. Mixed-phase clouds, containing both supercooled liquid water and ice, are ideal targets, as they respond well to seeding [74,75,76]. Seeding agents such as AgI act as ice-nucleating particles, enhancing precipitation through processes such as the Wegener-Bergeron-Findeisen mechanism and riming [75,77,78].

c) Cloud top temperature

Cloud top temperature is derived from BTs using the 10.3  $\mu\text{m}$  and 11.2  $\mu\text{m}$  bands [42,68,78]. In deep convective clouds, BTs at 10.3  $\mu\text{m}$  closely reflect actual cloud-top temperatures due to minimal water vapor interference [51,80,81]. The 11.2  $\mu\text{m}$  band, though also a window channel, experiences more absorption from atmospheric moisture, resulting in cooler BTs in clear sky conditions [43,80]. These bands are useful for distinguishing cloud structure and seeding impacts.

d) Cloud optical depth and thickness

Cloud optical depth is estimated using visible and IR channels. The 0.64  $\mu\text{m}$  band measures cloud reflectance, where higher reflectivity signals optically thicker clouds [42,68,83]. The 0.86  $\mu\text{m}$  band captures reflectance variations associated with cloud particle density and improves contrasts between clouds and land surface features [84]. The 10.3  $\mu\text{m}$  band complements this with BT data, where colder values indicate thicker and more developed clouds [85,86].

e) Ice and liquid water path

To evaluate the ice and liquid water path, GOES ABI bands differentiate between cloud phases [51,68,81]. The 1.6  $\mu\text{m}$  band detects ice formation, as ice absorbs more light than liquid water [82]. Brightened regions in this band over seeded areas indicate ice development, especially when supported by colder BTs from the 10.3  $\mu\text{m}$  [80]. Daytime analysis may include the 0.64  $\mu\text{m}$  band to optical thickness, while nighttime assessments observations use 10.3 and 12.3  $\mu\text{m}$  band comparisons to infer ice-phase formation [81].

f) Water vapor content

Atmospheric moisture is evaluated using the GOES ABI water vapor bands, which probe different vertical layers [51,80]. The 6.2  $\mu\text{m}$  wavelength captures upper-level moisture, 6.9  $\mu\text{m}$  monitors mid-level moisture, and 7.3  $\mu\text{m}$  focused on lower-level moisture [43,78,81,82]. Comparing moisture distribution across these bands reveals atmospheric stability and conditions favor or suppress cloud development. Combining this with IR BT

data (e.g., 10.3  $\mu\text{m}$ ) further supports the understanding of how cloud seeding effects on moisture transport and cloud microphysics.

g) Precipitation potential

Precipitation potential is evaluated through cloud-top temperature and phases analysis using IR bands [47,51]. The 11.2  $\mu\text{m}$  band detects cold, thick clouds likely to produce precipitation, while the 12.3  $\mu\text{m}$  band helps distinguish non-precipitating clouds. A reduction in BT difference between these bands can indicate ice-phase development post-seeding, suggesting enhanced precipitation potential [87].

#### 3.3.4. Radar Reflectivity

Radar reflectivity provides a quantitative measure of the energy reflected back to the radar from hydrometeors such as raindrops, snowflakes, or ice particles, and is typically expressed in decibels of reflectivity (dBZ). The National Radar Reflectivity Mosaic [88] integrates data from multiple ground-based weather radars, primarily from the NEXRAD (Next-Generation Radar) network, into a unified map, displaying the spatial distribution and intensity of precipitation over a large region [89]. The radar data used in these mosaics represent near real-time 24-hour coverage and are updated every 5 minutes, providing high temporal resolution necessary for detailed tracking of atmospheric processes [88]. In this study, the mosaic reflectivity data specifically cover the Lake Tahoe region, spanning approximately 38.89° to 39.27° N latitude and -120.39° to -119.86° W longitude.

These mosaics are particularly valuable for capturing the evolution of meso-scale convective systems and are widely used in cloud seeding studies to monitor seeded clouds and assess potential enhancements in precipitation attribute to seeding activity. Reflectivity mosaics support the comparison of precipitation pattern between target and control regions, track the movement of seeded clouds, and analyze the development of precipitation over time [90]. In this context, reflectivity data serve as a critical observational tool for post-event evaluations of seeding effectiveness [91].

### 3.4. Results and Discussion

#### 3.4.1. Meteorological Criteria for Effective Cloud Seeding

Table 3.2 summarizes the meteorological conditions recorded at the initiation of cloud seeding operations, as measured by the weather stations installed on the seeding generators across three key locations: the Ruby Mountains, the Santa Rosa Range, and the Tahoe area. Across all three sites, the data shows a consistent pattern of below- or near-freezing temperatures and moderate to high Relative Humidity (RH), both of which are essential for effective glaciogenic seeding. Such atmospheric conditions promote the growth of ice crystals following the introduction of seeding agents, particularly in supercooled liquid cloud environments. At Ruby Mountain, air temperatures during seeding operations ranged from  $-1^{\circ}\text{C}$  to  $0^{\circ}\text{C}$ , with RH values fluctuating between 56% and 94%. The wind direction varied considerably, spanning from  $190^{\circ}$  to  $268^{\circ}$ , while wind speeds remained relatively low, with gusts reaching a maximum of 18 mph. While sufficient for seeding initiation, the relatively weak wind speeds may limit the dispersion and vertical lofting of seeding

aerosols. In the Santa Rosa Range, seeding events occurred under air temperatures ranging from  $-2^{\circ}\text{C}$  to  $4^{\circ}\text{C}$ , and RH values between 57% and 88%. Wind direction varied more consistently from  $195^{\circ}$  to  $337^{\circ}$ , and gusts peaked at 16 mph. The more stable wind direction at this site, compared to the Ruby Mountains, may have supported more efficient transport of seeding aerosols into the target region, enhancing the probability of cloud-aerosol interaction and subsequent precipitation formation.

Seeding operations in the Tahoe region, where characterized by the coldest observed temperatures, with values dropping to  $-6^{\circ}\text{C}$ , and the highest RH values, which consistently remained at 96%. Wind direction was stable at  $195^{\circ}$ , while wind speeds ranged from 10 to 14 mph. These conditions represent an optimal environment for cold cloud seeding, with sustained high humidity and subfreezing temperatures facilitating effective nucleation and ice crystal growth. The consistent wind field likely aided in the efficient advection of seeded material into cloud updrafts.

Collectively, these site-specific observations provide important baseline information for identifying meteorological conditions that are favorable for effective cloud seeding operations. Such analyses are required for determining optimal timing and location for seeding, as they help ensure that the physical environment supports cloud microphysical processes necessary for precipitation enhancement. Furthermore, consistent characterization of pre-seeding conditions across different sites contributes to the reproducibility and reliability of seeding programs, informing both operational strategies and future experimental designs.

These observed meteorological conditions are generally consistent with established criteria for effective cloud seeding in mountainous regions. Previous studies and operational guidelines suggest that optimal seeding conditions typically include temperatures near or below freezing (approximately  $-2^{\circ}\text{C}$  to  $0^{\circ}\text{C}$ ), RH above 50%, and moderate, steady winds to facilitate the transport and dispersion of seeding agents within target cloud formations [1,92,93]. The recorded temperature ranges and RH values across the Ruby Mountains, Santa Rosa Range, and Tahoe area fall within these favorable parameters, supporting the potential effectiveness of seeding operations conducted during this period. Additionally, the relatively stable wind directions at Santa Rosa and Tahoe locations indicate conducive atmospheric flow patterns, which are important for the efficient delivery of seeding materials.

Table 3.2. Summary of Meteorological Conditions During Cloud Seeding Operations.

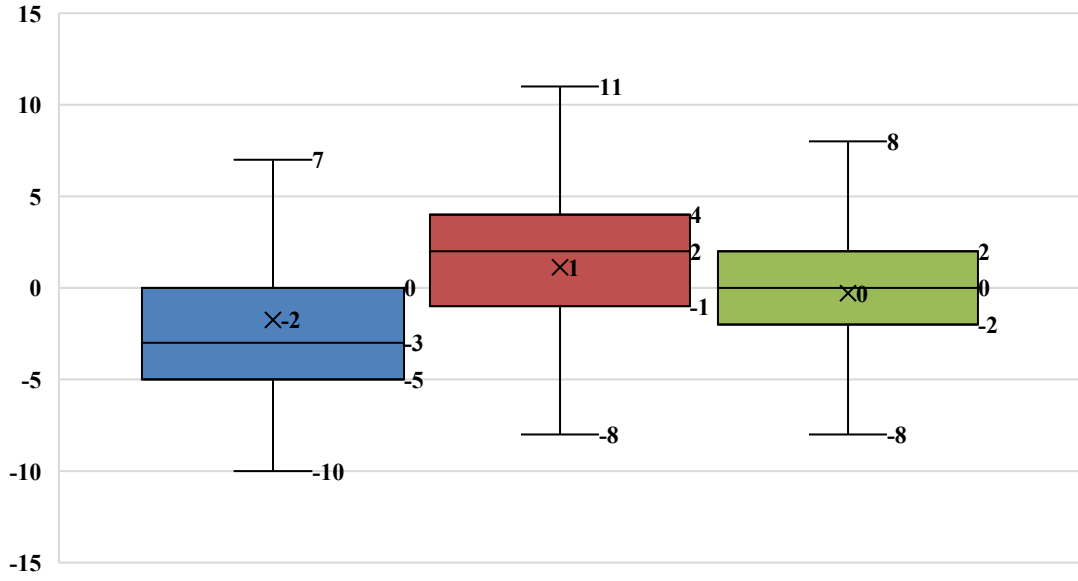
<b>Location</b>	<b>Date</b>	<b>Air Temperature (<math>^{\circ}\text{C}</math>)</b>	<b>RH (%)</b>	<b>Wind Direction (deg)</b>	<b>Wind Speed (mph)</b>	<b>Wind Gust (mph)</b>
Ruby	16-Feb-25	-1	94	224	5	11
	13-Jan-24	-1	79	190	13	18
	3-Jan-24	-1	94	268	4	7
	2-Jan-24	0	56	198	2	7
Santa Rosa	1-Mar-24	-2	57	195	5	13
	13-Jan-24	-1	88	213	7	16
	3-Jan-24	4	73	230	2	8
	2-Jan-24	2	65	337	2	5
Tahoe	16-Feb-25	-1	96	208	12	21
	11-Nov-24	-2	96	235	14	24
	20-Feb-24	-3	96	195	13	17
	4-Apr-24	-6	91	223	14	29
	1-Feb-24	-3	96	195	10	21

### 3.4.2. Site-Specific Variability in Atmospheric Conditions During Cloud Seeding

As a complement to the event-based meteorological summaries presented in the previous section, this section provides a statistical overview of the distributions of air temperature, wind speed and direction, and RH across the 288 seeding events conducted in 2024 (Figure 3.2). The 288 cloud seeding events were distributed across three locations: Tahoe (165 events), the Ruby Mountains (69 events), and Santa Rosa Range (54 events). Box-and-whisker plots are used to illustrate the variability and central tendencies of each parameter across the three locations. Each colored box plot represents the interquartile range (IQR) with the box spanning from the 25th percentile (Q1) to the 75th percentile (Q3), and the median (50th percentile) shown as the central line. Whiskers extend to the minimum and maximum values within 1.5 times the IQR, excluding statistical outliers, while a mean value is denoted by an “X” marker. This visualization facilitates a comparison of the central tendency and spread of meteorological variables across different seeding regions, highlighting site-specific variability that may influence cloud seeding operations.

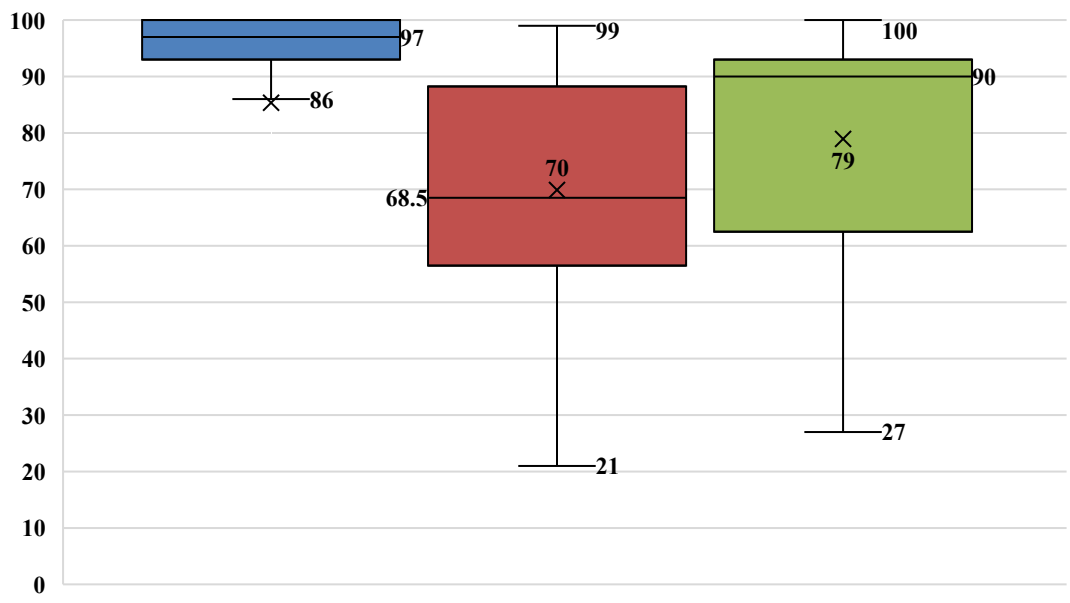
Tahoe Santa Rosa Ruby

Air Temperature (C)

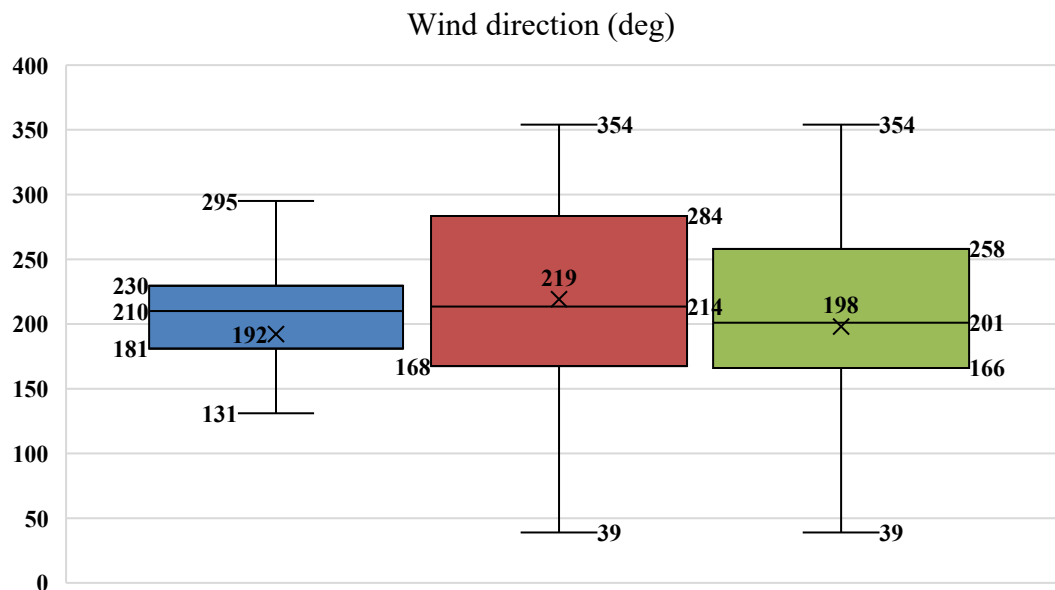


(a)

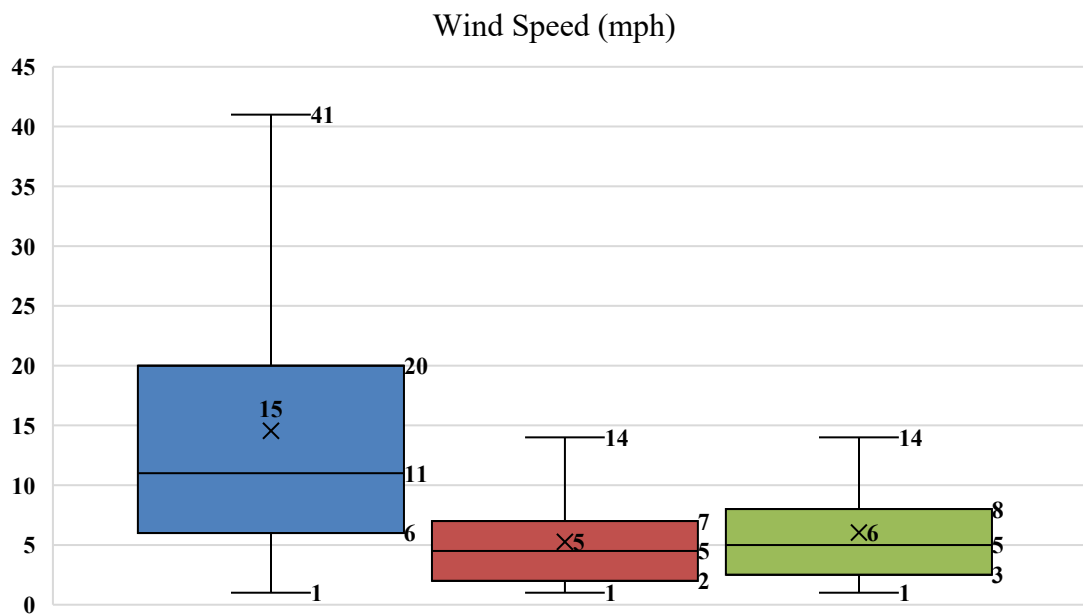
RH (%)



(b)



(c)



(d)

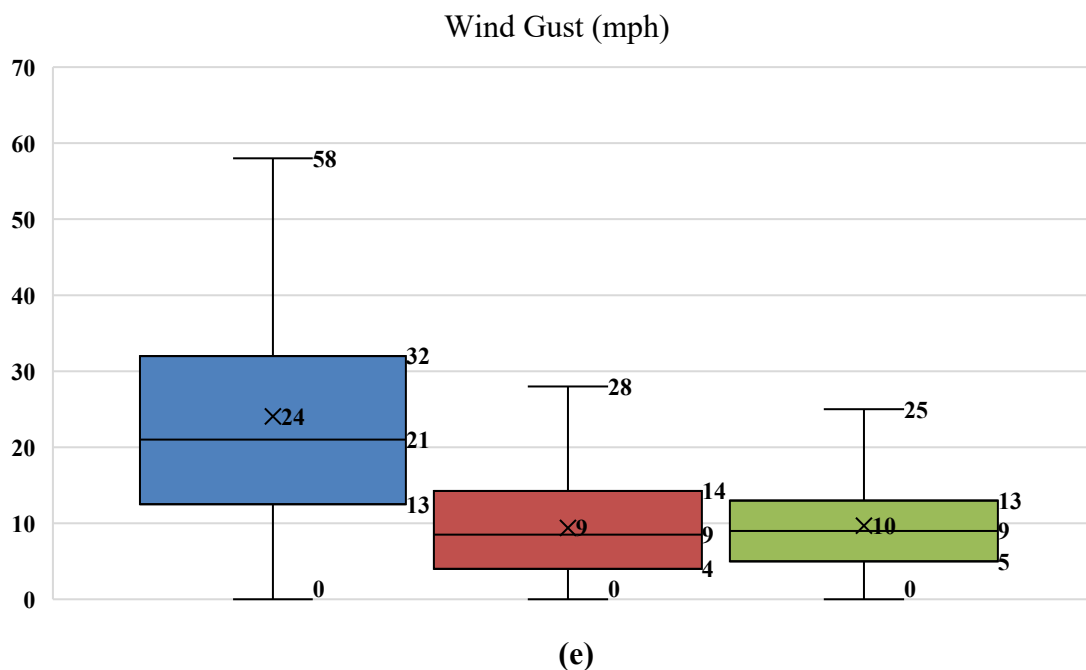


Figure 3.2. Box-and-whisker plots depicting the distribution of air temperatures recorded at Tahoe, Santa Rosa, and Ruby locations during the cloud seeding operations.

Figure 3.2a shows the air temperature distributions. Tahoe exhibits the lowest overall temperatures, with a median near  $-2^{\circ}\text{C}$  and whiskers extending from  $-10^{\circ}\text{C}$  to  $7^{\circ}\text{C}$ . In contrast, Santa Rosa has a median around  $0^{\circ}\text{C}$  and the broadest range, spanning from  $-8^{\circ}\text{C}$  to  $11^{\circ}\text{C}$ . Ruby's temperatures center slightly below  $0^{\circ}\text{C}$ , with whiskers from  $-8^{\circ}\text{C}$  to  $8^{\circ}\text{C}$ , indicating moderate variability. These distributions reinforce the earlier observation that Tahoe is generally colder than the other two sites, while Santa Rosa experiences the widest temperature fluctuations.

Figure 3.2b illustrates the distribution of RH. Tahoe generally experiences higher and more stable RH levels, with the box centered around 86–97%, whereas Santa Rosa and Ruby

exhibit wider spreads, extending down to approximately 21% and 27%, respectively. This suggests that although all three locations occasionally reach high RH, only Tahoe consistently maintain RH levels near saturation – conditions particularly favorable for hygroscopic cloud seeding techniques.

Wind direction (Figure 3.2c) shows substantial variability at all sites, with Santa Rosa displaying the broadest directional spread, whereas Tahoe wind direction appears somewhat more concentrated, indicating potentially steadier airflow patterns that may support more predictable plume transport.

Figure 3.2d presents wind speed distributions. Tahoe exhibits slightly higher median wind speeds and a wider range than the other locations. This observation aligns with the notion that stronger or more variable winds at Tahoe may enhance seeding material dispersal but also pose challenges for targeting.

Figure 3.2e reveals notable differences in wind gusts. Tahoe recorded the highest gust values - approaching 58 mph - and exhibits the greatest gust variability. Santa Rosa and Ruby remain within more moderate gust ranges (up to about 13–15 mph), suggesting relatively more stable conditions that may favor controlled seeding dispersion.

Taken together, these plots highlight additional insight into the local microclimate characteristics at each site. Tahoe tends to be colder and more humid, with stronger winds, and greater gust variability. Santa Rosa and Ruby while exhibiting greater variability in humidity and wind direction, generally experience milder wind speeds and gusts. These spatial differences highlight the importance of tailoring cloud seeding strategies to site-specific atmospheric dynamics, as variations in temperature, humidity, wind speed, and

direction can significantly influence the dispersion, activation, and effectiveness of seeding agents.

### 3.4.3. Satellite–Radar Analysis of Tahoe Region Cloud Seeding Events

In this section, we present detailed analyses of cloud seeding events over the Tahoe region using satellite remote sensing and ground-based radar observations to evaluate cloud microphysical changes and precipitation responses. These cases serve as representative examples of the broader study. Although the satellite and radar analyses in the main text focus on Tahoe-area cases to highlight typical seeding-related signatures, all cloud seeding events, spanning Tahoe, the Ruby Mountains, and Santa Rosa Range, were analyzed using a consistent method to ensure a regional comparability. Results from the Ruby and Santa Rosa events are detailed in the Appendix. The GOES satellite imagery used in this analysis was sourced from the NOAA/NESDIS Center for Satellite Applications and Research [94], and the radar images were obtained from the NOAA National Centers for Environmental Information’s Radar Viewer [88].

#### 3.4.3.1. Seeding Event 1: 11 November 2024

##### a) Satellite Remote Sensing Analysis

The analysis of GOES ABI satellite imagery across multiple spectral bands provided key insights into cloud microphysics properties and precipitation potential influenced by cloud seeding. Figure 3.3 presents different ABI channels at 20:00 UTC during the seeding event over the Tahoe region. Cloud particle size characterization utilized the 0.86  $\mu\text{m}$  (NIR) and 1.6  $\mu\text{m}$  (Shortwave IR) bands, which have differential sensitivities to liquid and ice phases.

In 0.86  $\mu\text{m}$  band, clouds appear bright due to strong reflectance from cloud droplets, making this band particularly effective for detecting water clouds. Conversely, 1.61  $\mu\text{m}$  band is more sensitive to ice particles, as ice strongly absorbs radiation at this wavelength, causing ice clouds to appear darker relative to liquid clouds. The comparative analysis between these two bands reveals regions where bright reflectance in 0.86  $\mu\text{m}$  corresponds to darker in 1.61  $\mu\text{m}$ , suggesting localized ice particle formation likely induced by seeding, consistent with effective ice nucleation.

Cloud phase determination using combined 1.61  $\mu\text{m}$  and 10.3  $\mu\text{m}$  bands confirmed the presence of ice-phase clouds in the seeded region. A moderately dark region in the 1.61  $\mu\text{m}$  band that simultaneously appears colder in the 10.3  $\mu\text{m}$  band likely indicates a mixed-phase cloud (a combination of supercooled liquid water and ice) or fully glaciated clouds at higher altitudes.

The intermediate darkness in the 1.61  $\mu\text{m}$  band, reflects partial glaciation, where some reflectance remains, while the colder temperature in the 10.3  $\mu\text{m}$  band imply high-altitude cloud tops. In the context of cloud seeding, bright reflectance in the 1.61  $\mu\text{m}$  band that transitions to darker tones while remaining cold in the 10.3  $\mu\text{m}$  band is indicative of favorable conditions for ice nucleation. Distinguishing mixed phase from fully glaciated clouds using the GOES ABI channels enhances the ability to monitor seeding impacts and improve numerical weather prediction models.

Further evaluation of cloud top temperature using the 10.3  $\mu\text{m}$  band, and the longwave IR Window channel (11.2  $\mu\text{m}$ ) revealed extensive cold cloud tops in the seeded areas. The 10.3  $\mu\text{m}$  band, less affected by atmospheric water vapor absorption, provides a more

accurate representation of cloud-top temperatures, while the 11.2  $\mu\text{m}$  band shows slightly increased sensitivity to atmospheric moisture. The observed dark blue to light blue shading in both bands indicates high-altitude, glaciated clouds likely undergoing ice-phase precipitation development. The evaluation of water vapor content using the 6.2  $\mu\text{m}$ , 6.9  $\mu\text{m}$ , and 7.3  $\mu\text{m}$  bands revealed a well-saturated upper and mid-level atmosphere, favorable for cloud development. Bright blue and white areas in the 6.2  $\mu\text{m}$ , 6.9  $\mu\text{m}$  bands show enhanced moisture upstream and over the like region, while the yellow shading in the 7.3  $\mu\text{m}$  band indicates drier air intrusion from the east. Nonetheless, the seeded mountain regions exhibit well-saturated low-level moisture condition, consistent with environments conducive to precipitation formation. Precipitation potential was further evaluated using BT differences between the 11.2  $\mu\text{m}$  and 12.3  $\mu\text{m}$  bands. These differences indicate cloud phase transitions from liquid to ice, with the spatial expansion of cold, thick clouds observed in the 11.2  $\mu\text{m}$  band reinforcing the likelihood of precipitation following seeding.

This multi-spectral satellite analysis demonstrates how GOES ABI can capture cloud microphysical changes associated with seeding operations. The presence of colder cloud tops, increased cloud optical thickness, and favorable moisture profile support the hypothesis that seeding influenced cloud dynamics to enhance precipitation potential. While direct in situ precipitation measurements remain necessary to conclusively quantify seeding effectiveness, these remote sensing observations provide valuable indicators of cloud response and can guide optimization of future seeding strategies.

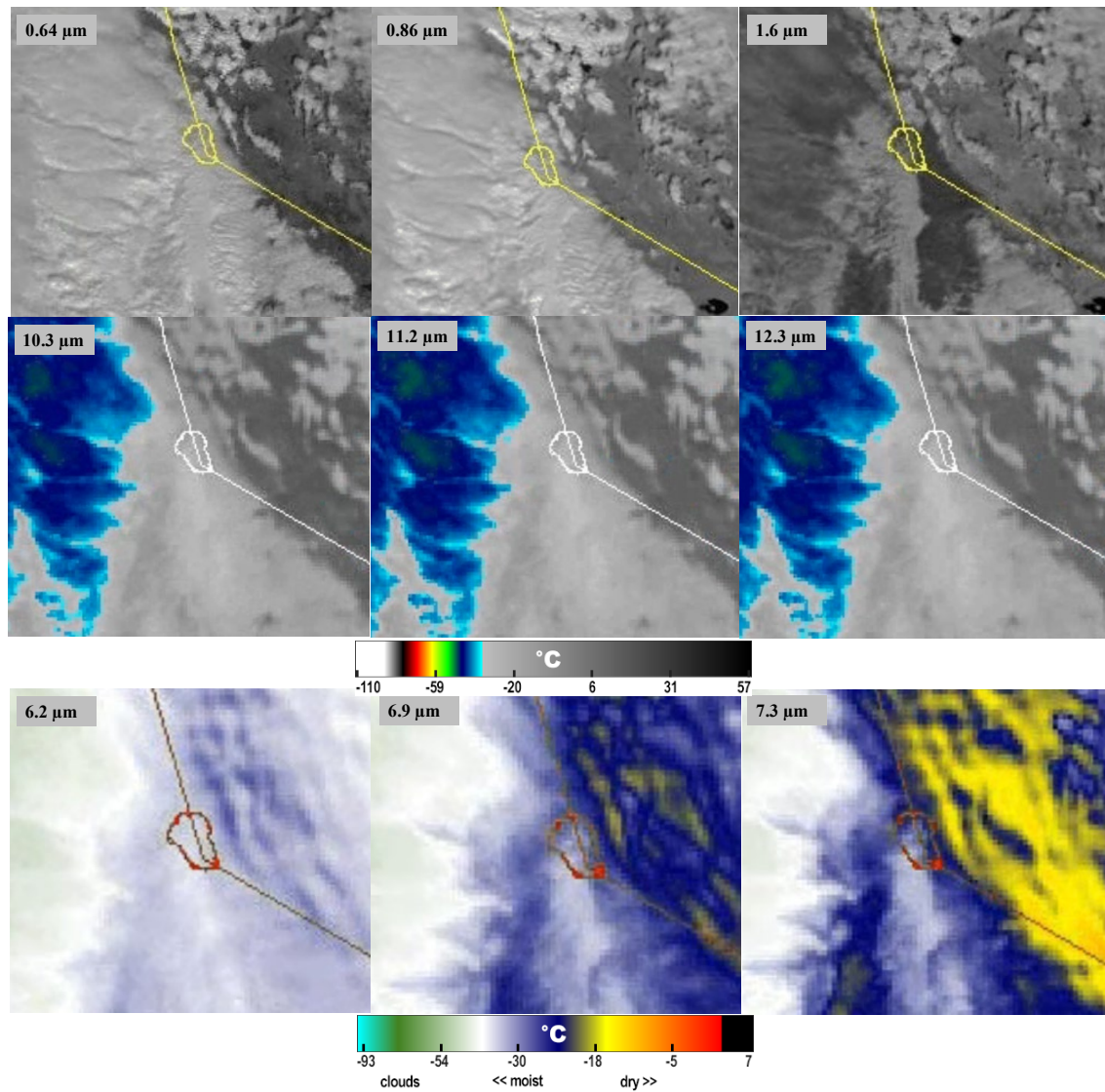


Figure 3.3. GOES ABI satellite imagery from the cloud seeding event on November 11, 2024, at 20:00 UTC, over the Tahoe region, highlighting multiple spectral bands used for cloud microphysical and thermodynamic analysis. The top row presents visible and near-infrared bands (0.64  $\mu\text{m}$ , 0.86  $\mu\text{m}$ , and 1.61  $\mu\text{m}$ ), the middle row displays infrared window bands (10.3  $\mu\text{m}$ , 11.2  $\mu\text{m}$ , and 12.3  $\mu\text{m}$ ), and the bottom row features water vapor bands (6.2  $\mu\text{m}$ , 6.9  $\mu\text{m}$ , and 7.3  $\mu\text{m}$ ). Satellite imagery from NOAA STAR GOES-West, Pacific Southwest sector.

## b) Radar-Based Analysis

Figure 3.4 presents radar reflectivity associated with the same 11 November 2024 event, with the first frame taken at 19:00 UTC, approximately one hour prior to the satellite observations, and the subsequent frames captured at 20-minute intervals (20:00, 20:20, and 20:40 UTC) to depict the temporal evolution of precipitation. Reflectivity values, ranging from weak returns in blues (~10-20 dBZ) to stronger returns in green (>30 dBZ), illustrate dynamic changes in precipitation intensity and coverage.

As the event progresses, reflectivity patterns expand and intensify, suggesting cloud growth and enhanced hydrometeor development. High reflectivity exceeding 30 dBZ is especially concentrated west and southwest of each frame, indicative of widespread moderate to heavy precipitation, likely associated with ice-phase processes such as graupel or aggregated snowflakes.

The development and merging of precipitation cells, particularly observed downwind and southwest of Lake Tahoe, point to potential orographic and seeding-enhanced effects, where supercooled liquid water was likely converted to ice, increasing precipitation efficiency. These downwind developments emerge clearly between 20:20 and 20:40 UTC, aligning with satellite-based microphysical indicators of successful seeding.

While reflectivity alone does not confirm seeding efficacy, the observed spatial growth, intensification, and persistence of radar echoes in seeded regions provide indirect evidence of enhanced precipitation processes. Such variability across different time steps and regions also reflects the influence of local atmospheric conditions, such as stability, moisture availability, and vertical wind shear, in modulating seeding outcomes.

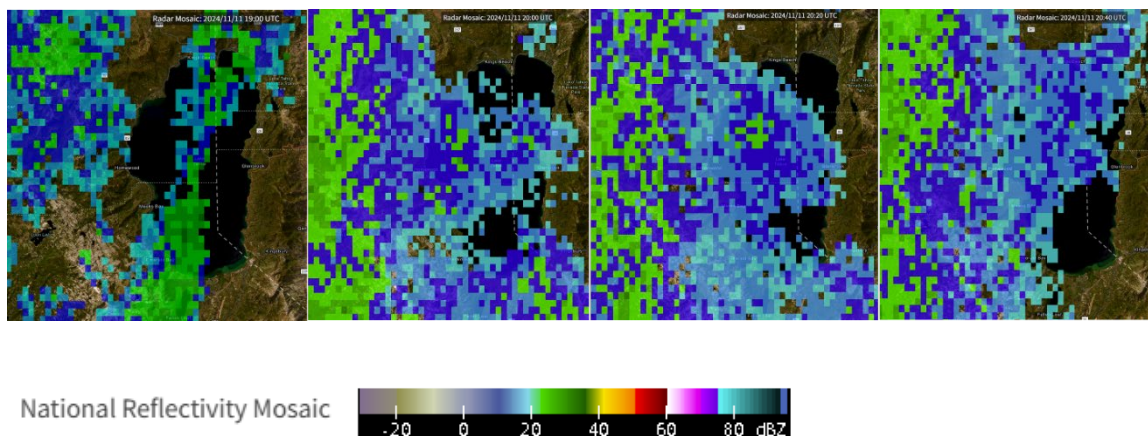


Figure 3.4. Radar reflectivity images on November 11, 2024. Sequence begins prior to seeding and illustrates the evolution of reflectivity following the initiation of cloud seeding. The images are from the National reflectivity mosaic derived from the NEXRAD (Next Generation Weather Radar) system and correspond to 19:00, 20:00, 20:20, and 20:40 UTC. The area shown is centered over the Lake Tahoe region, spanning parts of northeastern California and western Nevada. Radar images retrieved from the NOAA NCEI Radar Viewer.

### c) Integrated Satellite–Radar Interpretation for Seeding Event 1

Multi-spectral satellite imagery and radar reflectivity collectively highlight a coherent evolution of cloud and precipitation structures during the 11 November 2024 seeding event over the Tahoe region. Satellite observations indicated the development of optically thick, glaciated cloud tops and a well-saturated upper and mid-troposphere, particularly over and west of the lake - conditions favorable for ice-phase precipitation. These microphysical signatures coincided with radar-detected intensification and spatial broadening of precipitation echoes, with reflectivity exceeding 30 dBZ primarily in the western

downwind region during the 20:20 - 20:40 UTC interval. The temporal progression from glaciation signals in the satellite data to the strengthening of radar echoes supports a sequence consistent with seeded cloud development. The satellite imagery revealed cloud-top structure and phase transition processes, while the radar data captured the resulting hydrometeor growth and areal precipitation response. Together, these integrated observations provide strong, event-specific evidence of seeding enhanced precipitation during Event 1.

#### 3.4.3.2. Seeding Event 2: 20 February 2024

##### a) Satellite Remote Sensing Analysis

Satellite remote sensing observations during February 20, 2024 (Figure 3.5), cloud seeding event over the Tahoe region reveal moderate cloud development with localized indications of ice-phase processes. The analysis of cloud particle size indicates limited ice crystal growth, with subtly darkened regions in the 1.61  $\mu\text{m}$  band suggesting early-stage or partial glaciation in the targeted area. This interpretation is supported by BTs from the 10.3  $\mu\text{m}$  and 11.2  $\mu\text{m}$  bands, which show moderately cold cloud tops in the seeded zone, suggesting glaciated clouds with shallow vertical cloud development and potential for ice-phase precipitation, though less extensive and colder than in Event 1. The evaluation of cloud optical depth using the 0.64  $\mu\text{m}$  and 0.86  $\mu\text{m}$  bands shows moderate reflectance, indicative of optically denser clouds in parts of the region but without the pronounced structure or depth observed in the previous case. Water vapor content, examined across the 6.2  $\mu\text{m}$ , 6.9  $\mu\text{m}$ , and 7.3  $\mu\text{m}$  bands, indicates the presence of sufficient upper-, mid-, and lower-level moisture to support cloud development. Finally, precipitation potential, inferred from BT

differences between the 11.2  $\mu\text{m}$  and 12.3  $\mu\text{m}$  bands, shows subtle gradients, pointing to partial phase transition with reduced glaciation efficiency compared to Event 1.

The comparison between Events 1 and 2 highlights differences and similarities in cloud development and seeding effectiveness. The first case exhibits stronger signals of ice-phase cloud evolution, as evidenced by the pronounced dark regions in the 1.61  $\mu\text{m}$  band and colder, more expansive cloud tops in the 10.3  $\mu\text{m}$  and 11.2  $\mu\text{m}$  bands, suggesting greater ice particle formation. Additionally, higher optical thickness in the 0.64  $\mu\text{m}$  and 0.86  $\mu\text{m}$ , along with enhanced mid- and upper-level moisture in the 6.2  $\mu\text{m}$  and 6.9  $\mu\text{m}$  bands, supports the hypothesis that cloud seeding had a more substantial impact on cloud growth in this case.

Conversely, while the second case also shows evidence of cloud phase transition, the overall intensity of cloud development appears weaker. Some regions retain liquid-phase characteristics, as indicated by the subtler contrast between the 0.86  $\mu\text{m}$  and 1.61  $\mu\text{m}$  bands, and slightly warmer cloud-top temperatures, implying reduced vertical cloud growth or limited ice-phase processes. Additionally, lower upper-level humidity may have contributed to the reduced optical depth and glaciation, thereby limiting the effectiveness of seeding efforts.

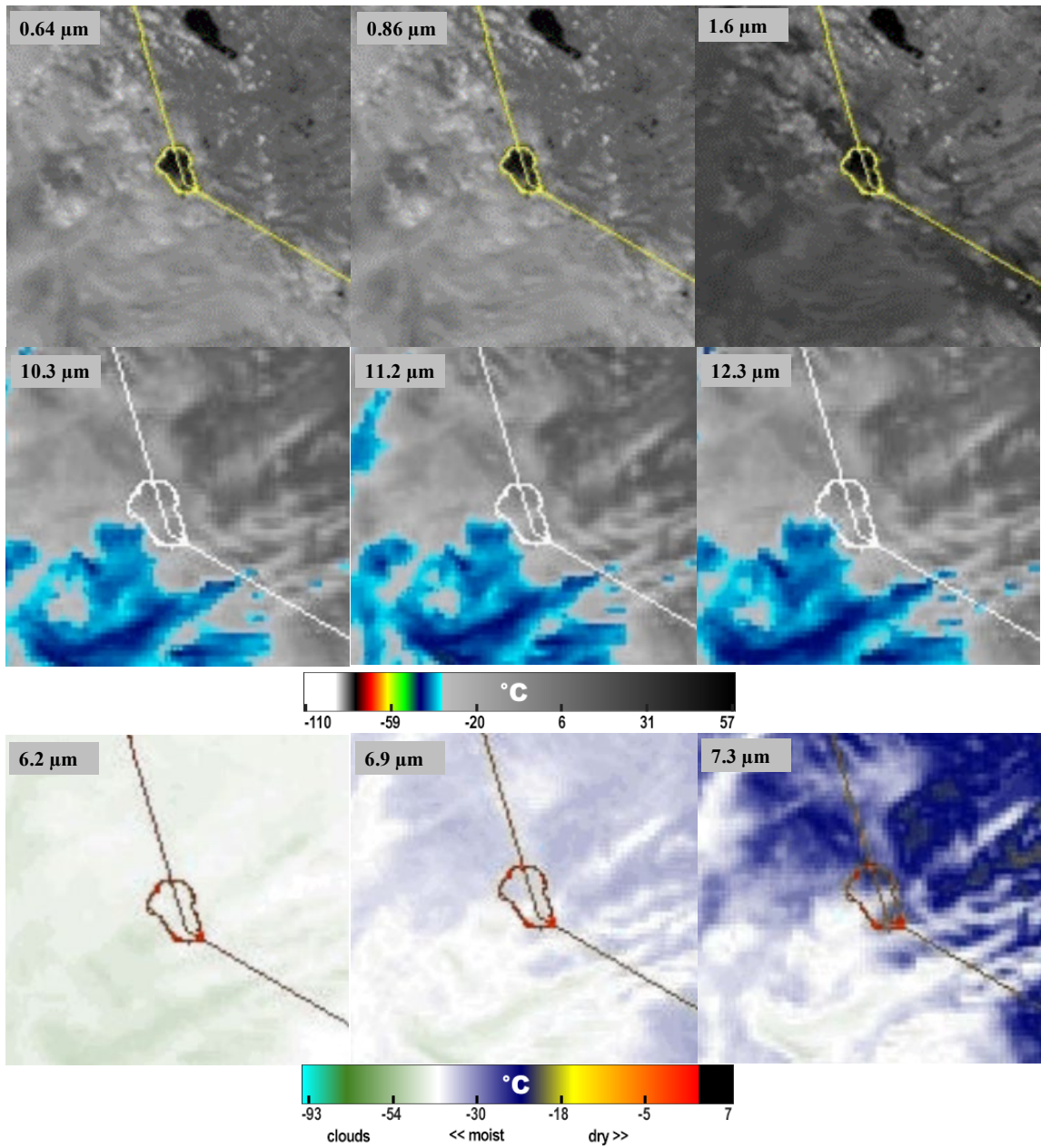


Figure 3.5. Same as Figure 3.3, but for February 20, 2024, at 21:51 UTC.

#### b) Radar-Based Analysis

Figure 3.6 shows radar reflectivity images associated with Cloud Seeding Event 2, capturing the temporal development of precipitation through four frames. The first frame

at 21:25 UTC, which is approximately one hour before the satellite observation, shows sparse and weak reflectivity, with only isolated low-intensity echoes ( $<20$  dBZ) scattered across the region. This frame represents the background atmospheric state, indicating minimal natural precipitation prior to seeding.

By 21:50 UTC, a slight increase in reflectivity emerges, primarily to the southwest of Lake Tahoe, though returns remain relatively weak and scattered. By 22:10 UTC, the radar imagery shows a clear intensification in both reflectivity and areal coverage, with echoes reaching 30-35 dBZ, particularly in areas extending northward and eastward from the Lake. At 22:30 UTC, the reflectivity field becomes more organized, with persistent moderate returns spanning significant portion of the region.

This gradual amplification and spatial expansion of radar echoes following the onset of seeding activity may reflect hydrometeor growth triggered by seeding-induced ice formation. While the initial atmospheric conditions were less active than those observed in the November case, the temporal progression of precipitation intensity, in tandem with satellite-indicated glaciation, supports the interpretation of a measurable seeding response during Event 2.

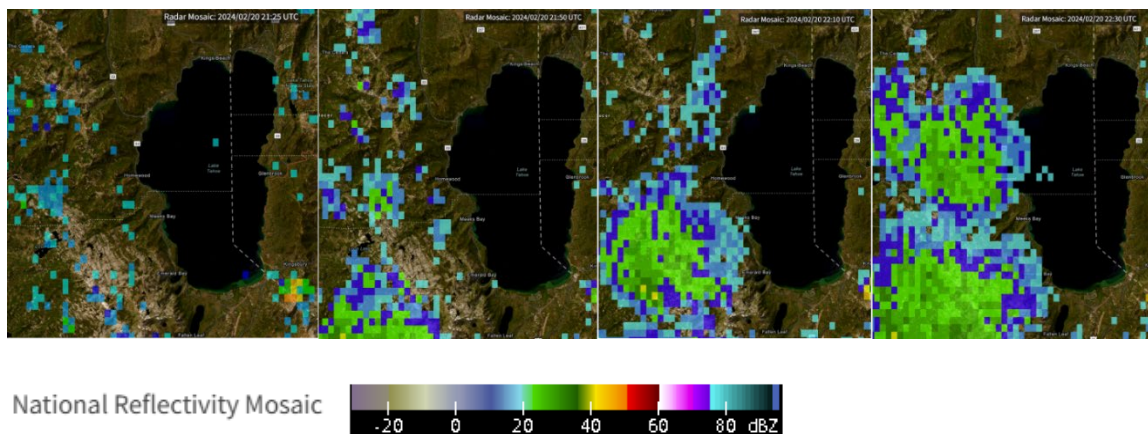


Figure 3.6. Same as Figure 3.4, but for February 20, 2024, showing data at 21:25, 21:50, 22:10, and 22:30 UTC.

### c) Integrated Satellite–Radar Interpretation for Seeding Event 2

The combined satellite and radar observations for the February 20, 2024, seeding event reveal a moderate cloud and precipitation response. GOES ABI imagery showed localized darkening in the 1.61  $\mu\text{m}$  band with modest BT depressions in the 10.3 and 11.2  $\mu\text{m}$  bands, suggesting partial glaciation within optically shallow clouds but with adequate mid- and upper-level saturation. Approximately 20–40 minutes after seeding initiation, radar reflectivity increased from isolated weak echoes (<20 dBZ) to more widespread areas exceeding 30 dBZ, particularly north and east of Lake Tahoe. This temporal evolution points to delayed hydrometeor growth, likely seeded ice-phase development progressing into organized precipitation.

While both platforms show signatures consistent with seeded cloud modification, the signal strength was weaker and more gradual compared to Event 1. The radar-sensed precipitation intensification lagged the glaciation signals, suggesting a slower cloud response under

marginal thermodynamic conditions. Together, the multi-sensor evidence points to a measurable but less robust seeding impact, constrained by less favorable vertical cloud structure.

#### 3.4.3.3. Seeding Event 3: 1 February 2024

##### a) Satellite Remote Sensing Analysis

As seen in Figure 3.7, ABI satellite data was analyzed to examine the effects of cloud seeding over the Tahoe area on 1 February 2024 at 18:16 UTC. In 0.86  $\mu\text{m}$  wavelength band, brighter reflectance indicates optically thick cloud cover, while the corresponding darkening in the 1.61  $\mu\text{m}$  band indicated enhanced absorption by ice particles, suggesting active droplet-to-ice phase transition within seeded clouds. This transition is further supported by cloud particle size analysis, which shows the expected reflectance-absorption contrast between the NIR and shortwave IR bands, consistent with ice crystal growth.

Cloud phase analysis based on the alignment of dark regions in the 1.61  $\mu\text{m}$  and 10.3  $\mu\text{m}$  bands with colder cloud tops in the 10.3  $\mu\text{m}$  IR window band reinforces the presence of glaciated clouds, implying successful heterogeneous ice nucleation potentially induced by seeding. In addition, the 10.3  $\mu\text{m}$  and 11.2  $\mu\text{m}$  bands show moderately cold cloud tops, warmer than those seen during the February 20 (Figure 3.5), November 11 (Figure 3.3), and February 16 (Figure A3.1) events in Tahoe. These signatures indicate vertical cloud development favorable for ice-phase precipitation, though somewhat limited in spatial extent.

The visible (0.64  $\mu\text{m}$ ) and NIR (0.86  $\mu\text{m}$ ) bands display high reflectance values over the seeded region, indicating optically dense and well-structured cloud layers. Minimal BT differences between the 11.2  $\mu\text{m}$  and 12.3  $\mu\text{m}$  bands further support enhanced cloud glaciation, as phase transitions reduce emissivity contrasts in these longwave channels.

Water vapor analysis indicates a saturated mid- and upper-troposphere, with no significant dry-air intrusion, suggesting a supportive thermodynamic environment for cloud development and sustained ice growth. Compared to the February 20 event, Event 3 exhibits a weaker glaciation signal and more favorable moisture structure, though still more limited in areal coverage and intensity than the November 11 case. These combined spectral observations indicate a moderate seeding response under partially supportive meteorological conditions.

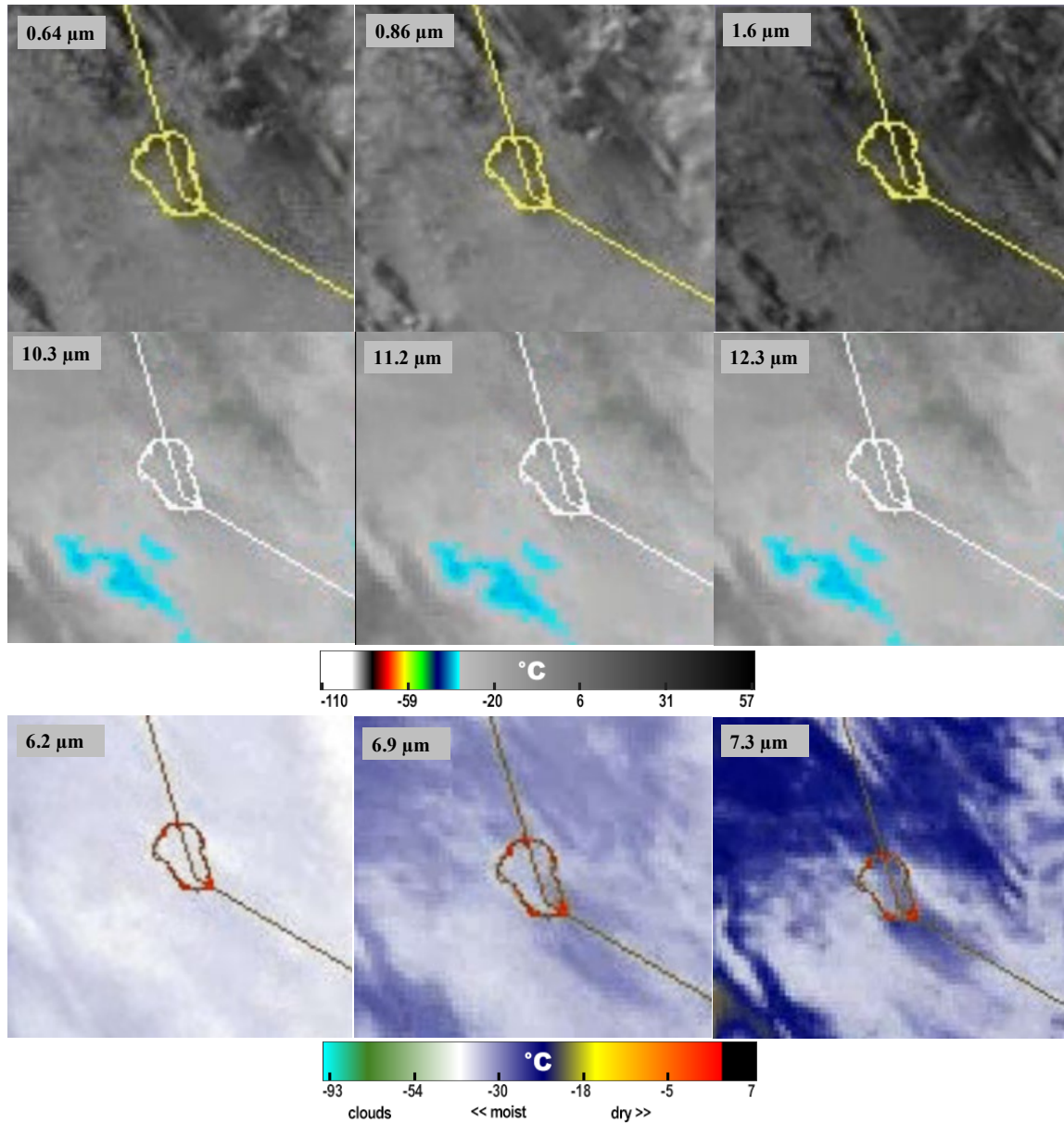


Figure 3.7. Same as Figure 3.3, but for February 1, 2024, at 18:16 UTC.

#### b) Radar-Based Analysis

Figure 3.8 presents radar reflectivity images for cloud seeding Event 3, capturing the temporal evolution of precipitation over the Tahoe region. The first frame at 17:25 UTC shows isolated weak echoes (<15 dBZ), indicating limited background precipitation prior

to the seeding operation. By 18:15 UTC, coinciding with satellite observations, low-level reflectivity begins to emerge in the southern sector of the domain, though still weak and scattered. At 18:35 UTC, the radar signal becomes more organized, with reflectivity increasing into the 25–30 dBZ range, particularly to the east and northeast of Lake Tahoe. By 18:55 UTC, the reflectivity field expands further, with localized areas exceeding 30 dBZ, consistent with the development of moderate precipitation intensity. The overall trend shows a gradual intensification and spatial expansion of radar echoes following the initiation of seeding, pointing to active hydrometeor growth under moderately supportive conditions.

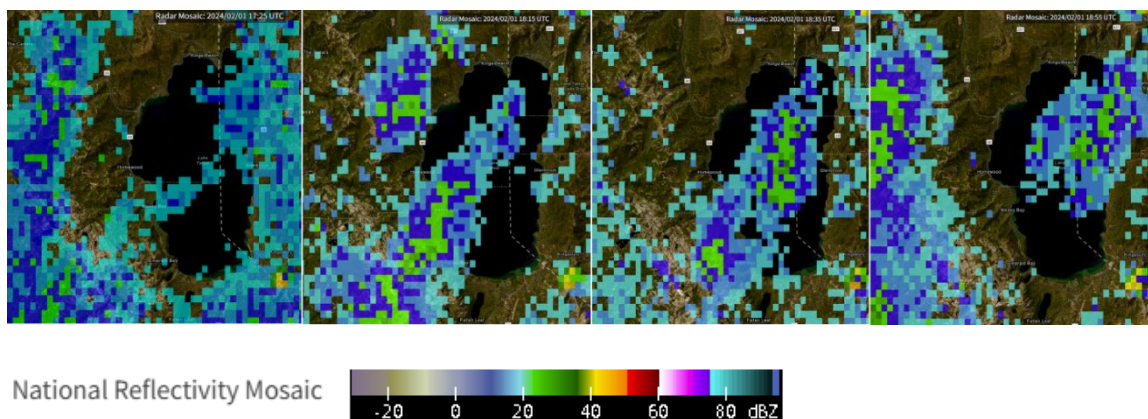


Figure 3.8. Same as Figure 3.4, but for February 1, 2024, showing data at 17:25, 18:15, 18:35, and 18:55 UTC.

### c) Integrated Satellite–Radar Interpretation for Seeding Event 3

Satellite and radar observations for the February 1, 2024, seeding event indicate a measurable but spatially confined atmospheric response. ABI imagery captured distinct signatures of ice-phase cloud development, including high reflectance in the visible bands,

differential absorption in the 1.61  $\mu\text{m}$  band, and moderately depressed BTs in the IR window channels. These features suggest active droplet-to-ice conversion within a cloud layer that, while optically thick, lacked the vertical depth seen in stronger cases.

Radar reflectivity patterns evolved gradually following seeding initiation, with echoes increasing from isolated low intensity returns to organized patches exceeding 30 dBZ. The reflectivity growth lagged the satellite-observed glaciation, aligning with a seeding-induced delay in hydrometeor formation. Unlike the broader and more intense response observed during the Event 1, the radar and satellite signals here remained localized but coherent, pointing to a seeding response shaped by marginally supportive thermodynamic conditions.

#### 3.4.3.4. Seeding Event 4: 4 April 2024

##### a) Satellite Remote Sensing Analysis

Figure 3.9 presents multi-spectral GOES ABI satellite imagery during the cloud seeding event on April 4, 2024, over the Tahoe region. A transition from small liquid droplets to ice particles is observed through NIR and shortwave IR bands with bright reflectance in the 0.86  $\mu\text{m}$  band and enhanced absorption in the 1.61  $\mu\text{m}$  band. This result confirms the presence of ice-phase clouds, suggesting that cloud seeding could promote ice nucleation. Further support for this transition comes from the cloud phase assessment, where darker regions in 1.61  $\mu\text{m}$  band correspond with colder cloud tops in the 10.3  $\mu\text{m}$  band, demonstrating the conversion of supercooled liquid water to ice. Cloud-top temperature analysis using 10.3  $\mu\text{m}$  and 11.2  $\mu\text{m}$  bands reveals widespread cold cloud tops, with deep blue shading suggesting enhanced vertical cloud development and glaciation. This cooling

implies cloud deepening, which is typically associated with enhanced precipitation potential. The same pattern can be seen in some Ruby and Santa Rosa mountains seeding events (Figures A3.2, A3.3, A3.5, A3.6, and A3.8). The cloud optical depth and thickness assessment, conducted using visible and near-infrared bands, indicated that seeded clouds exhibited increased optical thickness, as evidenced by high reflectance in 0.64  $\mu\text{m}$  and 0.86  $\mu\text{m}$  bands. These optically thick clouds suggest robust cloud microphysical development sustained during the event.

Water vapor content evaluation across 6.2  $\mu\text{m}$ , 6.9  $\mu\text{m}$ , and 7.3  $\mu\text{m}$  bands shows strong moisture availability throughout the vertical profile. Ample mid- and upper-level moisture, seen in white, provided a favorable thermodynamic environment for cloud persistence and ice-phase growth. Finally, the precipitation potential analysis, based on BT differences between the 11.2  $\mu\text{m}$  and 12.3  $\mu\text{m}$  bands, shows minimal separation, reinforcing the presence of glaciated, thick clouds. This signature, together with cloud-top cooling and phase transition indicators, suggests the cloud system evolved under conditions conducive to precipitation enhancement. Compared to earlier events, Event 4 displays similar spectral evidence of glaciation as Events 1 and 2 yet is distinguished by broader cold cloud coverage and uniformly moist profiles, highlighting its particularly favorable seeding environment. These findings demonstrate that cloud seeding facilitated ice nucleation, accompanied by thickening clouds and increasing precipitation potential under favorable atmospheric conditions.

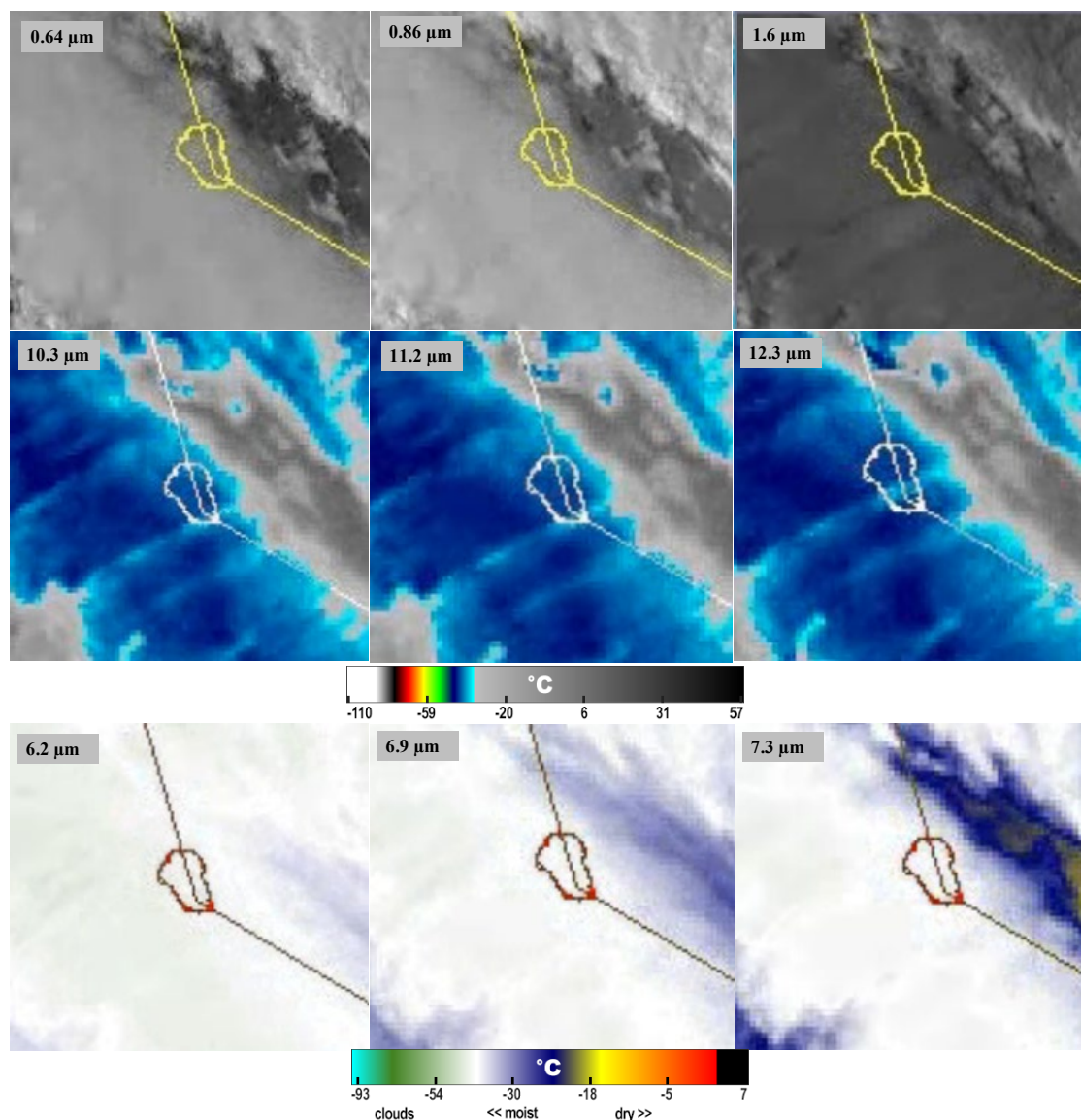


Figure 3.9. Same as Figure 3.3, but for April 4, 2024, at 23:21 UTC.

#### b) Radar-Based Analysis

Figure 3.10 shows radar reflectivity evolution during this seeding event, revealing a sustained increase in echo intensity and spatial coverage following the seeding window. Early frames display weak, scattered returns ( $<20$  dBZ), but subsequent frames depict

enhanced reflectivity, particularly over and downwind of the seeded region. The progression toward broader and more coherent radar returns, ranging from 20 to >30 dBZ, suggests hydrometeor growth likely supported by seeding-induced ice nucleation. Compared to previous events, this case exhibits a reflectivity response stronger than Event 3 but slightly weaker in areal coverage than Event 1, with spatial structure resembling Event 2.

The timing of radar intensification, relative to seeding initiation and the observed increase in dBZ values support the interpretation of enhanced precipitation development, potentially modulated by favorable mid- and upper-level moisture as seen in satellite observations. Collectively, these radar trends reinforce the hypothesis that cloud seeding in this event contributed to precipitation enhancement under conducive synoptic and thermodynamic conditions.

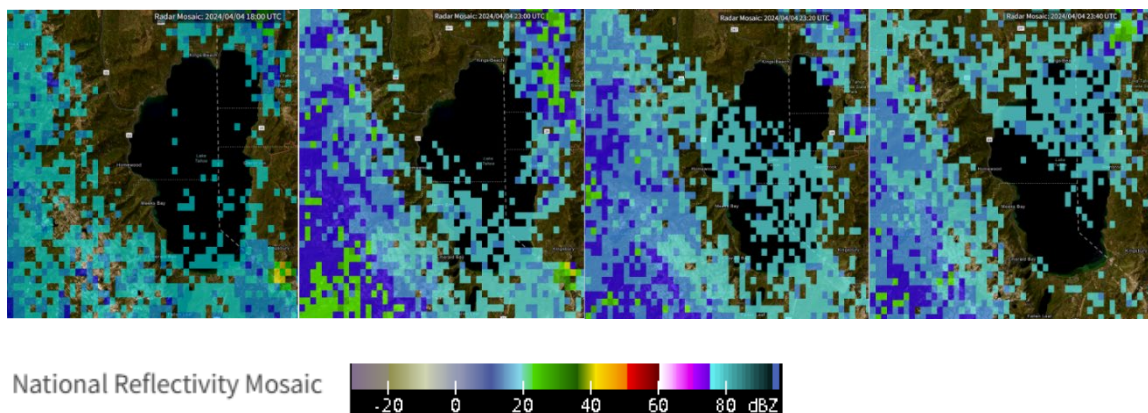


Figure 3.10. Same as Figure 3.4, but for April 4, 2024, showing data at 18:00, 23:00, 23:20, and 23:40 UTC.

c) Integrated Satellite–Radar Interpretation for Seeding Event 4

The temporal consistency between the development of radar echoes and the satellite-indicated glaciation suggests a coherent atmospheric response to cloud seeding on 4 April 2024. While radar reflectivity values remained moderate, the spatial expansion and structural organization of echoes following seeding indicate active hydrometeor growth. Unlike some previous events where the radar response was either minimal or fragmented, Event 4 demonstrates sustained echo development across the seeded region. This evolution aligns temporally with the expected post-seeding interval and reflects a stable precipitation regime. The collocation of radar intensification with favorable satellite-derived thermodynamic indicators, without relying solely on peak reflectivity, offers a more nuanced view of seeding effectiveness. In combination, the observations point to a productive interaction between the seeded clouds and the prevailing atmospheric conditions, resulting in a measurable, if moderate, enhancement of precipitation processes.

### 3.5. Summary and Conclusions

This study investigated the microphysical and thermodynamic responses to glaciogenic cloud seeding across multiple winter weather events in three mountainous regions of Nevada: Tahoe, the Ruby Mountains, and the Santa Rosa Range. Using multispectral satellite imagery from the GOES-16 ABI and regional NEXRAD radar reflectivity, we evaluated the extent to which seeded clouds displayed physical signatures associated with enhanced precipitation potential. The central hypothesis guiding this analysis was that remote sensing observations, particularly satellite-derived indicators of glaciation, cloud-

top cooling, and optical thickening, could be linked with radar-observed hydrometeor growth to assess seeding impacts in varying atmospheric regimes.

Although the visual analysis presented in the main text focused on four representative seeding events from the Tahoe region, all events across the three study regions were analyzed using a consistent methodology. Satellite imagery for the Ruby Mountains and Santa Rosa Range are provided in the Appendix. The meteorological conditions for all study regions were included in the main analysis, offering crucial context for interpreting the seeding outcomes.

Our analysis revealed that seeding responses varied significantly by region, reflecting differences in local meteorological conditions and cloud properties. Events in the Tahoe region consistently exhibited strong seeding signatures, including clear transitions from liquid to ice phase in satellite observations, colder and thickening cloud tops, and sustained increases in radar reflectivity. These responses were most apparent when ambient conditions supported seeding effectiveness - namely, cold temperatures, abundant mid- and upper-tropospheric moisture, and favorable wind shear. In contrast, cases in the Santa Rosa Range typically lacked sufficient supercooled liquid water and exhibited warmer cloud tops and thinner cloud optical depth, resulting in weaker cloud and radar responses. The Ruby Mountains presented mixed results, with some events, such as on January 13, 2024, at 17:11 UTC (Figure A3.7) displaying strong microphysical changes, while others revealed only marginal seeding effects. Key satellite-derived indicators of successful seeding included enhanced absorption in the 1.61  $\mu\text{m}$  band paired with bright reflectance in the 0.86  $\mu\text{m}$  band, suggesting droplet-to-ice conversion. These spectral patterns were often

accompanied by cloud-top cooling in the 10.3 and 11.2  $\mu\text{m}$  bands, and minimal BT differences between 11.2  $\mu\text{m}$  and 12.3  $\mu\text{m}$ , evidence of glaciation and precipitation potential. Radar reflectivity complemented these findings, especially when increases in dBZ were observed following the initiation of seeding. Meteorological analysis further clarified these findings by identifying region-specific atmospheric conditions that influenced seeding effectiveness. Tahoe events benefited from colder environments and deeper moisture profiles, while Santa Rosa and Ruby displayed broader variability in temperature, humidity, and wind structure. These results underscore the importance of tailoring cloud seeding strategies to regional atmospheric conditions, particularly those that support supercooled liquid water, vertical development, and ice-phase transitions.

A major contribution of this study is the development of a reproducible framework for satellite–radar integration, which enables a more robust and multi-dimensional assessment of seeding outcomes. While satellite data alone can reveal microphysical cloud changes, and radar data can verify precipitation development, their combined use allows for a fuller characterization of the seeding lifecycle from initial cloud-phase transitions to hydrometeor growth and potential surface impacts. This dual approach is particularly effective in marginal or ambiguous cases, where individual sensor data may be inconclusive. In practical terms, the findings from this study can inform more precise and adaptive operational seeding programs. By leveraging satellite and radar data in tandem, cloud seeding efforts can be better targeted, monitored, and evaluated, ensuring greater efficiency and effectiveness. Moreover, the satellite–radar framework presented here provides a scalable and transferable tool for similar evaluations in other regions, particularly where ground-based observations may be limited. Overall, this work contributes to both the

scientific understanding and operational practice of cloud seeding by demonstrating that spectral and structural cloud properties observed through remote sensing can reliably indicate seeding outcomes. By aligning physical cloud processes with observational evidence, this integrative approach strengthens our ability to assess and optimize precipitation enhancement strategies in diverse atmospheric environments.

### 3.6. References

1. Brientjes RT. A review of cloud seeding experiments to enhance precipitation and some new prospects. *Bull Am Meteorol Soc.* 1999;80(5):805-20.
2. Guo X, Zheng G, Jin D. A numerical comparison study of cloud seeding by silver iodide and liquid carbon dioxide. *Atmos Res.* 2006;79(3-4):183-226.
3. Essien M. Evaluation of cloud seeding techniques for precipitation enhancement. *Glob J Clim Stud.* 2023;1(1):53-64.
4. Mehdizadeh G, Erfani E, McDonough F, Hosseinpour F. Quantifying the influence of cloud seeding on ice-particle growth and snowfall through idealized microphysical modeling. *Atmosphere (Basel).* 2024;15(12):1460.
5. Mehdizadeh G, Hosseinpour FE, McDonough F, Erfani E. Studying the mechanistic impacts of cloud seeding on snowfall with insights from a cloud microphysical model [poster]. Graduate Poster Symposium; 2023 Nov; Reno, NV. DOI:10.13140/RG.2.2.17127.42408.
6. Yu X, Dai J, Lei H, Xu X, Fan P, Chen Z, et al. Physical effect of cloud seeding revealed by NOAA satellite imagery. *Chin Sci Bull.* 2005;50:45-52.

7. Lin KI, Chung KS, Wang SH, Chen LH, Liou YC, Lin PL, et al. Evaluation of hygroscopic cloud seeding in warm-rain processes by a hybrid microphysics scheme using a WRF model: a real case study. *Atmos Chem Phys*. 2023;23(18):10423-38.
8. Mehdizadeh G, Hosseinpour F, Erfani E, McDonough F. Impacts of atmospheric conditions on cloud seeding: a numerical approach. In: *AGU Fall Meeting Abstracts*; 2024 Dec; San Francisco, CA. Washington (DC): American Geophysical Union; 2024. Abstract A21G-1809.
9. Cotton WR, Pielke RA. *Human Impacts on Weather and Climate*. 2nd ed. Cambridge: Cambridge University Press; 2007.
10. Flossmann AI, Manton M, Abshaev A, Brientjes R, Murakami M, Prabhakaran T, Yao Z. Review of advances in precipitation-enhancement research. *Bull Am Meteorol Soc*. 2019;100(8):1465-80.
11. Geerts B, Pokharel B, Kristovich DAR. Blowing snow as a natural glaciogenic cloud-seeding mechanism. *Mon Weather Rev*. 2015;143(12):5017-33.
12. Jensen A, Watts A, Richards M. DRI unmanned cloud-seeding realizes beyond visual line of sight. *Phys.org* [Internet]. 2017 Feb 17 [cited 2025 Jul 9]. Available from: <https://phys.org/news/2017-02-dri-unmanned-cloud-seeding-visual-line.html>
13. Wu X, Yan N, Yu H, Niu S, Meng F, Liu W, Sun H. Advances in the evaluation of cloud seeding: statistical evidence for the enhancement of precipitation. *Earth Space Sci*. 2018;5(9):425-39.

14. Dong X, Zhao C, Huang Z, Mai R, Lv F, Xue X, et al. Increase of precipitation by cloud seeding observed from a case study in November 2020 over Shijiazhuang, China. *Atmos Res.* 2021;262:105766.
15. Muñoz LMP. Seeding change in weather modification globally. *WMO Bull.* 2017;66(1):16.
16. Silverman BA. A critical assessment of glaciogenic seeding of convective clouds for rainfall enhancement. *Bull Am Meteorol Soc.* 2001;82(5):903-24.
17. United States Government Accountability Office. *Cloud Seeding Technology: Assessing Effectiveness and Other Challenges* [Internet]. Washington (DC): GAO; 2024. Report No.: GAO-25-107328. [cited 2025 Jul 9]. Available from: <https://www.gao.gov/products/gao-25-107328>
18. Fajardo C, Costa G, Sánchez-Fortún S. Potential risk of acute toxicity induced by AgI cloud seeding on soil and freshwater biota. *Ecotoxicol Environ Saf.* 2016;133:433-41.
19. Malik S, Bano H, Rather RA, Ahmad S. Cloud seeding: its prospects and concerns in the modern world—a review. *Int J Pure Appl Biosci.* 2018;6(5):791-6.
20. Gholaminejad A, Mehdizadeh G, Dolatimehr A, Arfaeinia H, Farjadfard S, Dobaradaran S, et al. Phthalate esters pollution in the leachate, soil, and water around a landfill near the sea, Iran. *Environ Res.* 2024;248:118234.
21. Mehdizadeh G, Nikoo MR, Talebbeydokhti N, Vanda S, Nematollahi B. Hypolimnetic aeration optimization based on reservoir thermal stratification simulation. *J Hydrol.* 2023;625:130106.

22. Birgani SA, Zadeh SS, Davari DD, Ostovar A. Deep learning applications for analysing concrete surface cracks. *Int J Appl Data Sci Eng Health*. 2024;1(2):69-84.
23. Ostovar A. Comparative Life Cycle Assessment (LCA) of Different Asphalt Emulsion Types [master's thesis]. Reno (NV): Univ. of Nevada, Reno; 2023.
24. Mardi R, Ostovar A. Seismic performance and sustainability of BRB and SMA-braced structures under incremental dynamic analysis. *J Sustainabil*. 2025;1(1).
25. Ostovar A, Davari DD, Dzikuć M. Determinants of design with multilayer perceptron neural networks: a comparison with logistic regression. *Sustainability*. 2025;17(6):2611.
26. Dong X, Zhao C, Yang Y, Wang Y, Sun Y, Fan R. Distinct change of supercooled liquid cloud properties by aerosols from an aircraft-based seeding experiment. *Earth Space Sci*. 2020;7(8):e2020EA001196.
27. Rosenfeld D, Zhu Y, Wang M, Zheng Y, Goren T, Yu S. Aerosol-driven droplet concentrations dominate coverage and water of oceanic low-level clouds. *Science*. 2019;363(6424):eaav0566.
28. Yue Z, Rosenfeld D, Liu G, Dai J, Yu X, Zhu Y, et al. Automated mapping of convective clouds (AMCC) thermodynamical, microphysical, and CCN properties from SNPP/VIIRS satellite data. *J Appl Meteorol Climatol*. 2019;58(4):887-902.
29. Anuar SNS, Narashid RH, Razak TR, Hashim S, Rahim A, Boharsi SN. Cloud seeding potential areas from remote sensing of low-level cloud. In: *Proc 20th IEEE Int Colloquium on Signal Processing & Its Applications (CSPA)*; 2024 Mar; Penang, Malaysia. Piscataway (NJ): IEEE; 2024. p. 35-40.

30. Rosenfeld D, Lensky IM. Satellite-based insights into precipitation formation processes in continental and maritime convective clouds. *Bull Am Meteorol Soc.* 1998;79(11):2457-76.
31. Rosenfeld D, Yu X, Dai J. Satellite-retrieved microstructure of AgI seeding tracks in supercooled layer clouds. *J Appl Meteorol.* 2005;44(6):760-7.
32. Yu X, Dai J, Rosenfeld D, Lei H, Xu X, Fan P, et al. Comparison of model-predicted transport and diffusion of seeding material with NOAA satellite-observed seeding track in supercooled layer clouds. *J Appl Meteorol.* 2005;44(6):749-59.
33. Wang J, Yue Z, Rosenfeld D, Zhang L, Zhu Y, Dai J, et al. Evolution of an AgI cloud-seeding track in central China as seen by a combination of radar, satellite, and disdrometer observations. *J Geophys Res Atmos.* 2021;126(11):e2020JD033914.
34. Pagano TS, Durham RM. Moderate resolution imaging spectroradiometer (MODIS). In: *Sensor Systems for the Early Earth Observing System Platforms.* Proc SPIE 1939; 1993. p. 2-17.
35. Jin S, Gao C, Li J. Atmospheric sounding from Fengyun-3C GPS radio occultation observations: first results and validation. *Adv Meteorol.* 2019;2019:4780143.
36. Zheng S, Wang G, Huang X, Miao C, Xing W, Chen S, et al. Improvement and design of transmitter modifier wind cooling protection for CINRAD/CB weather radar. *J Geosci Environ Prot.* 2018;6(11):139-46.
37. Friedrich K, Higgins S, Masters FJ, Lopez CR. Articulating and stationery PARSIVEL disdrometer measurements in conditions with strong winds and heavy rainfall. *J Atmos Oceanic Technol.* 2013;30(9):2063-80.

38. Raupach TH, Berne A. Correction of raindrop size distributions measured by Parsivel disdrometers, using a two-dimensional video disdrometer as a reference. *Atmos Meas Tech.* 2015;8(1):343-65.
39. Morrison AE, Siems ST, Manton MJ. On a natural environment for glaciogenic cloud seeding. *J Appl Meteorol Climatol.* 2013;52(5):1097-104.
40. Bessho K, Date K, Hayashi M, Ikeda A, Imai T, Inoue H, et al. An introduction to Himawari-8/9—Japan's new-generation geostationary meteorological satellites. *J Meteorol Soc Jpn.* 2016;94(2):151-83.
41. Greenwald TJ, Pierce RB, Schaack TK, Otkin JA, Rogal M, Bah K, et al. Real-time simulation of the GOES-R ABI for user readiness and product evaluation. *Bull Am Meteorol Soc.* 2016;97:245-61.
42. Schmit TJ, Gunshor MM, Menzel WP, Gurka JJ, Li J, Bachmeier AS. Introducing the next-generation Advanced Baseline Imager on GOES-R. *Bull Am Meteorol Soc.* 2005;86(8):1079-96.
43. Schmit TJ, Lindner BL, Jung JA, Gunshor MM. GOES-R Advanced Baseline Imager (ABI) spectral bands. *J Appl Meteorol.* 2005;44(11):1735-42.
44. Schmit TJ, Lindstrom SS, Gerth JJ, Gunshor MM. Applications of the 16 spectral bands on the Advanced Baseline Imager (ABI). *J Oper Meteorol.* 2018;6(4):33-46.
45. Kalluri S, Alcala C, Carr J, Griffith P, Lebar W, Lindsey D, et al. From photons to pixels: processing data from the Advanced Baseline Imager. *Remote Sens.* 2018;10(2):177.
46. Flossmann AI, Wyszogrodzki AA, Jensen D. Review of advances in precipitation-enhancement research. *Bull Am Meteorol Soc.* 2019;100(8):1465-90.

47. Heidinger AK, Pavolonis MJ, Calvert C, Hoffman J, Nebuda S, Straka W III, et al. ABI cloud products from the GOES-R series. In: Goodman SJ, Schmit TJ, Daniels JM, Jamilkowski ML, editors. *The GOES-R Series*. Amsterdam: Elsevier; 2020. p. 43-62.
48. Afzali Goroooh V, Kalia S, Nguyen P, Hsu KL, Sorooshian S, Ganguly S, et al. Deep neural network cloud-type classification (DeepCTC) model and its application in evaluating PERSIANN-CCS. *Remote Sens*. 2020;12(2):316.
49. Gunshor MM, Schmit TJ, Pogorzala D, Lindstrom S, Nelson JP. GOES-R series ABI imagery artifacts. *J Appl Remote Sens*. 2020;14(3):032411.
50. Zheng G, Brown CW, DiGiacomo PM. Retrieval of oceanic chlorophyll concentration from GOES-R Advanced Baseline Imager using deep learning. *Remote Sens Environ*. 2023;295:113660.
51. Schmit TJ, Griffith P, Gunshor MM, Daniels JM, Goodman SJ, Lehair WJ. A closer look at the ABI on the GOES-R series. *Bull Am Meteorol Soc*. 2017;98(4):681-98.
52. Griffith DA, Solak ME. The potential use of winter cloud seeding programs to augment the flow of the Colorado River. Colorado White Paper: report to the Upper Colorado River Commission; 2006 Mar.
53. Simon M. Enhancing the weather: governance of weather modification activities in the United States. *Wm Mary Environ Law Policy Rev*. 2021;46:149-207.
54. Guo X, Lin D, Wu F. Analysis of precipitation process and operational precipitation enhancement in Panxi region based on cloud parameters retrievals from China's next-generation geostationary meteorological satellite FY-4A. *Atmosphere (Basel)*. 2023;14(6):922.

55. Yan L, Zhou Y, Wu Y, Cai M, Peng C, et al. FY-4A measurement of cloud-seeding effect and validation of a catalyst T&D algorithm. *Atmosphere (Basel)*. 2024;15(5):556.
56. Helder D, Doelling D, Bhatt R, Choi T, Barsi J. Calibrating geosynchronous and polar orbiting satellites: sharing best practices. *Remote Sens*. 2020;12(17):2786.
57. Schmit TJ, Gunshor MM. ABI imagery from the GOES-R series. In: Goodman SJ, Schmit TJ, Daniels JM, Jamilkowski ML, editors. *The GOES-R Series*. Amsterdam: Elsevier; 2020. p. 23-34.
58. Miller SD, Seaman CJ, Rogers MA, Kidder SQ. The importance of shortwave-infrared observations for remote sensing of snow and ice properties from space. *Remote Sens*. 2021;13(5):873.
59. Schmit TJ, Li J, Lee S-J, Li Z, Dworak R, Lee Y-K. Legacy atmospheric profiles and derived products from GOES-16: validation and applications. *Earth Space Sci*. 2019;6(9):1730-48.
60. Li Z, Xu J, Schmit TJ, Zhou X. Observing convective cloud development using GOES-16 ABI: a case study analysis. *Atmosphere (Basel)*. 2021;12(8):1013.
61. Dror T, Chekroun MD, Altaratz O, Koren I. Deciphering organization of GOES-16 green cumulus through the empirical orthogonal function lens. *Atmos Chem Phys*. 2021;21(16):12261-72.
62. Bah MK, Gunshor MM, Schmit TJ. Generation of GOES-16 true color imagery without a green band. *Earth Space Sci*. 2018;5(9):549-58.

63. Wimmers A, Griffin S, Gerth J, Bachmeier S, Lindstrom S. Observations of gravity waves with high-pass filtering in the new generation of geostationary imagers and their relation to aircraft turbulence. *Weather Forecast.* 2018;33(1):139-44.
64. Nam K, Wang F, Yan K, Zhu G. Characteristics and time-series monitoring by GOES-17 of volcano plume on 15 Jan 2022 from Tonga submarine eruption. *Geoenviron Disasters.* 2023;10(1):1-17.
65. Lee JR, Li J, Li Z, Wang P, Li J. ABI water vapor radiance assimilation in a regional NWP model by accounting for the surface impact. *Earth Space Sci.* 2019;6(9):1652-66.
66. Miller NB, Gunshor MM, Merrelli AJ, L'Ecuyer TS, Schmit TJ, Gerth JJ, et al. Imaging considerations from a geostationary orbit using the short-wavelength side of the mid-infrared water-vapor absorption band. *Earth Space Sci.* 2022;9(1):e2021EA002080.
67. Lensky IM, Rosenfeld D. Clouds-Aerosols-Precipitation Satellite Analysis Tool (CAPSAT). *Atmos Chem Phys.* 2008;8(22):6739-53.
68. National Weather Service. GOES-R ABI Bands Quick Information Guide (Cheat Sheet), NOAA Weather Forecast Office Corpus Christi, 2017. Available online: [http://weather.gov/media/crp/GOES-R\\_Cheat\\_Sheet.pdf](http://weather.gov/media/crp/GOES-R_Cheat_Sheet.pdf) (accessed on 31 July 2025).
69. Peng J, Yu Y. GOES-R Advanced Baseline Imager (ABI) algorithm theoretical basis document for surface albedo. Washington (DC): NOAA; 2020.
70. Xu W, Chang F-L, Li Z, Guo J. Satellite-based retrieval of cloud microphysical properties: recent advances and perspectives. *Remote Sens.* 2023;15(3):678.

71. Mayer B, Emde C, Gasteiger J. Radiative transfer in cloudy atmospheres: challenges and advances. *J Quant Spectrosc Radiat Transf.* 2024;205:123-45.
72. Bachmeier S. Mixed-phase stratiform clouds in an Arctic air mass. *CIMSS Satellite Blog* [Internet]. 2017 Dec 28 [cited 2025 Jul 9]. Available from: <https://cimss.ssec.wisc.edu/satellite-blog>
73. Harkema S, DiGangi JP, Zondlo MA. Observations of ice supersaturation and cirrus clouds using a novel water vapor sensor. *Atmos Meas Tech.* 2021;14(2):1231-45.
74. Wang Y, Fan J, Zhang R, Leung LR, Franklin C. Improving bulk microphysics parameterizations in simulations of aerosol effects. *J Geophys Res Atmos.* 2024;119(8):4564-82.
75. Mülmenstädt J, Sourdeval O, Delanoë J, Quaas J. Frequency of occurrence of rain from liquid-, mixed-, and ice-phase clouds derived from A-Train satellite retrievals. *Geophys Res Lett.* 2015;42(15):6502-9.
76. Noh YJ, Seaman CJ, Vonder Haar TH, Hudak DR, Rodriguez P. Comparisons and analyses of aircraft and satellite observations for wintertime mixed-phase clouds. *J Geophys Res Atmos.* 2011;116(D18).
77. Korolev A. Limitations of the Wegener–Bergeron–Findeisen mechanism in the evolution of mixed-phase clouds. *J Atmos Sci.* 2007;64(9):3372-5.
78. Hillger DW, Ellrod GP. Detection of important atmospheric and surface features by employing principal component image transformation of GOES imagery. *Journal of Applied Meteorology.* 2003 May;42(5):611-29.
79. Costa A, Sherwood SC, Renno NO. Role of supercooled water in decay of mixed-phase clouds over the Southern Ocean. *J Clim.* 2017;30(16):6229-40.

80. Bedka KM, Minnis P, Duda DP. Properties of satellite-observed transient tropospheric cooling events associated with overshooting convection. *J Appl Meteorol Climatol*. 2021;60(1):3-23.
81. Lindsey DT, Grasso LD, Monette S. Use of the 1.38  $\mu\text{m}$  channel for improved thin cirrus detection. *J Appl Meteorol Climatol*. 2012;51(5):998-1012.
82. Hillger DW, Kopp TJ, Lee TF. GOES-14 Super Rapid Scan Operations to prepare for GOES-R. *J Appl Remote Sens*. 2013;7(1):073462.
83. Walther A, Heidinger AK. The IAPP cloud detection and analysis package. *J Geophys Res Atmos*. 2012;117(D19).
84. Minnis P, Harrison EF, Stowe LL, Gibson GR, Denn FM, Doelling DR, et al. Radiative climate forcing by the Mount Pinatubo volcanic eruption. *Science*. 1995;270(5233):75-7.
85. Minnis P, Young DF, Garber DP, Nguyen L. Cloud optical properties derived from satellite data. *J Clim*. 2002;15(10):1261-82.
86. Platnick S, King MD, Ackerman SA, Menzel WP, Baum BA, Riedi J, et al. The MODIS cloud products: algorithms and examples from Terra. *IEEE Trans Geosci Remote Sens*. 2003;41(2):459-73.
87. Kuo CP, Kummerow C. Merging TEMPEST microwave and GOES-16 geostationary IR soundings for improved water vapor profiles. *Atmos Meas Tech*. 2024;17(18):5637-53.
88. NOAA National Centers for Environmental Information. NCEI radar viewer: composite reflectivity radar image [Internet]. Asheville (NC): NOAA; 2025 [cited 2025 Jul 9]. Available from: <https://www.ncei.noaa.gov/maps/radar/>

89. Tang J, Matyas CJ. High-efficiency weather radar mosaic image generation framework. In: Proc IEEE Int Geosci Remote Sens Symp (IGARSS); 2021 Jul; Brussels, Belgium. Piscataway (NJ): IEEE; 2021. p. 367-9.
90. Zhang J, Howard K, Langston C, Vasiloff S, Kaney B, Arthur A, et al. National Mosaic and Multi-Sensor QPE (NMQ) system: description, results, and future plans. Bull Am Meteorol Soc. 2011;92(10):1321-33.
91. Geerts B, Miao Q, Yang Y, Rasmussen R, Breed D. An airborne profiling radar study of the impact of glaciogenic cloud seeding on snowfall from winter orographic clouds. J Atmos Sci. 2010;67(10):3286-302.
92. Breed D, Rasmussen R, Weeks C, Boe B, Deshler T. Evaluating winter orographic cloud seeding: design of the Wyoming Weather Modification Pilot Project. J Appl Meteorol Climatol. 2014;53(2):282-99.
93. Langerud DW, Boe BA, Keyes CG Jr. How to implement a cloud-seeding program. In: Guidelines for Cloud Seeding to Augment Precipitation. Reston (VA): ASCE; 2016. p. 163-89.
94. NOAA STAR. GOES-West – sector view: Pacific Southwest [Internet]. College Park (MD): NOAA/NESDIS Center for Satellite Applications and Research; accessed 2025 Jul 6. Available from: <https://www.star.nesdis.noaa.gov/GOES/sector.php?sat=G18&sector=psw>

## 3.7. Appendix

## Tahoe Area Seeding on 16 February 2025

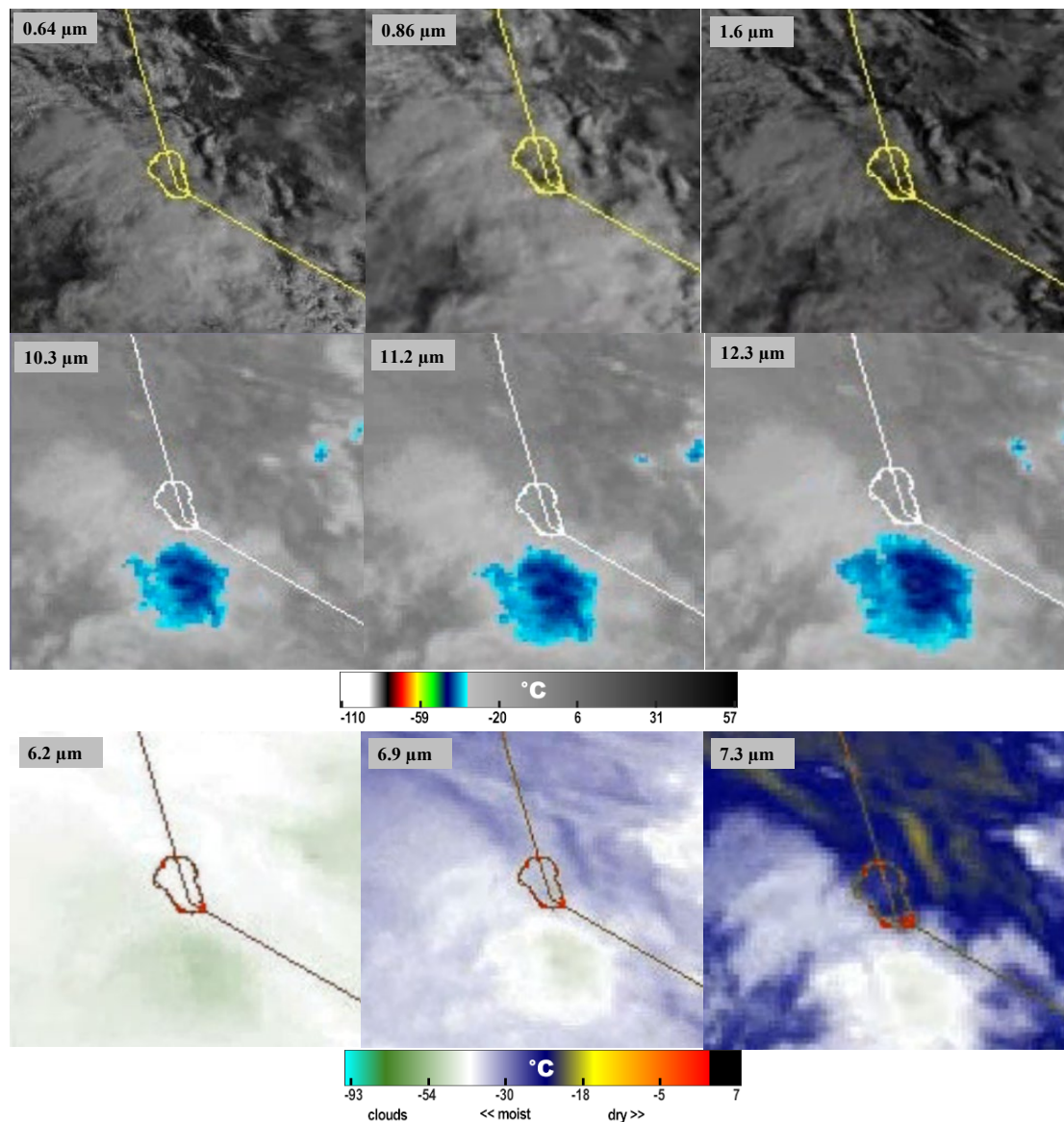


Figure A3.1. GOES BI satellite imagery from the cloud seeding event on February 16, 2025, at 17:36 UTC, over the Tahoe region, highlighting multiple spectral bands used for cloud microphysical analysis. The top row presents visible and near-infrared bands (0.64  $\mu\text{m}$ , 0.86  $\mu\text{m}$ , and 1.61  $\mu\text{m}$ ), the middle row displays infrared window bands (10.3  $\mu\text{m}$ ,

11.2  $\mu\text{m}$ , and 12.3  $\mu\text{m}$ ), and the bottom row features water vapor bands (6.2  $\mu\text{m}$ , 6.9  $\mu\text{m}$ , and 7.3  $\mu\text{m}$ ).

### Santa Rosa Seeding on 17 January 2024

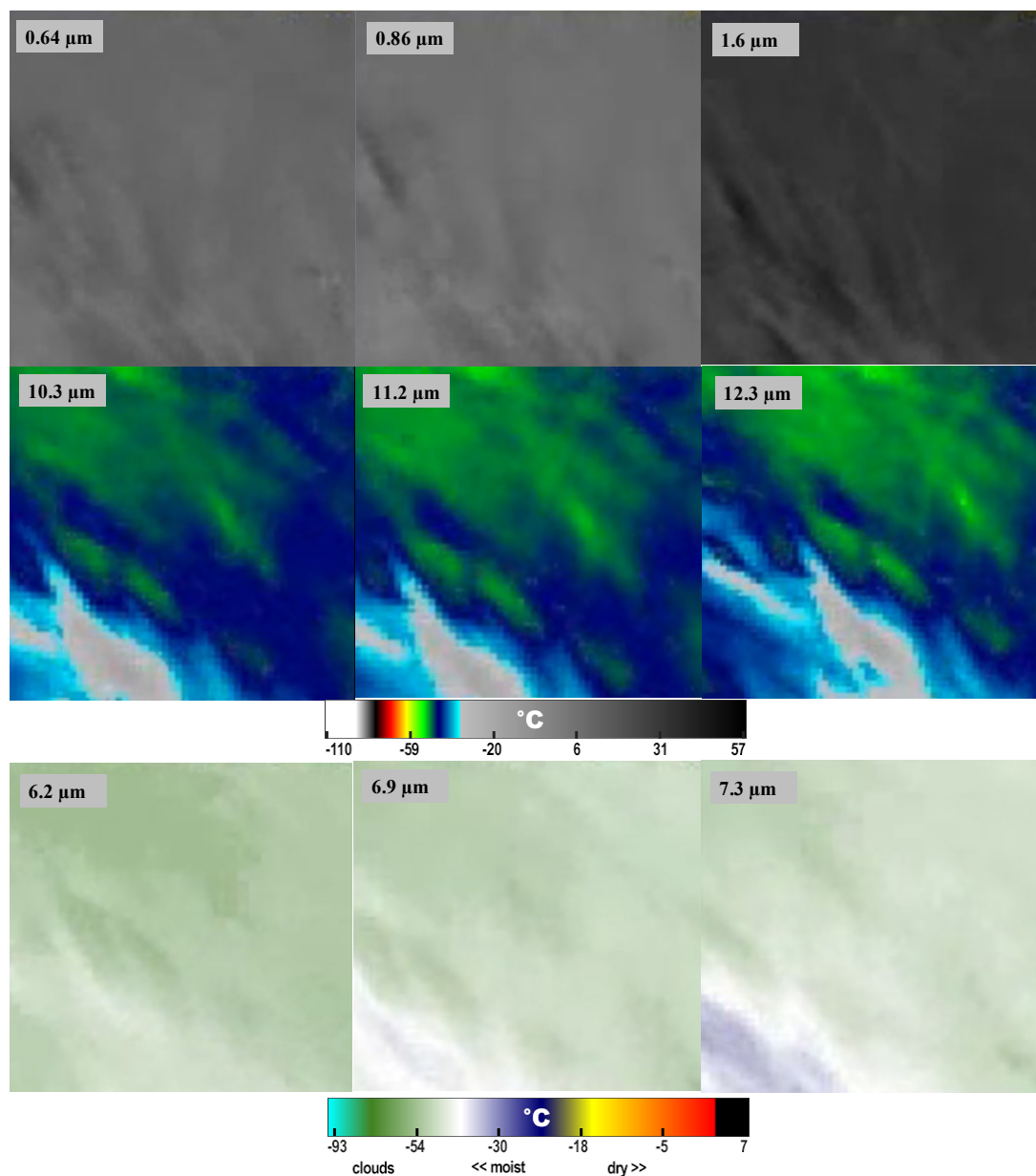


Figure A3.2. Same as Figure A3.1 but for January 17, 2024, at 17:26 UTC, over the Santa Rosa Mountain.

## Santa Rosa Seeding on 2 January 2024

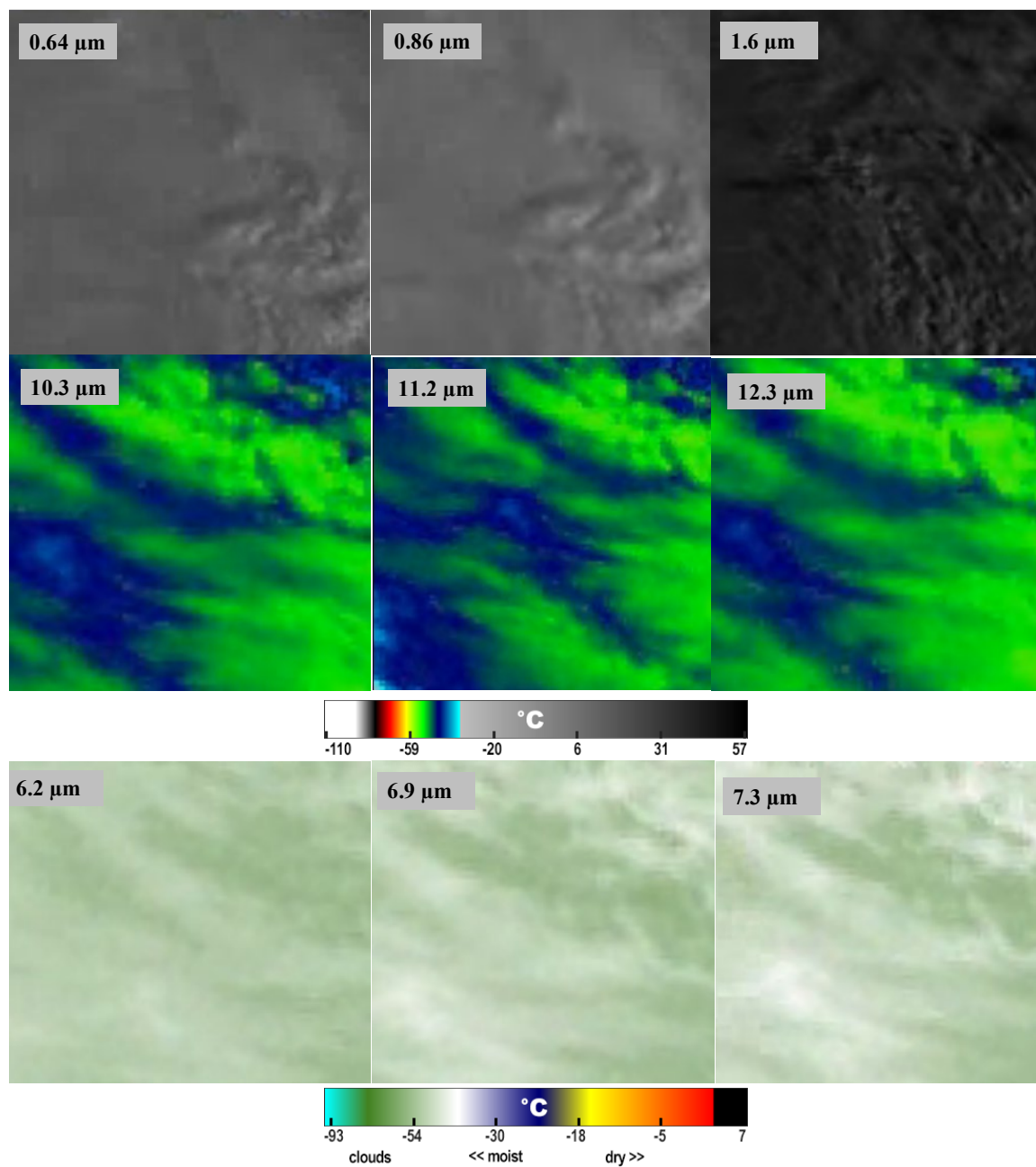


Figure A3.3. Same as Figure A3.1 but for January 2, 2024, at 17:17 UTC, over the Santa Rosa Mountain.

## Santa Rosa Seeding on 3 January 2024

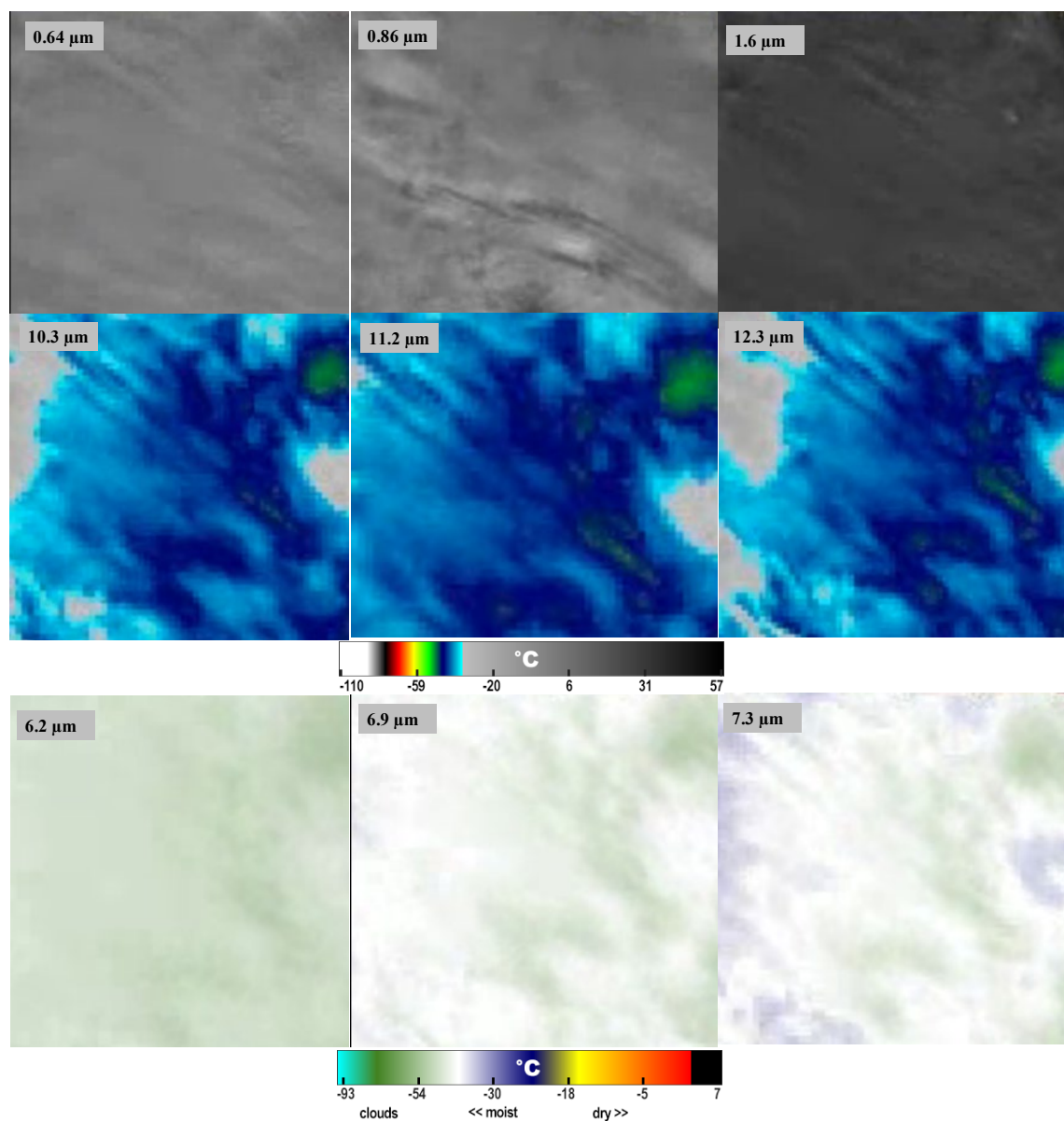


Figure A3.4. Same as Figure A3.1 but for January 3, 2024, at 20:06 UTC, over the Santa Rosa Mountain.

## Santa Rosa Seeding on 2 March 2024

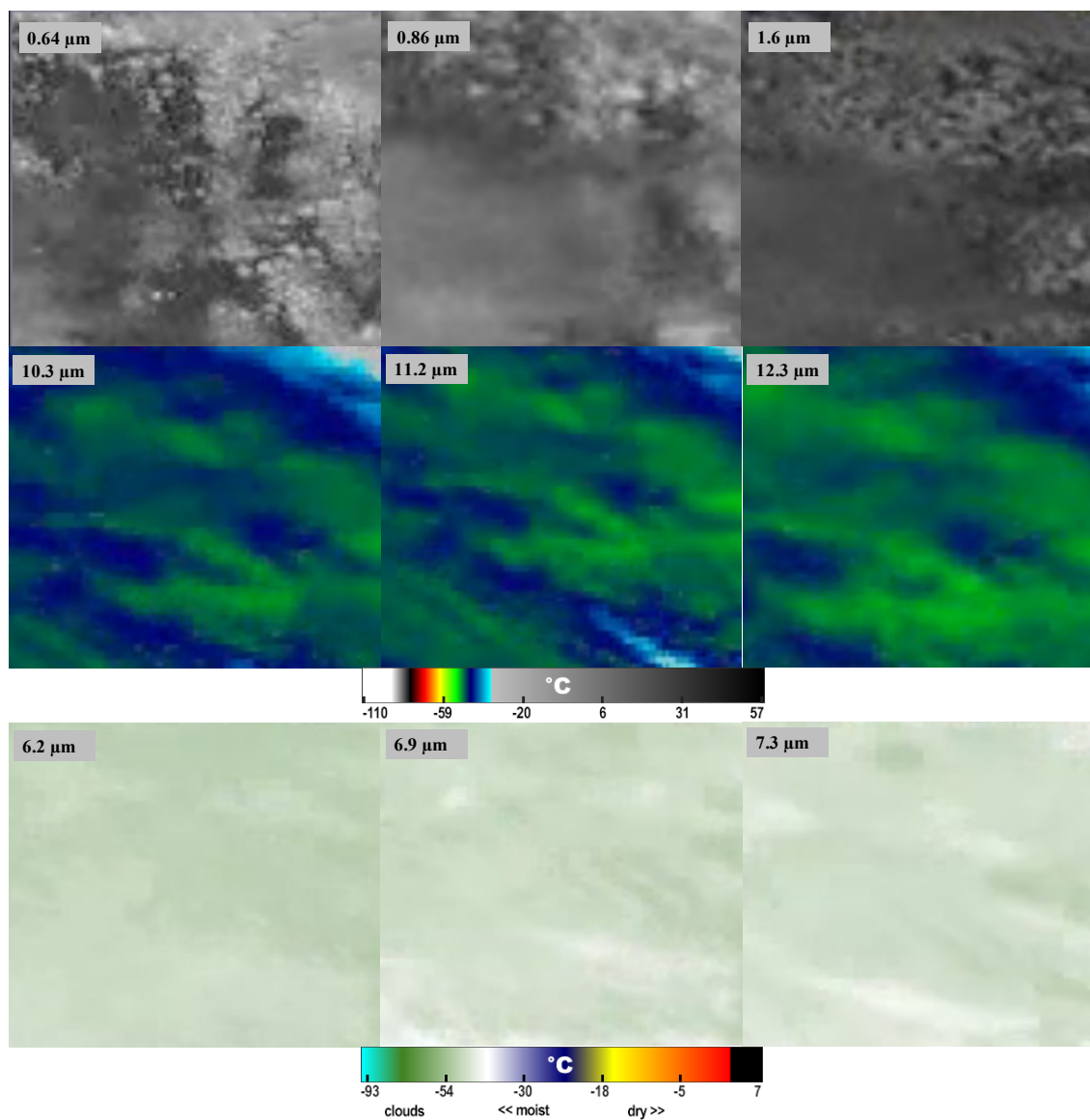


Figure A3.5. Same as Figure A3.1 but for March 2, 2024, at 23:06 UTC, over the Santa Rosa Mountain.

## Ruby Seeding on 16 February 2025

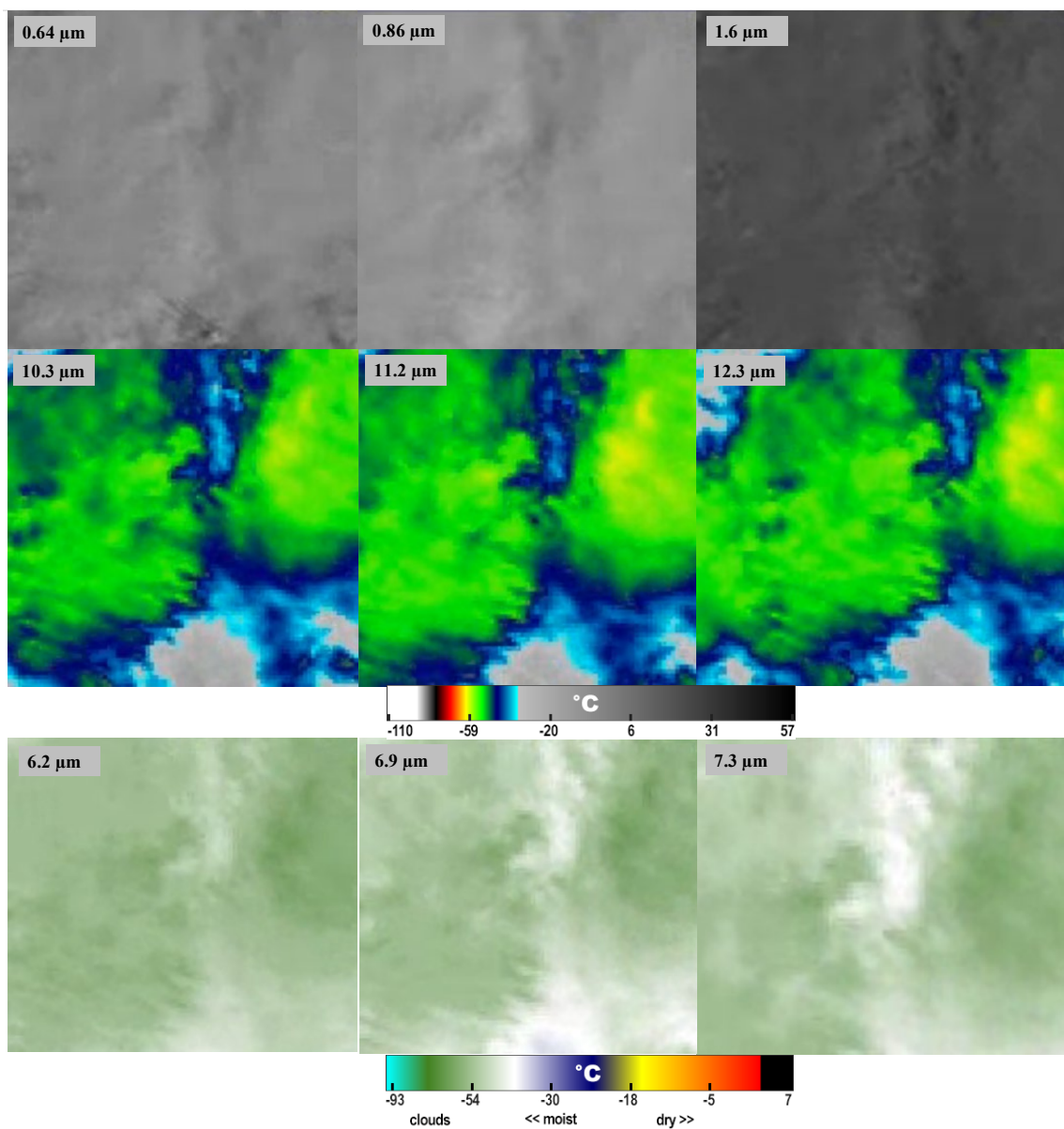


Figure A3.6. Same as Figure A3.1 but for February 16, 2025, at 17:36 UTC, over the Ruby Mountain.

## Ruby Seeding on 13 January 2024

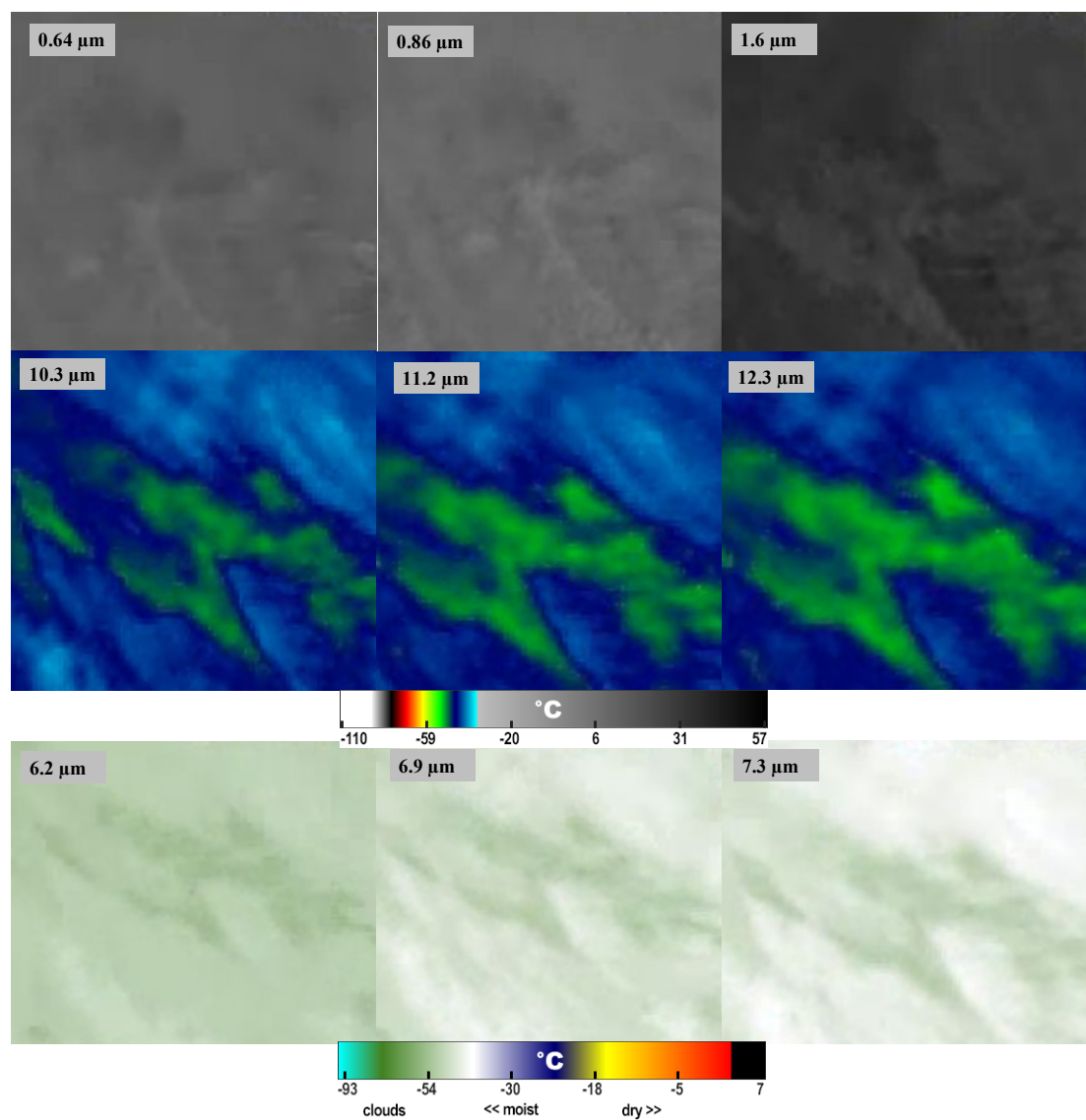


Figure A3.7. Same as Figure A3.1 but for January 13, 2024, at 17:11 UTC, over the Ruby Mountain.

## Ruby Seeding on 2 January 2024

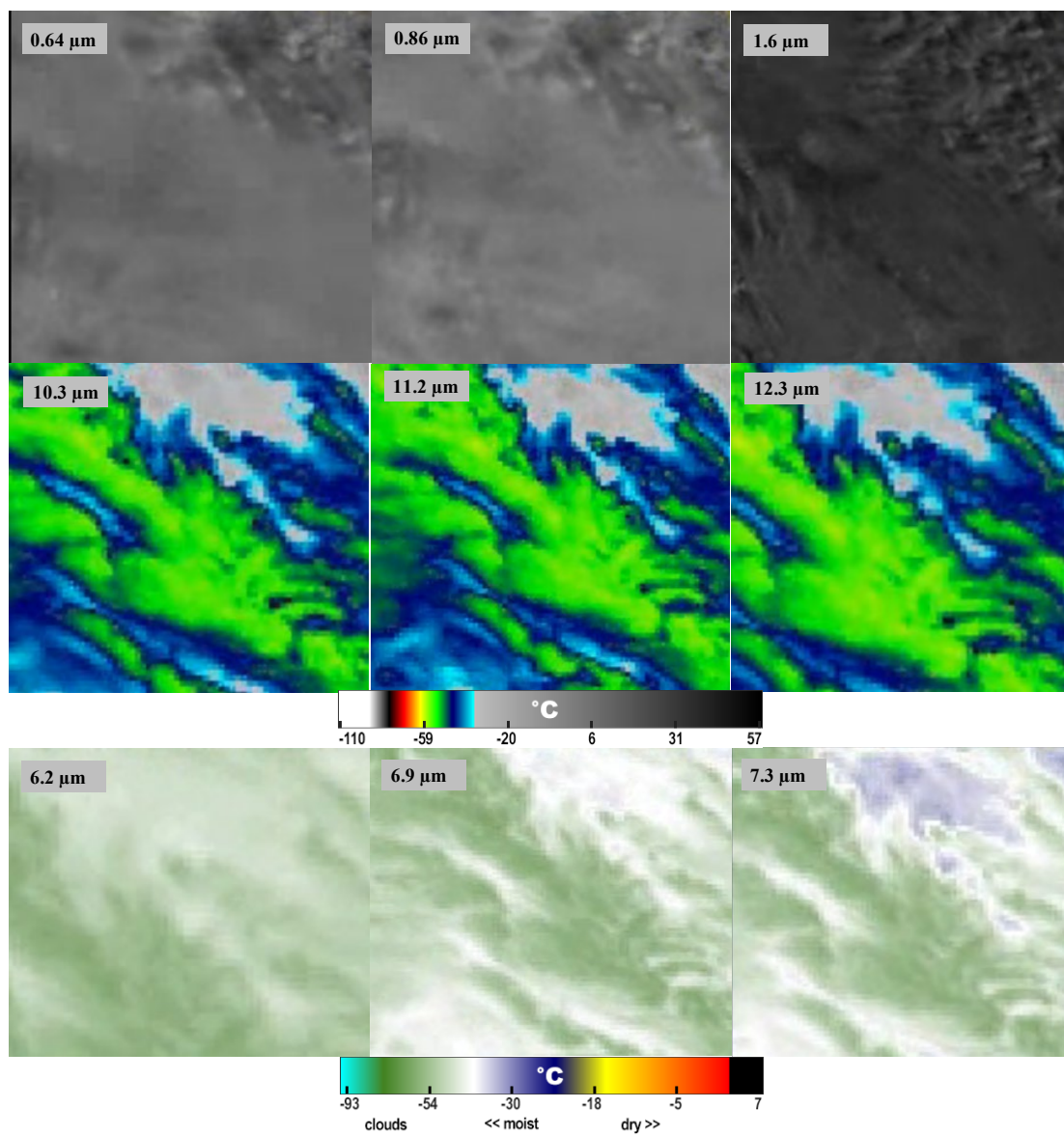


Figure A3.8. Same as Figure A3.1 but for January 2, 2024, at 14:31 UTC, over the Ruby Mountain.

## Ruby area on 3 January 2024

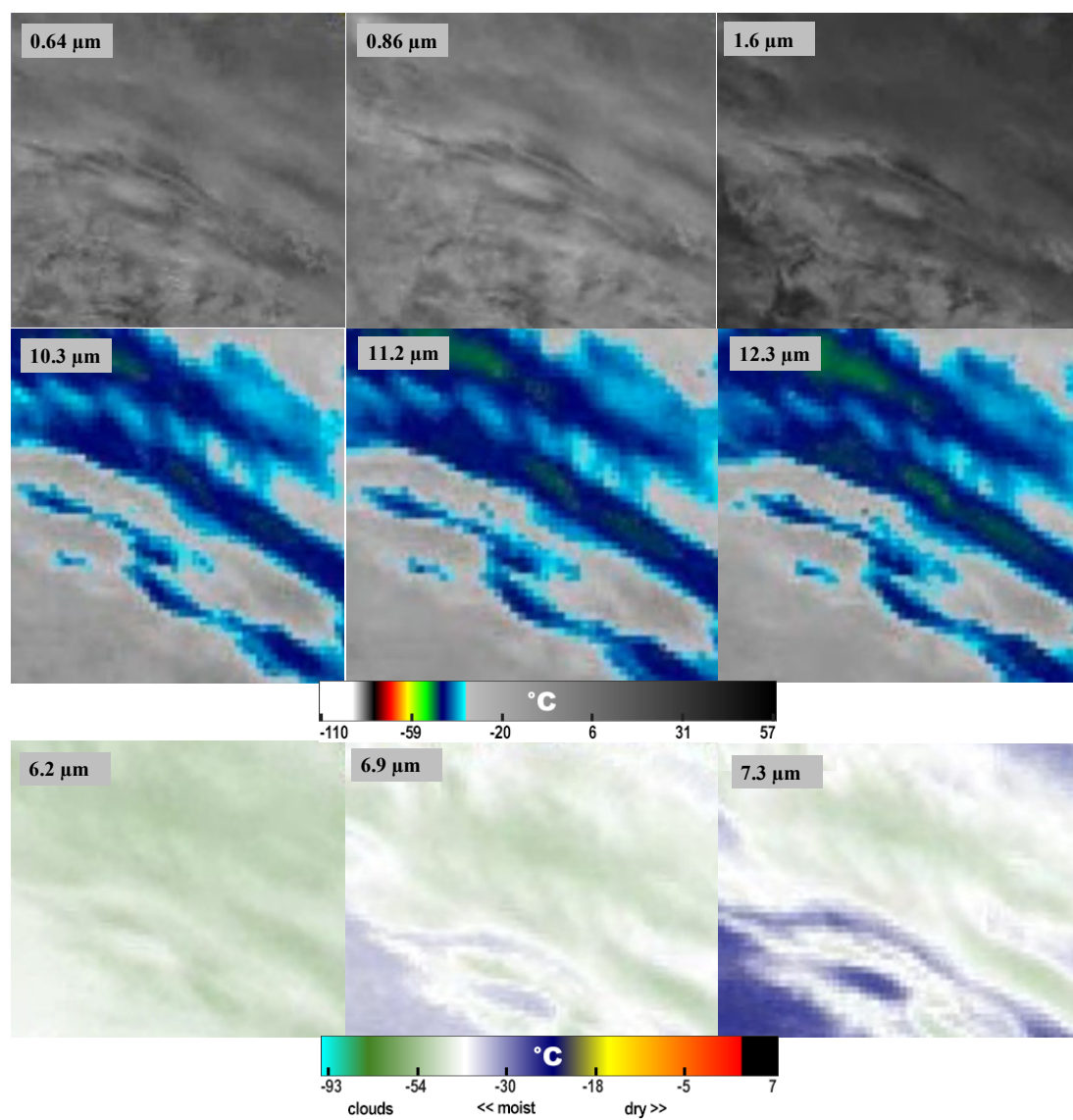


Figure A3.9. Same as Figure A3.1 but for January 3, 2024, at 20:36 UTC, over the Ruby Mountain.

## Chapter 4

### Summary and conclusions

This dissertation contributes significant advancements to the understanding and modeling of cloud seeding which is the most common weather modification technique aimed at enhancing precipitation, particularly in water-scarce regions. Through the development and application of the Snow Growth Model for Rimed Snowfall (SGMR), this research provided deeper insights into the microphysical processes involved in seeded cloud systems. By incorporating key processes such as riming and heterogeneous ice nucleation, the SGMR enabled more realistic simulations of snowfall evolution, capturing the behaviors of seeded clouds in the Tahoe region. Compared to earlier studies, which often lacked the integration of these processes, the present work offered a more comprehensive representation of cloud microphysics, yielding more accurate estimates of snowfall rate, ice particle number concentration, and ice water content.

The analysis of five cloud seeding events in the Tahoe area revealed that seeding increased snowfall rates by an average of 24%, with some cases showing enhancements of up to 37%. These increases were most prominent in colder, deeper clouds with abundant supercooled liquid water. Riming contributed significantly to enhanced ice mass, while nucleation primarily affected particle concentration. Fall speeds of snow particles were marginally affected due to the small size of nucleated crystals. The results confirm that cloud seeding

outcomes are highly sensitive to initial atmospheric conditions, including moisture availability and temperature structure.

To extend the applicability of the findings, the study also analyzed 13 cloud seeding events across three regions—Lake Tahoe, Santa Rosa Range, and Ruby Mountains—using satellite remote sensing data. This comparative analysis revealed clear spatial variability in cloud seeding effectiveness, underscoring the role of local meteorological conditions. The Tahoe region displayed the most consistent and favorable seeding responses, with satellite observations confirming enhanced cloud glaciation, increased optical thickness, and enhanced precipitation potential. These effects were linked to high mid- and upper-tropospheric moisture, substantial optical thickness, and cold cloud-top temperatures. In contrast, the Santa Rosa cases exhibited limited response, likely due to insufficient moisture and warmer, thinner clouds. The Ruby Mountains presented mixed outcomes, with some cases reflecting favorable seeding indicators and others showing minimal changes.

Satellite-derived spectral metrics, such as reflectance and absorption in shortwave bands, brightness temperature differences in thermal infrared channels, and cloud optical depth, proved to be effective tools for assessing cloud phase transition, depth, and glaciation. These metrics confirmed that seeding is most effective in clouds that are optically thick, moisture-rich, and cold, particularly those exhibiting substantial supercooled liquid water content. The study also found that the presence of mixed-phase cloud layers served as a strong predictor of successful seeding outcomes.

Together, these two investigations form a cohesive framework for understanding and improving cloud seeding operations. The SGMR model provided a computationally efficient and physically grounded tool for simulating the microphysical response of clouds to seeding, while the satellite-based analysis offered region-specific insights into the environmental conditions helping to effective seeding. This dual approach enabled a rigorous assessment of seeding impacts and identified key atmospheric indicators for targeting seeding operations.

Significantly, the four objectives outlined at the beginning of this dissertation have now been directly addressed through the research presented. The study successfully incorporated satellite remote sensing perspectives to enhance both model validation and the interpretation of seeding responses. The SGMR was applied and improved to simulate seeded snowfall with greater accuracy by incorporating essential microphysical processes. Controlled model experiments were conducted under diverse atmospheric conditions to quantify the impact of seeding on snowfall, and regional satellite-based analyses offered robust criteria for evaluating seeding potential. Each objective has contributed to a more comprehensive and operationally useful understanding of cloud seeding. As climate change intensifies drought risks and disrupts regional hydrological cycles, especially in the western United States, cloud seeding has emerged as a potential tool for water resource management. However, its success depends on more than just the application of seeding agents, it requires precise targeting, informed by a scientific understanding of cloud physics and environmental variability. This dissertation contributes to that understanding by integrating advanced microphysical modeling with remote sensing tools, thus enhancing both predictive capability and operational effectiveness.

In conclusion, this work provides both a theoretical and applied foundation for the continued development of cloud seeding as a viable weather modification strategy. It highlights the need for:

- High-resolution modeling tools that reflect real atmospheric processes,
- Satellite-based diagnostics to identify seedable conditions,
- And a regionally tailored approach to account for atmospheric variability.

By bridging these elements, this dissertation not only advances cloud microphysics research but also supports more effective, evidence-based weather modification practices in an era of increasing water scarcity.

#### 4.1. Recommendation for future work

While this dissertation advances the knowledge of cloud seeding mechanisms through enhanced microphysical modeling and satellite-based observational analysis, several key opportunities remain to refine and expand upon these findings.

First, future research can move beyond one-dimensional modeling tools like SGMR to more advanced three-dimensional mesoscale models capable of capturing dynamic interactions between cloud microphysics, topography, and atmospheric circulation. Combining sophisticated aerosol schemes into these models would improve the simulation of aerosol-cloud interactions, including the dispersion, activation, and transformation of seeding agents such as silver iodide.

Second, the analysis would benefit from additional in situ observational data, such as aircraft-based cloud microphysics measurements, to validate both modeled and satellite-derived outputs.

Third, while this study focused on orographic clouds, applying its approaches to other cloud types such as convective or maritime stratocumulus, would broaden its applicability and inform seeding strategies across diverse meteorological regimes. Examining interannual and long-term variability in seeding responses could also shed light on how cloud seeding effectiveness may shift under changing climate conditions.

From an observational perspective, integrating machine learning and data assimilation techniques with satellite observations is promising for automating the identification of seedable cloud conditions and quantifying seeding impacts. These tools could enhance operational decision-making and support more adaptive, responsive cloud seeding programs.

In summary, future work should focus on expanding modeling capabilities, strengthening observational validation, exploring a wider range of cloud environments, and leveraging emerging technologies for real-time analysis. These efforts are helpful in making cloud seeding a more reliable and practical tool for managing water resources, especially as we face increasing climate and water-related challenges.